Titre: Title:	Electrodeposition of PEDOT on Linear and Curved Intracerebral Probes for Improved Neural Recording and Stimulation
Auteur: Author:	Jo'Elen Hagler
Date:	2025
Type:	Mémoire ou thèse / Dissertation or Thesis
Référence: Citation:	Hagler, J. (2025). Electrodeposition of PEDOT on Linear and Curved Intracerebral Probes for Improved Neural Recording and Stimulation [Thèse de doctorat, Polytechnique Montréal]. PolyPublie. https://publications.polymtl.ca/66228/

URL de PolyPublie: PolyPublie URL:	https://publications.polymtl.ca/66228/
Directeurs de recherche: Advisors:	Fabio Cicoira, & Bénédicte Amilhon
Programme: Program:	Génie chimique

POLYTECHNIQUE MONTRÉAL

affiliée à l'Université de Montréal

Electrodeposition of PEDOT on linear and curved intracerebral probes for improved neural recording and stimulation

JO'ELEN HAGLER

Département de génie chimique

Thèse présentée en vue de l'obtention du diplôme de *Philosophiæ Doctor*

Génie chimique

Juin 2025

POLYTECHNIQUE MONTRÉAL

affiliée à l'Université de Montréal

Cette thèse intitulée :

Electrodeposition of PEDOT on linear and curved intracerebral probes for improved neural recording and stimulation

présentée par **Jo'Elen HAGLER**

en vue de l'obtention du diplôme de *Philosophiæ Doctor*

a été dûment acceptée par le jury d'examen constitué de:

Gregory DE CRESCENZO, président
Fabio CICOIRA, membre et directeur de recherche
Bénédicte AMILHON, membre et codirectrice de recherche
Raphaël TROUILLON, membre
George Gregory MALLIARAS, membre externe

DEDICATION

To my loving father, mother, and partner.

ACKNOWLEDGEMENTS

First, I would like to thank my dad, mom, and my partner, Yasser. I would not have achieved this without them. Their guidance, unwavering support, and belief in my abilities provided me with the confidence and resilience to grow personally and reach the goals I set out to accomplish.

I want to extend my heartfelt thanks to my supervisor, Fabio Cicoira, for welcoming me into your research group and guiding me in the field of conducting polymers. Your unwavering support over the years, as well as your faith in my research capabilities, has granted me the freedom to accomplish this challenging project. Thank you for placing your confidence in me. Special thanks to my cosupervisor, Bénédicte Amilhon, for your encouragement, which has provided me with tremendous confidence, for answering all my neuroscience questions, and for your invaluable insights that inspired the development of the curved neural device.

I want to express my gratitude to Guillaume Ducharme for conducting numerous surgeries, offering practical guidance for the in vivo experiments, and sharing your expertise in neural device electronics with me. Your passion for neuroscience and consistent support have profoundly influenced my personal and professional growth. Your enthusiasm for my project, especially during the initial implantation of the curved neural device, has greatly motivated me and strengthened my dedication to the success of our work.

Fabio, Bénédicte, and Guillaume, it has been a pleasure working with you. I am very grateful for the opportunities you provided me. Thank you for allowing me to be part of your creativity and scientific endeavours. I hope to have the good fortune to continue doing so in the future!

I would like to thank my colleagues in Fabio Cicoira's group who guided me as a new PhD student, in particular, Côme Bodart for his excellent thesis that introduced me to this field, Nicolò Rossetti, who trained and guided me, and Arun Subramanian, who made me feel especially welcome and always made me laugh. Thank you to all the students in this group who assisted and collaborated with me throughout the years. Thank you to Meijing Wang for being a wonderful friend and colleague and for helping me with microfabrication. Thank you to Xin Zhou for always being available to discuss research together – we had many laughs and interesting conversations over the years. Thank you to Jeeyeon Yeu for your friendship and collaboration during the most challenging stages of this project. Thank you to Chi-Hyeong Kim and Pierre Kateb; I enjoyed learning from you and collaborating with you to create flexible epidermal devices.

I am deeply grateful to Yasser Matos-Peralta for generously sharing his expertise in chemistry. His guidance has significantly refined my skills, enhanced my understanding of electrochemistry, and allowed me to overcome numerous challenges.

Thank you to all my colleagues in Bénédicte Amilhon's group, especially Justine Fortine-Houde, for training me in immunohistochemical analysis, and Lucia Pizzoccaro for performing the tissue preparation and analysis. I am grateful to have had the opportunity to learn so much from your expertise in neuroscience.

Many thanks to the technicians of the GCM laboratory, especially Christophe Clément, who provided expert training and guidance in microfabrication techniques and assisted me in developing and refining the fabrication protocols. Your technical expertise was invaluable in helping me build these devices. Your happiness and energy made the clean room a bright place to work and sparked a new passion for building microelectronics within me. I also want to thank André Hoang Gaona for being so kind, for always being available to help me troubleshoot, and for assisting me in improving the quality of my devices.

A special thank you to Alexandre Bréard in the Chemical Engineering department for being kind and helpful throughout my PhD, especially in seeing me through to the end. I am truly grateful for all the professors, researchers, technicians, and administration that are passionate about helping students succeed and achieve their goals.

RÉSUMÉ

Les réseaux de microélectrodes sont des outils standards pour la réalisation d'expériences électrophysiologiques chroniques, permettant aux chercheurs d'enregistrer simultanément l'activité d'un grand nombre de neurones. Dans le domaine des neuroprothèses, les microélectrodes ciblant les structures cérébrales profondes sont couramment utilisées pour identifier les zones épileptogènes ou traiter la maladie de Parkinson. L'adoption clinique des réseaux de microélectrodes a cependant été entravée par des déficits dans leur fiabilité à long terme. La performance et la longévité du dispositif sont associées à l'impédance électrique des microélectrodes, ce qui limite la capacité de stimulation de l'électrode ou la qualité de l'enregistrement du signal neuronal. Les approches d'ingénierie des matériaux et des dispositifs visant à atténuer les causes de défaillance des dispositifs et à améliorer les enregistrements ou la stimulation neuronale sont conçues pour améliorer simultanément la performance des électrodes et minimiser la réponse neuro-inflammatoire.

Une méthode bien établie pour améliorer la performance des électrodes consiste à modifier la surface des microélectrodes métalliques plates avec des polymères conducteurs, en particulier le poly(3,4-éthylènedioxythiophène) (PEDOT). Le PEDOT offre un avantage unique pour améliorer la performance des microélectrodes en raison de ses diverses voies de dépôt, de sa capacité à établir des microstructures et de ses excellentes propriétés de conduction mixte. Le revêtement des surfaces des microélectrodes avec du PEDOT augmente considérablement la surface électroactive de l'interface électrode/tissu et réduit l'impédance, ce qui se traduit par un rapport signal/bruit (RSB) amélioré et une capacité de stimulation accrue.

Un avantage fréquemment cité du PEDOT est sa stabilité supérieure par rapport aux autres polymères conducteurs. Pour étudier cette stabilité, une série de tests simulant un environnement biologique ont été effectués in vivo en utilisant des microfils de PtIr revêtus de PEDOT:BF_4 électrodéposé. Les résultats ont indiqué que l'électroactivité du PEDOT restait constamment stable au fil du temps. Cela a été confirmé par des tests de vieillissement accéléré dans une solution saline tamponnée au phosphate, qui simulaient une année à la température corporelle. De plus, la biocompatibilité du PEDOT:BF_4 a été évaluée en comparant la réponse inflammatoire après implantation dans le cortex de rongeur à des microfils de PtIr non revêtus. Ces tests ont révélé des niveaux similaires d'inflammation modérée pour les deux électrodes.

L'incompatibilité mécanique entre le cerveau et le matériau de la sonde est reconnue comme une cause principale de la formation de cicatrices. En remplaçant les sondes rigides en silicium ou en métal par des polymères plus souples, nous pouvons réduire la disparité des propriétés mécaniques entre le tissu et la sonde, aidant ainsi à atténuer la réaction neuro-inflammatoire.

Cette thèse détaille la conception et les techniques de fabrication d'une sonde neuronale flexible présentant une forme non conventionnelle. Lors de la conception d'un réseau de microélectrodes, il est essentiel d'évaluer l'accessibilité de la région cérébrale ciblée et des types de cellules neuronales spécifiques. Une nouvelle approche a été développée pour créer une configuration de réseau d'électrodes courbe visant à l'enregistrement intracérébral dans la région CA1 de l'hippocampe ventral. Ce réseau à base de parylene présente un substrat de 4 μm d'épaisseur avec 16 microélectrodes en or uniformément espacées disposées le long d'un rayon de 7 mm, permettant de cibler des régions cérébrales profondes anatomiquement complexes. Chaque électrode est revêtue du polymère conducteur PEDOT:BF_4 pour améliorer le transfert de charge. Un support de soie avec une courbure identique fournit la résistance mécanique nécessaire pour implanter la sonde courbe flexible. La sonde courbe assemblée a été testée dans l'hippocampe dorsal de rongeur, enregistrant avec succès des potentiels de champ locaux et des potentiels d'action extracellulaires.

Le nettoyage électrochimique des microélectrodes en or, l'optimisation des revêtements de PEDOT et l'amélioration de l'assemblage des dispositifs ont été identifiés comme des étapes essentielles pour améliorer l'utilité de ces dispositifs. Dans l'ensemble, cette étude démontre comment le PEDOT peut améliorer considérablement les interfaces neuronales sous divers aspects. De plus, nos résultats montrent que le support de soie a fourni la rigidité nécessaire pour pénétrer le cerveau selon une trajectoire circulaire. Des études in vivo prolongées seront nécessaires pour évaluer la longévité de la sonde. À l'avenir, nous prévoyons d'implanter la sonde courbée dans une région de l'hippocampe ventral très difficile à atteindre avec les sondes neuronales traditionnelles. Cette conception de sonde neuronale innovante peut être adaptée pour recueillir des données neuronales provenant de régions cérébrales auparavant inaccessibles, offrant des informations cruciales pour la recherche en neurosciences.

ABSTRACT

Microelectrode arrays are standard tools for conducting chronic electrophysiological experiments, allowing researchers to record simultaneously from large numbers of neurons. Within the field of Neuroprosthetics, microelectrodes targeting deep brain structures are routinely used to identify epileptogenic zones or treat Parkinson's disease. The suboptimal long-term reliability has hindered the clinical adoption of microelectrode arrays. The device's performance and longevity are associated with the electrical impedance of the microelectrodes, which limits the electrode's capacity to stimulate or the quality of the neural signal recording. Materials and device engineering approaches for alleviating the causes of device failure and improving neural recordings or stimulation are designed to simultaneously enhance electrode performance and minimize the neuroinflammatory response.

A well-established method to enhance electrode performance involves modifying the surface of flat metallic microelectrodes with conducting polymers, especially poly(3,4-ethylenedioxythiophene) (PEDOT). PEDOT provides a unique advantage for improving microelectrode performance due to its various deposition routes, capability to pattern microstructures, and excellent mixed conduction properties. Coating the surfaces of microelectrodes with PEDOT significantly increases the electroactive surface area of the electrode/tissue interface and reduces impedance, resulting in improved signal-to-noise ratio (SNR) and stimulation capacity.

A frequently cited benefit of PEDOT is its superior stability compared to other conducting polymers. To investigate this stability, a series of tests simulating a biological environment were performed in vivo using electrodeposited PEDOT:BF_4 coated PtIr microwires. The results indicated that the electroactivity of PEDOT remained consistently stable over time. This was further confirmed through accelerated aging tests in phosphate-buffered saline, which simulated one year at body temperature. Additionally, the biocompatibility of PEDOT:BF_4 was evaluated by comparing the inflammatory response after implantation in the rodent cortex to uncoated PtIr microwires. These tests revealed similar levels of moderate inflammation for both electrodes.

The mechanical incompatibility between the brain and the probe's material is recognized as a primary cause of scar formation. By replacing rigid probes made of silicon or metal with softer

polymers, we can reduce the disparity in mechanical properties between the tissue and the probe, helping to alleviate the neuroinflammatory reaction.

This thesis details the design and fabrication techniques for a flexible neural probe featuring an unconventional, non-orthogonal shape. When designing a microelectrode array, it is vital to assess the accessibility of the target brain region and the specific neuron cell types. A novel approach has been developed to create a curved electrode array configuration aimed at intracerebral recording within the CA1 region of the ventral hippocampus. This parylene-based array features a 4 μm thick substrate with 16 evenly spaced gold microelectrodes arranged along a circular path with a 7 mm radius, enabling the targeting of anatomically complex deep brain regions. Each electrode is coated with the conductive polymer PEDOT:BF_4 to enhance charge transfer. A silk shuttle with identical curvature provides the necessary mechanical strength to implant the flexible curved probe. The assembled curved probe was tested acutely in the rodent cortex, successfully recording distinguishable local field potentials and extracellular action potentials.

The electrochemical cleaning of gold microelectrodes, optimization of PEDOT coatings, and improvement of device assembly have been identified as essential steps to enhance the utility of these devices. Overall, this study demonstrates how PEDOT can significantly enhance neural interfaces in various aspects. Moreover, our findings show that the silk shuttle provided the necessary stiffness to penetrate the brain in a circular trajectory. Extended in vivo studies will be needed to assess the probe's longevity. Moving forward, we plan to implant the curved probe in a region of the ventral hippocampus that is very challenging to reach with traditional neural probes. This innovative neural probe design can be tailored to collect neural data from previously inaccessible brain regions, offering critical insights for neuroscience research.

TABLE OF CONTENTS

LIST OF TABLES

LIST OF FIGURES

LIST OF SYMBOLS AND ABBREVIATIONS

ADC	Analog-to-digital converter
BBB	Blood-brain barrier
CA1	Cornu Ammonis field 1
CSD	Current source density
CSC	Charge storage capacity
CT	Computed tomography
CV	Cyclic voltammetry
CVD	Chemical vapor deposition
DAPI	4',6-diamidino-2-phenylindole
Dex	Dexamethasone
DIW	Deionized water
dHP	Dorsal hippocampus
DNA	Deoxyribonucleic acid
DRIE	Deep reactive ion etching
ECoG	Electrocorticography
EDA	Electrodermal activity
EEG	Electroencephalography
EIS	Electrochemical impedance spectroscopy
FBR	Foreign body response

FPC	Flexible printed circuit
GFAP	Glial fibrillary acid protein
HOMO	Highest occupied molecular orbital
IPA	Isopropyl alcohol
LUMO	Lowest unoccupied molecular orbital
LFP	Local field potential
MRI	Magnetic resonance imaging
OECT	Organic electrochemical transistor
PaC	Parylene-C
PBS	Phosphate-buffered saline
PCB	Printed circuit board
PDMS	Polydimethylsiloxane
PEDOT	Poly(3,4-ethylenedioxythiophene)
PET	Polyethylene terephthalate
PFA	Paraformaldehyde
PSS	Poly(styrene sulfonate)
PtIr	Platinum iridium
RIE	Reactive ion etching
sEEG	Stereotactic EEG

SEM	Scanning electron microscope
SNR	Signal-to-noise ratio
SOI	Silicon-on-insulator
SU-8	Epoxy-based negative photoresist
$TEABF_4$	Tetraethylammonium tetrafluoroborate
TPU	Thermoplastic polyurethane
UEA	Utah electrode array
vHP	Ventral hippocampus

LIST OF APPENDICES

CHAPTER 1 INTRODUCTION

Neurophysiology and neuroprosthetics are invaluable tools for monitoring, diagnosing, and treating human neurological diseases. Technological advancements in microelectronics have led to the development of highly reliable and safe penetrating microelectrode arrays capable of interfacing directly with neural tissue [2]. Human brain intracerebral electrophysiology is most often applied for the surgical treatment of epilepsy [3, 4], movement disorders [5, 6], and brain tumors [7, 8]. Neurophysiological mapping in epilepsy has arguably the most significant potential for advancing human-based neuroscience to understand specific mechanistic functions of local neural circuits or whole brain areas [9].

Epilepsy surgery is a treatment option for patients who experience seizures that cannot be controlled with medication. Identifying and surgically removing, or resecting, the source of the seizures in the brain can completely suppress them. Multiple penetrating depth electrodes, implanted along oblique trajectories, map the potential source of seizures in deep brain structures such as the hippocampus. However, innovative neural interfaces and trajectories could reduce the number of electrodes required in surgical interventions and record from regions that are currently inaccessible due to the complex structure of the human brain.

Advances in human neuroscience and understanding how neurological disorders are expressed in the brain require new high-density microelectrode array technologies appropriate for human use. Additional design parameters—e.g., optimized electrode coatings to improve signal quality, conformal and unique form-factor probes to mediate the foreign body response, and unconventional electrode and probe architectures able to target curved and deep brain structures—need to be included for practical recording and stimulation studies and long-term clinical translation of neural interfaces.

1.1 Neurons

The brain and spinal cord compose the central nervous system, which relies on nerve cells, or neurons, as its fundamental building blocks. Neurons across brain regions work together to form neural networks responsible for encoding, processing, and transmitting information that initiates behavioral responses. Neurons transmit information by generating electrical signals, a process driven by the movement of ions across their plasma membranes. A neuron consists of a cell body,

essential for the neuron's signaling capabilities; dendrites, which primarily receive inputs from neighboring or distant neurons; and the axon, mainly responsible for transmitting signals to other cells through a structure called the synapse. When incoming signals elevate the neuron's membrane potential beyond a specific threshold, the neuron becomes activated and generates an electrical impulse termed an action potential. This impulse is then chemically transmitted at the axon terminal to the target tissue.

1.2 Mechanism of neural network communication

The intracellular environment of a neuronal cell contains high concentrations of potassium (K^+). Conversely, the extracellular medium contains primarily sodium (Na^+), chloride (Cl^-) and calcium (Ca^+) ions. The neuronal cell membrane separates the two spaces, maintaining a potential difference of approximately −60 mV inside the cell relative to the outside environment. Ions can move in and out of the cell through small openings called ion channels, which rapidly open or close depending on the membrane potential. When the channels are open, ions flow passively depending on the ion's intra- or extracellular concentration gradient. Ion pumps actively transport ions against their concentration gradient to restore and maintain the neuron's resting potential. For example, the fast (Na^+) action potential is the largest amplitude intracellular event. The action potential is initiated by the binding of chemicals known as neurotransmitters to receptors embedded in the synapse of a neuron—the thin gap between the axon terminal and the membrane of the sensing neuron. The activation of the receptors changes the conformation of the channels, allowing Na^+ to enter the cell. At a critical threshold of Na^+ influx, additional channels open, and a rapid influx of Na+ occurs, depolarizing the membrane to a peak potential of approximately +20 mV inside the cell. This event is shown by the rising phase of the action potential (Figure 1.1). At the peak potential, the voltage-dependent inactivation of Na^+ channels halts the influx of Na^+, while activation of K^+ channels quickly compensates for the Na^+ influx by the efflux of K^+. The repolarization of the cell to the resting voltage is portrayed as the falling phase of the action potential. The action potential then propagates from the axon to the neuron's dendrites, influencing the activity at the synapses of neighboring neurons.

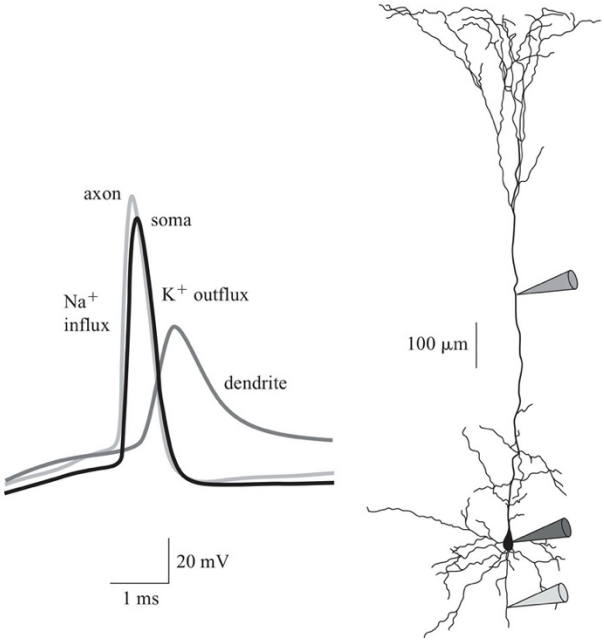

Figure 1.1 Action potential propagation forward to the axon terminal and backward to the dendrites. Action potential waveform (left) recorded from the axon, soma, and dendrite in a pyramidal neuron (right). Reproduced with permission from [12].

1.3 Extracellular currents : Recording and analysis

1.3.1 Action potentials

The action potential refers to the largest amplitude potential event intracellularly, while it is referred to as unit activity or spikes extracellularly. The recorded signal of the intracellular action potential and extracellular unit activity reliably correlate, although the amplitude, duration, and shape differ [13]. These output signals of the neuron can be measured extracellularly as a voltage difference with a recording electrode. The amplitude of the recorded spike attenuates as the distance between the recording site and the neuron cell body increases [14]. Therefore, recording a significant amplitude signal with a biphasic waveform typical of a spike indicates that the electrode is close to the cell body of a neuron [15].

1.3.2 Local field potentials

Neurons are surrounded by a conductive matrix composed of the extracellular medium. The current flowing across the neuronal membrane causes potential differences to propagate through the

extracellular space. At any given point outside the neuron, the recorded potential represents the linear summation of numerous overlapping potential fields generated by a population of neighboring neurons, referred to as the local field potential (LFP) [16].

There is a negligible contribution of unit activity to the local field because of the low-pass filtering properties of the extracellular space. The higher frequency unit activity (100 Hz to 10 kHz) attenuates more with distance than the relatively slow field potential activity (0.1 to 100 Hz). Slower changing voltages, such as the effects of postsynaptic potentials, can propagate much farther in the extracellular medium, allowing for the temporal summation of current from synchronously activated neurons [17]. Consequently, the local field potentials are an excellent tool for assessing the spatiotemporal cooperativity of neurons in a structure.

The number of neurons contributing to the measured signal varies substantially depending on the size and placement of the recording electrode. Suppose the electrode is small enough and placed near the cell bodies of a small number of neurons. In that case, there can be a statistical relationship between the local field potentials (cooperating inputs into the cell population) and the spike outputs [18].

1.3.3 CSD analysis

Recording electrodes must be small and positioned close to the neuron's cell body to determine the source of local activity. By using several equidistant microelectrodes to simultaneously record from the same neuron, the current source density (CSD) of local currents can be calculated and analysed to identify the generation site of activity. Current source density analysis is employed to calculate profiles of current sources (positive charges flowing from the intracellular space of a neuron to the extracellular medium) and sinks (positive charges flowing into the cell) based on extracellular potential recordings.

CSD is a scalar quantity that measures the current entering a volume of extracellular space per unit volume. The one-dimensional CSD (e.g. along the axodendritic axis of a neuron) can be estimated by the second spatial derivative of the recorded potential as a function of depth according to

$$\sigma_z \frac{\partial^2 \phi}{\partial z^2} = -I_m \qquad 1.1$$

where z is the direction perpendicular to the neural layer structures or laminae, σ is the conductivity tensor of the extracellular medium, ϕ is the field potential, and I_m is the CSD [19, 20]. The voltage gradient, i.e., the rate at which the potential field attenuates with distance from the source, can be determined by the difference in voltage recorded at adjacent electrodes.

If electrodes are placed far from the source, the voltage gradient will be the same at each electrode (the voltage attenuates at the same rate). Thus, the difference between the voltage gradients (the second derivative of the potential) will be zero, indicating the measured field wasn't generated locally. Conversely, if the electrodes were placed near the source of local activity, the difference between voltage gradients of the adjacent electrodes would be significant. By placing many

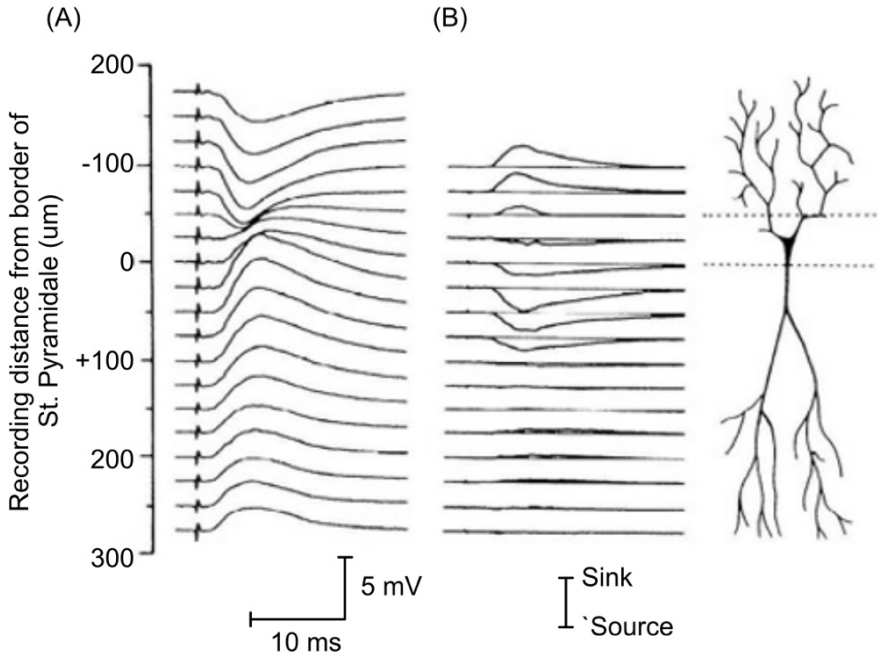

Figure 1.2 Current source density analysis. (A) Field potentials at 25 μm intervals parallel to the cell axis. (B) CSD analysis reveals a sink (positive) in the stratum oriens and a source (negative) in the cell body layer and proximal dendrites. A pyramidal cell is shown on the right, with the borders of the stratum pyramidale denoted by dotted lines. Distance along the cell axis is taken from the ventral border (0 μm). Sink or source current is taken relative to the polarity of the CSD. Reproduced with permission from [21].

microelectrodes close together, the precise location of maximum current density can be determined, indicating the exact location of the current origin [12, 16]. An example of CSD analysis in the stratum oriens is shown in Figure 1.2 [21]. Figure 1.2A shows the field potential recorded at

different locations along the cell. The CSD analysis (Figure 1.2B) computed from the field potential displays the development of a current sink in the region of the dendrites, indicating current flowing from the extracellular space into the cell, and a current source at the cell body.

The one-dimensional CSD is only valid if the potential remains constant in the lateral direction (within the same layer of laminated structures) [19]. This condition does not apply to curved layers, as seen in the hippocampus. In these cases, a single linear microelectrode array cannot effectively capture signals perpendicular to the neural layers. Therefore, recording from curved layers necessitates using a 2D or 3D microelectrode array, which consists of multiple shanks of linear electrode arrays, with recording sites arranged laterally along each shank and throughout their length. By analyzing LFPs obtained from various positions in both directions orthogonal to the neural layer, one can derive the two-dimensional CSD [22].

1.4 Electrochemistry of recording and stimulating extracellular signals

A microelectrode used to record from or stimulate a neural cell is always paired with a second grounded electrode, such as a metal screw in contact with the brain. This electrode setup can be compared to microelectrodes immersed in a saline solution of an electrochemical cell. The microelectrode acts as the working electrode, while the ground is the combined reference/counter electrode. The recording electrode of a neural interface senses voltage fluctuations generated from nearby neurons, generating a current that flows to ground through the head-stage amplifier. The amplifier detects these fluctuations in input voltage (V_{in}) and outputs an amplified voltage (V_{rec}). This output is further amplified, filtered, and processed before being displayed. Any noise at the electrode or within the system is also amplified and displayed as background noise in the recorded signal [23]. Stimulation electrodes, on the other hand, inject current to trigger a response in a small population of neurons. Current is driven from the microelectrode to a distant ground. The amount of charge must be sufficiently high to depolarize the membranes of target neurons and initiate action potentials. An electrode should possess a high charge injection capacity to ensure safe and efficient stimulation [24].

Understanding the electrochemical mechanisms at the interface between the electrode and tissue is crucial for establishing electrical communication with tissue. The capacity of a stimulation or recording electrode to convert electronic current at the electrode into ionic current is measured by its charge transduction properties. The primary mechanisms of charge transduction at the electrode

interface are Faradaic, capacitive, and pseudocapacitive. In Faradaic reactions, electrons transfer across the interface, causing oxidation or reduction of surface-confined species or species in solution. In capacitive charge injection, charges are transferred without physically crossing the interface itself through the charging and discharging of the electrical double layer, which is formed from the electrostatic separation of ions and electrons, as well as the electrolyte dipole orientation. When Faradaic reactions are confined to a surface monolayer, these reactions are described as pseudocapacitive and involve double-layer charging, as well as charge transfer across the interface. The electrode surface's material and microstructure, and the interface's potential, determine the extent to which each of these mechanisms occurs.

To detect potential signals or inject charge into neural tissue, charge carriers must cross the charge injection barrier between the tissue's liquid phase and the electrode's solid phase. The complete neural interface includes biotic (nervous tissue) and abiotic (electrodes, interconnects, amplifiers) components, meaning the overall recording or stimulation performance does not directly reflect the electrode. To reduce variability from biological factors, electrodes are often characterized in environments that simulate the brain, such as phosphate-buffered saline (PBS). The chemical composition of PBS closely resembles the brain's extracellular fluid in terms of key species like Na^+, Cl^-, H^+, and K^+ [25]. While other biological species present in vivo can affect the electrode surface, the fundamental electrode properties affecting the electrochemical performance are expected to remain consistent between the two environments [26]. Therefore, PBS is a suitable environment for short-term in vitro electrode characterization. Evaluation of the long-term performance of electrodes should also consider the changes in the electrochemical environment initiated by the neuroinflammatory response, such as local changes in pH, reactive ion species, and protein adsorption on electrode surfaces [27].

1.4.1 Neural interface impedance

The properties of the microelectrode can be decoupled from other components influencing the neural interface performance of the system by characterizing the electrode using electrochemical impedance spectroscopy (EIS). Electrochemical impedance measures the resistance of charge transduction between the electrode and the ionic medium. A stimulation electrode with low impedance requires a lower supplied voltage to inject a given amount of charge, enabling a higher

charge injection limit and safer stimulation. A recording electrode with low impedance will acquire a signal with reduced noise and greater signal amplitude.

During EIS, the microelectrode is immersed in an electrolyte solution, such as PBS, alongside a platinum counter electrode and a silver/silver chloride (Ag/AgCl) reference electrode. EIS evaluates an electrode's response to a sinusoidal potential at a specific frequency *f*. The excitation potential should remain low (10–100 mV) to prevent unwanted electrochemical reactions at the electrode surface. By comparing the amplitude and phase of the input potential with the recorded output current, the electrochemical impedance (Z) of the system is calculated. Measuring Z across a range of frequencies produces a spectrum of impedances, typically represented in a Bode plot. This plot illustrates the magnitude of the impedance on a logarithmic scale and its phase shift on a linear scale, recorded at each frequency. The Bode plot outlines the 'transfer function' of the working electrode interface, demonstrating how signals of varying frequencies are transmitted.

The electrode-tissue interface, in response to the sinusoidal potential, can be modeled and optimized with an equivalent electrical circuit. This equivalent circuit can help us to understand the physical processes involved in charge transfer at the interface. In the case of an electrode in contact with neural tissue, the model treats the neural signal as a low-impedance voltage source. A resistor describes the extracellular matrix and depends on the geometry of the recording site. A resistor and a capacitor in parallel represent the Faradaic surface reactions and the electrical double-layer capacitance. Often, the electrode impedance is modeled using constant phase elements or Warburg impedances depending on the electrode coating or surface properties.

Tissue and electrode resistances attenuate the recorded signal independent of frequency. In contrast, the double-layer capacitance contributes attenuation as well as a phase shift of 90°. In the case of a metal electrode in contact with saline, the equivalent circuit describes the behaviour of a high-pass filter. At high frequencies, the impedance contribution from the double-layer capacitor is negligible, and the charge transfer is limited by the diffusion of ionic species in the electrolyte. This results in attenuation of the potential signal in proportion to the electrolyte resistance without a phase shift. In contrast, charge transfer at mid-range frequencies is controlled by faradaic surface reactions in parallel with the double-layer capacitance, resulting in significant attenuation and a 90° phase shift. At very low frequencies, the impedance of the double-layer capacitance approaches

infinity, and the solution and electrode resistance control the charge transfer, resulting in more attenuation without a phase shift.

The electrical double-layer capacitance is proportional to the contact area between the electrode and the electrolyte. For smooth electrodes, the contact area is the geometrical surface area. In contrast, for rough or porous electrode surfaces, the electrochemically active area is dramatically larger than the geometrical surface area, significantly increasing capacitive charge transfer. This increase in capacitance is critical for microelectrode performance since the electrode's geometrical size can be reduced to increase spatial selectivity while still achieving low impedance.

The impedance of neural electrodes is typically characterized at 1 kHz, as the primary information in action potentials occurs around this frequency. However, action potentials and local field potentials (LFPs) encompass a broader range of frequency components [16]. The frequency of LFPs can be as low as 1 Hz, and the impedance at low frequencies can be several orders of magnitude higher than at high frequencies. As a result, LFP recordings may be heavily influenced by frequency-dependent filtering.

To quantify the electrode performance, the cutoff frequency offers a more informative alternative to the 1 kHz impedance for identifying the signal band where frequency-dependent filtering occurs at the interface [28]. The cutoff frequency is defined as the point at which the signal magnitude is reduced by 3 dB relative to the signal transfer in passband. It can be determined by the frequency corresponding to a phase angle of –45°, marking the transition of the electrode charge transfer from primarily resistive to capacitive.

1.4.2 Cyclic voltammetry and charge storage capacity

Cyclic voltammetry (CV) offers valuable insights into the electrochemical characteristics of the electrode surface. Utilizing the same three-electrode configuration as impedance measurements, a voltage is cyclically swept at a constant rate across the working electrode while current flowing through both the working and counter electrodes is recorded. This voltage is ramped linearly with time between oxidizing and reducing potentials within the water window. During CV tests, the measured current reflects charge transfer reactions and capacitive charging at the electrode-electrolyte interface. Cyclic voltammetry can provide useful kinetic and mechanistic information about irreversible faradaic reactions, such as the electrolysis of water or diffusion-limited reactions

at the electrode surface such as the oxidation of Pt to PtO appearing as a peak at the standard electrochemical potential of Pt [29].

The electrode area, morphology, material, electrolyte, and scan rate are important factors to consider when comparing CVs from different electrodes. A quantifiable metric that can be derived from CV curves is the cathodic charge storage capacity (CSC_c), calculated as the integral of the cathodic (negative) current of the CV curve measured in charge per unit area of the electrode [30]. The CSC_c integrates all charges transferred and measures the charge the electrode can deliver for a specific voltage sweep.

1.4.3 Charge injection performance at the neural interface

Electrical stimulation of neural cells can either excite or suppress neural activity by depolarizing the membranes. This depolarization occurs through ionic current flow between an electrode positioned near the target neurons and a grounding electrode. Typically, neural stimulation is delivered as biphasic current pulses, which consist of both cathodal and anodal phases. The pulse amplitudes and durations are chosen to ensure the pulse has a net zero charge.

The parameters of the stimulation pulse consist of the charge, charge and current density – determined by the electrode's geometric surface area – and pulse frequency. These parameters are empirically determined to ensure that the delivered charge exceeds the threshold required to depolarize the cell while preventing irreversible electrochemical reactions and avoiding tissue damage. Faradaic reactions can trigger irreversible processes that damage electrodes or tissues. The most common irreversible reaction encountered with stimulation electrodes is water electrolysis, which can lead to corrosion or degradation of the electrode material, destroying its conductive properties and possibly releasing toxic by-products into the tissue [31]. Therefore, it is essential to avoid prolonged biasing of the electrode beyond the “water window,” which is defined as the range of potentials between the oxidation and reduction potentials of water. The water window varies among electrode materials but generally ranges from –0.6 to 0.8 V vs Ag/AgCl at pH 7 [32].

Targeted stimulation of neurons requires minimizing the size of the electrodes. As previously discussed, electrode impedance increases as electrode size decreases, restricting the charge injection capacity. However, by reducing the electrode dimensions below the thickness of the ion diffusion layer, the ion transport limitations on the reaction rate are lessened, resulting in significantly higher charge-injection densities [32]. Geometry also influences the effect of

stimulation. Typically, a nonuniform current distribution over the electrode surface arises, with higher charge injection reactions occurring along the perimeter or tip of an electrode [33].

The key criterion for ensuring the safety of a stimulation protocol is maintaining electrode polarization within the water window [24]. To assess the stimulation performance of an electrode in vitro, the interface polarization (E_p) of the electrode during a cathodic pulse is evaluated against the electrochemical safety threshold. Practically, a stimulator delivers a biphasic stimulus waveform while monitoring the voltage at the electrode surface. Voltage transient curves are recorded as the current amplitude is increased stepwise until E_p reaches the electrochemical limit. At this E_p, the charge injected defines the maximum charge injection capacity (CIC_{max}) that can be applied per pulse before the onset of water electrolysis [34].

1.4.4 Improving data quality in recordings of neuronal populations.

Extracellular neuronal recordings are typically performed by placing microelectrodes in a small volume of neural tissue. The recorded signal comprises the superposition of fast (100 Hz to 10,000 Hz) extracellular action potentials (spikes) and lower-frequency (<100 Hz) local field potentials. The amplitude of the extracellular spike decreases rapidly with increasing distance. Nonetheless, action potentials can be detected at several hundred microns from the soma. For instance, at distances >140 μm, a single electrode (radius = 15 μm) can detect extracellular spike activity from up to 1,000 neurons in the rat cortex [35].

Single neurons are isolated from nearby cells using multiple precisely placed recording sites and spike sorting algorithms. The specific geometric distribution of recording sites allows for the assessment of spatial relationships among individual neurons [22]. Algorithms for detecting and sorting spikes from extracellular recordings filter out low-frequency components (<100 Hz) and capture only the signal waveform that exceeds a specified amplitude threshold. Spike sorting then categorizes cell-specific waveforms based on their amplitude and shape [23, 35, 36]. The effectiveness of spike sorting techniques significantly depends on the quality of the acquisition electronics, ensuring a high signal-to-noise ratio (SNR) of the spike amplitudes compared to the background noise present in the recording.

A significant contributor to background noise is thermal noise at the recording electrode [23]. Typically, thermal noise during recordings averages around 6 μV. However, the level of thermal noise varies with the impedance at the electrode-tissue interface and the chosen recording

bandwidth [37]. Thermal noise v_n is defined as the root-mean-square voltage recorded over the bandwidth Δf. This value represents the voltage produced by thermal agitation in the resistive impedance of the electrode-tissue interface $\mathrm{Re}(Z)$ [38]. Thermal noise is estimated using the Johnson-Nyquist formula:

$$v_n = \sqrt{4k_B T \Delta f \, \mathrm{Re}(Z)} \tag{1.2}$$

where k_B is the Boltzmann constant (8.62×10^{-5} eV·K^{-1}) and T represents the absolute temperature in Kelvin. As discussed in Section 1.6, the electrode material and surface area influence the electrode impedance. When the surface area of an electrode decreases, its impedance increases, as does the thermal noise.

During intracortical microelectrode recordings, biological noise also contributes to background noise. This biological noise originates from the extracellular activity of neurons recorded at distances too far from the soma to distinguish spikes from background noise [35, 37]. The microelectrode dimensions, typically <20 μm in diameter, should be selected based on the targeted neuron type and positioned near the neurons of interest to capture large spike amplitudes while minimizing biological noise [23].

The threshold voltage for spike detection is informed by noise measured from thermal and biological sources. This threshold is chosen to optimize the detection of true events while minimizing false positives. As a result, microelectrodes that can reduce overall noise and achieve a high SNR are crucial for accurately isolating units from the recorded signal. Therefore, the design and properties of electrodes used for extracellular recordings are essential for high-quality spike sorting and the identification of individual neurons.

1.5 Recording from complex brain structures

The analysis of extracellular signals recorded with a microelectrode array requires specific spatial orientations of the recording sites to the targeted cortical layers. Many brain regions display distinct planar (laminar) layers of neural tissues organized parallel to the surface of the cortex. Linear microelectrode arrays oriented perpendicular to these layers record functionally meaningful variations in the generated potential fields (Figure 1.3). However, the potential is translationally invariant parallel to the cortical layer, and recordings from sites oriented across a single plane in the tissue would show a redundant signal [39]. To calculate the CSD from the field potential

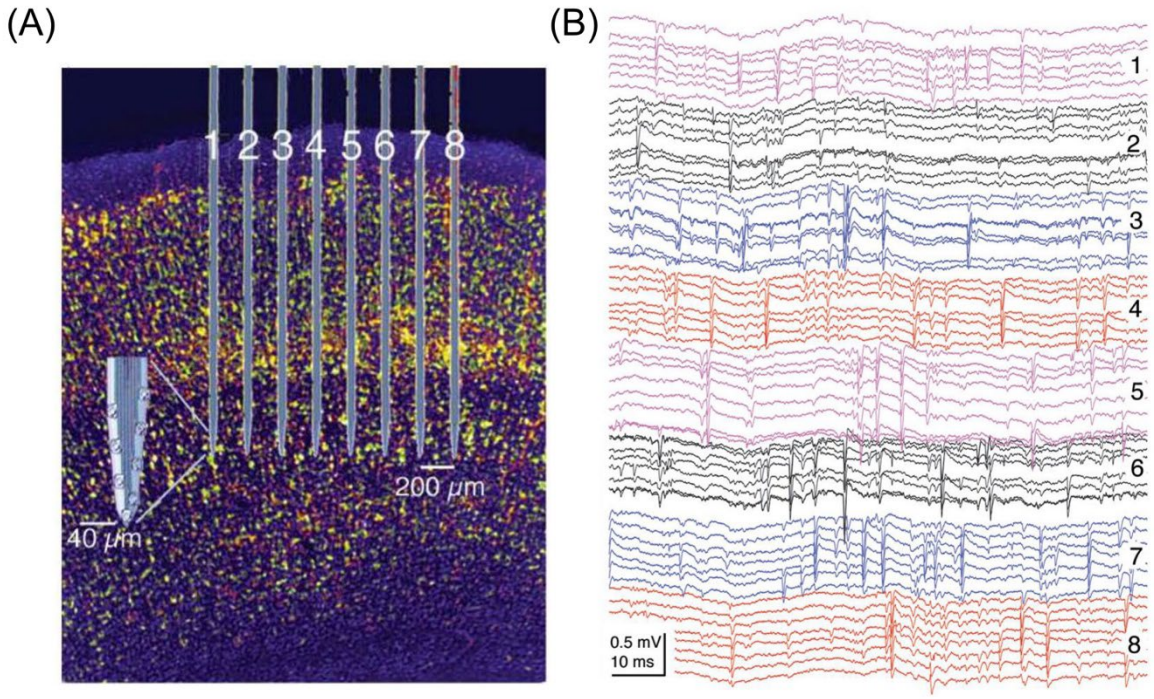

Figure 1.3 High-density recording of unit activity in the somatosensory cortex. (A) Placement of an eight-shank silicon probe with eight recording sites on each shank. (B) A short epoch of raw recording. Spikes are present across sites of the same shank but not across electrodes placed laterally across different shanks. Reproduced with permission from [38].

recorded from different types of neuronal populations, the microelectrode array should be oriented perpendicularly to the neural tissue layer along the axis of the neuronal cells. Single-shank planar probes can be oriented perpendicularly to planar sections of nervous tissues. However, curved laminated structures, such as in the CA1 region of the ventral hippocampus, generally require 3D recording architectures to position the recording sites perpendicular to the laminae. Current 3D microelectrode array designs include microassembled planar arrays transformed into a single 3D array [40, 41] or slanted Utah electrode arrays [42, 43]. Nonetheless, the trajectory of these architectures is still constrained to an orthogonal approach, and some deep structures remain inaccessible to targeted electrode recording or stimulation. Novel probe designs with unconventional trajectories could orient electrodes to regions in the brain that are understudied and further our mechanistic understanding of brain function.

1.6 Foreign body response to chronic penetrating microelectrode arrays

The central nervous system (CNS) is a complex and dynamic system that continuously adapts to environmental changes. It consists of an intricate network of neurons, glial cells, and immune cells interconnected through various pathways and feedback loops modulated by the extracellular matrix and signaling molecules such as cytokines, neurotrophins, and neurotransmitters [44, 45]. Under normal conditions, these coordinated interactions are essential for maintaining homeostasis and generating context-specific, appropriate physiological responses. Neuroimmune interactions, mediated by this interdependent network, regulate CNS activity and respond to injury or neuroinflammation to restore tissue homeostasis. While neuroinflammation can be protective, aiding tissue repair and recovery, dysfunctional or chronic neuroinflammation may become maladaptive, contributing to a cycle of chronic inflammation and neuronal injury [46].

The clinical application of intracortical microelectrodes necessitates interfacing with the CNS while maintaining long-term reliability and function. However, the recording performance of these microelectrodes declines over prolonged implantation periods [3]. Neuroinflammation following implantation has been identified as a significant factor impacting microelectrode performance [47, 48]. The immune system of the central nervous system is activated immediately after traumatic injury and remains responsive if it detects foreign materials in its environment. This phenomenon is referred to as the foreign body response (FBR). This tissue response alters the environment from which electrophysiological signals are obtained, leading to recording inaccuracy, instability, and failure.

Neuroinflammation after injury is classified into two main phases: acute and chronic responses. When a probe is inserted, it causes vascular disruption, activating microglial and immune cells within minutes to stabilize the injury and clear debris. In addition to microglia, oligodendrocytes and astrocytes are activated within hours, continuously releasing inflammatory signals during the first few days following the injury. This inflammation results in neuronal and glial cell death, peaking within 24 hours after the injury. Within 7 to 10 days, astrocytes surround the injured tissue, forming a glial scar. While this scar serves to protect neuronal cells from inflammatory signals, it also hinders neuronal regeneration near the injury site, ultimately leading to ~40% neuronal loss within 100 μm of the implant [49, 50].

Another mechanism that affects the performance of chronic intracortical microelectrode recording is neuroinflammation, exacerbated by damage to the blood-brain barrier (BBB). The integrity of the BBB deteriorates after microelectrode implantation due to neuroinflammation [51]. This deterioration increases BBB permeability, permitting blood-borne components, including bacteria and inflammatory proteins, to enter the brain, thereby amplifying the neuroinflammatory response at the implant site and influencing microelectrode performance [52].

The repercussions of these tissue responses on the performance of recording and stimulating microelectrodes result in increased impedance at the electrode-tissue interface. This impedance is inversely related to the specific geometry of the tissue that either generates the recorded potential or is activated by the stimulating electrode [53]. Lower tissue impedance leads to less attenuation of the recorded signal or stimulating current. Over time, as the glial sheath thickens and neurons move farther from the electrode surface, the impedance increases, and the signal amplitudes decrease [54, 55]. Additionally, the FBR contributes to the degradation of the physical device, resulting in the loss of electrode coating or insulation, as well as leakage or cracking [47]. Numerous systematic review articles describe how the interactions between neural implant materials and cells contribute to the development of FBR and impact the long-term functionality of microelectrodes [56-60].

1.7 Penetrating microelectrode arrays in epilepsy surgery

Electroencephalography (EEG) records electrical brain activity, typically with electrodes attached to the scalp surface. Electrocorticography (ECoG) electrodes obtain EEG recordings from the brain surface [61]. EEG signals acquired with stereotactic EEG (sEEG) use penetrating depth electrodes that target shallow and deep brain structures such as the hippocampus [62]. Most human ECoG or sEEG studies are conducted in patients with medication-resistant epilepsy. Identifying and surgically removing, i.e. resecting, the source of the seizures in the brain can completely suppress seizures [10, 11]. ECoG can precisely determine the origin of the seizures if the epilepsy originates in one region of the brain. If the onset of the seizure is unknown or thought to be in the brain's deeper structures, then sEEG is used.

The success of epilepsy surgery depends on correctly identifying the “epileptogenic zone,” defined as the minimal area of the cortex that must be resected to produce seizure freedom [63]. Choosing electrode trajectories that safely map the maximal area of brain tissue is critical for achieving

seizure freedom after surgery. However, recording deep brain structures, such as the hippocampus, remains challenging due to its anatomical features, orientation, and complex functional structure [64].

To perform sEEG, the patient is typically implanted with 8-20 semi-rigid cylindrical shafts containing 5-20 equidistant recording electrodes. [4] Each electrode has an exposed length of ~2 mm, diameters ranging from 0.8 to 2 mm, and is separated by a center-to-center distance of 2.5 to 10 mm. Shafts are inserted into millimetre-sized holes in the skull and penetrate the brain with different approach trajectories along the lateral (orthogonal) or longitudinal (parietal) axis (Figure 1.4).

The trajectory of depth electrodes is chosen to accurately sample the likely structures involved in seizure onset and the hypothesized functional networks they interact with [65]. Trajectories are selected to maximize sampling from deep cortical and subcortical areas. In most cases, trajectories are oriented orthogonally to correlate anatomical structures with the electrophysiological recordings. However, if multiple targets are accessible using a single non-orthogonal trajectory, an angled approach is selected to minimize the number of implanted electrodes [66]. After localizing the epileptic zone, the areas responsible for the seizures are entirely resected, depending on whether the brain regions can be safely removed.

The correct anatomical localization of all the implanted electrodes is mandatory to determine where the EEG signals are recorded (Figure 1.4) This process typically involves manually localizing 100 to 200 contacts per patient by visual inspection of post-implant CT scans. It is often incomplete and, in some cases, inaccurate, especially for non-planar trajectories. Ongoing research is dedicated to developing algorithms and user interfaces to estimate electrode positions accurately [67].

The multiple sEEG electrodes and trajectories currently required for resection of the epileptogenic zone can complicate sEEG surgeries and post-implant estimation of electrode positioning, pose risks of infection and discomfort to patients due to the number of open scalp wounds, and can’t access all deep brain structures [68]. In addition, a significant portion of patients continue to experience seizures after surgery, primarily due to significantly under-sampling the locations of potential seizure onset [69]. Neural interfaces with innovative architectures and trajectories

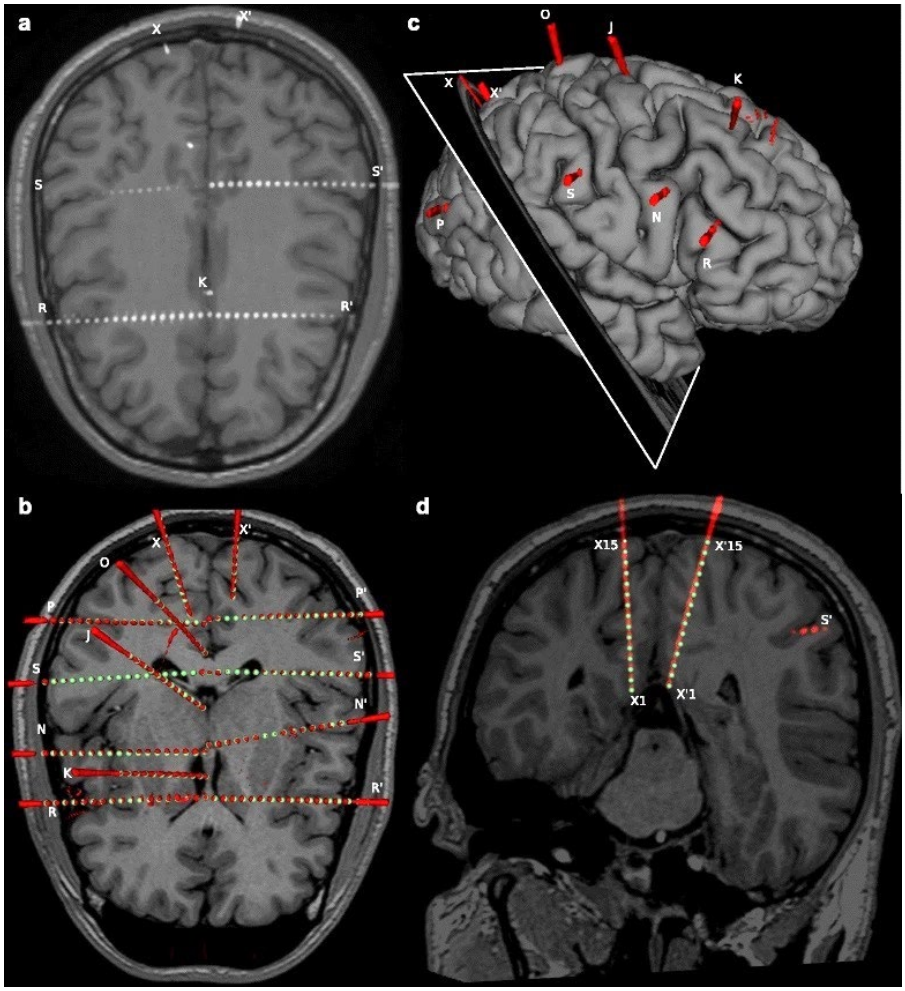

Figure 1.4 An example of sEEG implant trajectories illustrates the complex task of aligning non-planar electrodes with post-implant imaging data. (a) MRI and post-implant CT scans have lower resolution for sEEG implants along non-planar trajectories, resulting in artefacts (e.g. X and X') and typically require manual corrections. (b) Estimated coordinates of the electrode contacts generated using an algorithm to detect contact positions from post-implant CT scans. (c) Shows the right pial surface and the cut plane used in (d) where the example of X and X' electrodes are shown accurately segmented using a contact position estimator algorithm. Reproduced with permission from [67].

designed to record from complex structures in the human brain could considerably reduce the number of electrodes required in surgical interventions and record from critical regions that are currently inaccessible.

1.8 Research objectives

Technological advancements in intracortical microelectrodes have significantly improved the safety and efficacy of neuroprosthetics while advancing our understanding of brain function. However, progress in human brain recording relies on existing neurophysiological recording techniques utilized in patients undergoing neurosurgery for medical treatment. A major current challenge is achieving high-resolution spatiotemporal neural recordings from critical brain regions that are difficult to access. There is a significant gap in recording local and near-local network activities, for instance, within and among cortical regions that are likely central to the emergent properties that give rise to behavior. This issue relates not only to the density of electrodes but, equally critically, to the specific areas of the brain being sampled. For example, new neural probe architectures specifically designed for mapping critical deep brain areas with complex 3D structures, such as the hippocampus, could allow us to investigate network-level organization for the first time, with significant implications for advancing both basic research and clinical applications. The challenges encountered in epilepsy surgery, where intracranial recordings are performed (Section 1.7), illustrate a context in which new neurotechnologies could greatly advance human neuroscience and improve the treatment of neurological disorders.

Furthermore, current neural electrodes lack the long-term reliability necessary for clinical applications. The areas of most intense research focus on addressing how the quality of the electrical interface and the bulk material of neural devices contribute to high impedance. Conducting polymers, particularly poly(3,4-ethylenedioxythiophene) (PEDOT), offer unique advantages in enhancing electrode performance due to their versatile patterning capabilities, hygroscopic nature, and excellent ionic and electronic conduction properties.

The primary objective of this thesis is to present electrodeposited PEDOT-coated neural interfaces that improve electrochemical properties for long-term neural stimulation and recording. The stability of PEDOT, in comparison to other conducting polymers, is one of its main advantages. In pursuit of our objective, it is essential to investigate the stability of PEDOT-coated electrodes over extended periods in a biological environment and assess the foreign body response.

Therefore, the first objective is to enhance the electrical performance of neural electrodes coated with electropolymerized PEDOT:BF_4, confirm the stability of these PEDOT coatings, and evaluate the neuroinflammatory response. To achieve this objective, we:

- Verify the stability of electrodeposited PEDOT:BF_4 coatings on microwires coated with PEDOT:BF_4 under continuous stimulation for 24 hours in phosphate buffered saline (PBS) and evaluate the electrical performance using electrochemical impedance spectroscopy.
- Implant microwires coated with PEDOT:BF_4 in the rodent cortex and subject them to daily stimulation and subsequent impedance measurements, over a period of 60 days.
- Conduct histological analysis of the brain tissue surrounding the implants.

A second specific objective of this thesis was to create innovative neural interface architectures capable of mapping unexplored neural circuits within deep 3D brain structures and mitigating the foreign body response. To achieve this objective, we:

- Create flexible epidermal recording devices using PEDOT via screen printing, and assess their mechanical and electrochemical performance.
- Develop a neural probe constructed entirely from ultra-thin parylene by employing chemical vapor deposition (CVD) to apply the substrate and insulating layers.
- Design a novel curved microelectrode array featuring a probe curvature, electrode area, and pitch designed to target the ventral hippocampus. Employ lithography, electron-beam metal evaporation, lift-off, and reactive ion etching for device fabrication.
- Electropolymerize PEDOT:BF_4 onto the surface of gold microelectrodes and characterize the electrode surface using electrochemical impedance spectroscopy, cyclic voltammetry, and scanning electron microscopy.
- Create a silk shuttle to ensure the mechanical strength necessary for implanting the ultra-flexible probe. Use lithography and deep reactive ion etching (DRIE) to shape the tip and curvature of the shuttle by patterning 3D structures on a silicon wafer and transferring this pattern onto polydimethylsiloxane (PDMS). Introduce an aqueous silk solution into the PDMS mold to form a silk shuttle adhered to the probe.
- Design a custom rotating implantation device to interface with standard stereotaxic tools, enabling precise insertion of the probe along a curved path to accurately position the electrodes at the target coordinates.

1.9 Structure of the thesis

Chapter 1 provides background information on neural signals, describes the electrochemical basis for recording and stimulating neural populations with electrodes, and outlines the primary challenges affecting recording and stimulation performance. Chapter 2 reviews the history of penetrating microelectrode technology and the current advancements in flexible and unconventional neural device technology. Furthermore, it discusses the benefits of PEDOT in enhancing neural device performance.

Chapters 3 and 4 include reprints of two articles based on this thesis's research:

Article I Jo'Elen Hagler, Jeeyeon Yeu, Xin Zhou, Guillaume Ducharme, Bénédicte Amilhon, and Fabio Cicoira, "Electrodeposited PEDOT:BF_4 Coatings Improve Impedance of Chronic Neural Stimulating Probes In Vivo," *Advanced Materials Interfaces*, vol. 9, no. 35, p. 2201066, 2022.

Article II: Jo'Elen Hagler, ChiHyeong Kim, Pierre Kateb, Jeeyeon Yeu, Noémy Gagnon-Lafrenais, Erin Gee, Sofian Audry, and Fabio Cicoira, **"**Flexible and stretchable printed conducting polymer devices for electrodermal activity measurements," *Flexible and Printed Electronics,* vol. 7, no. 1, p. 014008, 2022.

In **Article I**, we examined the stability of electrodeposited PEDOT:BF_4 microwires when subjected to daily stimulation in the rodent cortex over 60 days. Our findings indicate the in vivo stability of PEDOT coatings under stimulation for the duration of the experiment, along with an assessment of acute and chronic inflammation in brain tissue resulting from the microelectrode implants. The impedance of the PEDOT coatings remained consistent throughout the testing conditions and durations. As expected for metallic microwires, inflammation was observed to be elevated around both PEDOT-coated microwires and the control at similar levels.

This discovery prompted a shift towards flexible bioelectronics. The main challenge associated with metallic neural interfaces lies in their rigidity, which causes substantial damage to brain tissue and culminates in functional loss months post-surgery due to the foreign body response (Section 1.7). Since identifying this issue, significant efforts have been focused on developing neural interfaces that utilize compliant materials. Epidermal, skin-based probes serve as examples of successful conformal, compliant probes that enable new functionalities. Therefore, in **Article II**, we explore the creation of flexible epidermal recording devices made from screen-printed

PEDOT:poly(styrene sulfonate) (PSS) on soft and stretchable polyurethane substrates. Additionally, we present the mechanical characterization, the electrochemical performance in PBS, and results from experiments assessing electrodermal activity from the surface of a human finger.

In Chapter 5, we present our findings regarding the development and implementation of a flexible neural device featuring an innovative architecture: the first curved neural microelectrode array. This device has been precisely designed to interface with the CA1 area of the ventral hippocampus, where achieving accurate electrode placement is particularly challenging. The device's flexibility is attained using ultra-thin parylene, with an overall device thickness of only 4 μm. The sixteen gold microelectrodes are coated with PEDOT:BF_4, which significantly reduces electrode impedance by two orders of magnitude. A silk shuttle provides the necessary mechanical strength for implanting the flexible curved probes. By rotating the curved probe during insertion along a circular path, we successfully positioned the electrodes perpendicular to the pyramidal layers of the dorsal and ventral hippocampus. We ultimately present the recorded signals from the dorsal hippocampus to demonstrate proof of concept for the initial use of the curved neural probe.

Finally, Chapter 6 offers a thorough discussion of the findings and their implications, while Chapter 7 summarizes the contributions of this multidisciplinary project, highlights its significant achievements, and proposes directions for future research.

CHAPTER 2 LITERATURE REVIEW

2.1 Electrode materials for neural recording and stimulation

Electrodes are a critical component of neural devices. All parts of these devices, including electrodes, must meet essential requirements for safety and functionality. Recording electrodes should achieve low interfacial impedance and maintain long-term stability of their structural properties. To maintain a high signal-to-noise ratio (SNR) over time, the material of the electrode material must not degrade or corrode in the biological environment. On the other hand, stimulation electrodes encounter challenges related to charge injection, including concerns for tissue safety and potential corrosion and degradation of the electrodes [70].

Electrode materials for recording and stimulation must possess high conductivity and effectively manage rising electrical impedance. Metals, particularly noble metals, are the primary conductors for neural electrodes and have been employed in neural interfaces for over 70 years [71, 72]. Noble metals and their alloys typically remain chemically inert over chronic timescales. Conventional microelectrode materials include gold [73], platinum [24], platinum-iridium [74, 75], titanium [76], titanium nitride [77], iridium [78, 79], iridium oxide [80-82], stainless steel [83], and tungsten [84, 85]. However, as the dimensions of conventional metallic electrodes are reduced for spatial selectivity, the impedance increases dramatically (~1 MΩ). Additionally, some materials, such as platinum, tungsten, and iridium oxide, can undergo dissolution and corrosion when stimulated [70, 86-88].

Both electrochemical and biological factors influence electrode performance, making it extremely challenging to select electrode materials that encompass all desirable properties. One strategy to reduce the impedance of conventional smooth metallic electrodes is to increase the roughness of the electrode surface, such as with nanostructured platinum [89] or gold nanoparticle [90] electrodes. These methods demonstrate good stability and have a well-established preparation process. Conducting polymers, particularly PEDOT, serve as a coating material to enhance the electrochemical surface area, offering unique advantages for improving long-term recording quality and high charge injection capacity [91-94]. Section 2.5 discusses PEDOT coatings for enhancing neural interfaces, while Chapters 3 through 5 present the stability and performance results of PEDOT.

2.2 Microwires

The single microwire electrode is the most commonly used electrophysiological neural interface. Utilizing microwires to monitor electrical activity and stimulate neurons in deep brain areas has contributed to our understanding of sensory and motor functions. The first recordings from individual neurons using metallic wire electrodes occurred in the 1940s. A pioneering study employed Ag/AgCl wire electrodes to detect electrical signals from single neurons [95]. Subsequently, materials like stainless steel and tungsten emerged as more effective and safer options for chronic recording applications [96, 97]. In the 1950s, electrolytic pointing was used to create sharpened stainless steel microwires, which reduced electrode variability and facilitated insertion into cortical tissue [98]. Initially, devices were limited to recording for only a few hours to days. However, in the 1970s, the introduction of microwire electrodes made from iridium (Ir), platinum (Pt), and platinum-iridium alloys (Pt/Ir) enabled recordings that lasted more than 200 days after implantation [79, 99].

Microwire-based microelectrodes consist of conductive materials formed into thin wires through an extrusion process [100] and are coated with insulating layers along their length. For high-density, long-term recordings, microwires typically have a diameter of <20 μm to minimize tissue damage and improve chronic single-unit recordings. The insulation around the microwire ensures that only the tip is exposed for recording neural signals, thereby improving signal specificity, which is essential for maintaining recording quality by capturing signals solely from the microwire tip while ensuring biocompatibility. Common insulation materials for microwires include Parylene-C and polyimide [101, 102]. Today, several companies such as Microprobes and Plexon provide microwire technologies commercially.

Despite various advancements, a major challenge for microwires remains the reliable recording of high-quality data over time. Furthermore, while microwires can effectively target individual neurons, investigating the collaborative activity of neuronal groups requires the simultaneous observation of many neurons. To accomplish this, two key criteria must be met: (1) accurately placing multiple recording electrodes within a small tissue volume with submillimeter precision and (2) minimizing tissue damage.

In regions with a high density of neurons, isolating individual neurons using single wires is challenging. A single electrode tip captures similar amplitude spikes from multiple neurons at the

same distance, complicating single-cell isolation. By employing two closely spaced electrodes, neurons within a plane can be identified, while three electrodes focus on neurons arranged in a line. Including a fourth electrode in a different plane enables 3D spatial separation of neurons through triangulation. The concept of triangulating biological voltage sources originated from studies of the heart. The heart 'tetrode' requires four electrodes positioned on the body to accurately pinpoint anatomical sources of voltage, which is a standard method for analyzing electrocardiograms. This technique can effectively localize any stationary dipoles, such as neural action potentials. The first neural "tetrode" consisted of four thin wires (12 μm in diameter each) that were twisted and glued together [103]. Wire tetrodes offer numerous advantages over sharp-tip single electrodes, including low-impedance recording tips and improved mechanical stability [104, 105]. Under ideal conditions, a tetrode can record signals from up to 20 well-isolated neurons [35].

2.3 Planar microelectrode arrays

The invention of lithographically based planar processes in 1959 enabled the fabrication of microelectronic integrated circuits [106]. The new technology was soon adapted to other fields, such as miniaturized sensors and actuators. By 1966, researchers at Stanford University had adopted microfabrication techniques for developing high-density microelectrode arrays for extracellular action potential recording [2]. As MEMS technology advanced, the established knowledge and equipment from the microelectronic industry were directly applied to silicon-based probe formation. Silicon can be precisely shaped to create only a few micrometers wide probe structures, with high yield and reproducibility. In 1981, Kensall Wise and his team at the University of Michigan began developing 2D and 3D silicon probes (Figure 2.1) that soon became ubiquitous in neuroscience research, known as the Michigan probe [40, 41, 107-109]. In 2004, they formed the company NeuroNexus, which offers microelectrode arrays with up to 256 recording sites and custom electrode dimensions and designs. Michigan probes are the current state-of-the-art planar neural microelectrode arrays and have reduced the price of high-density electrode neural probes from over $250,000 to less than $10,000.

Fabrication of silicon probes is performed using bulk micromachining processes. The micromachining of silicon probes has evolved and varies for different applications. DRIE and slow diffusion-boron etching can produce a probe of arbitrary 2D shape, not dependent on wafer crystallography [40, 110]. The overall process to fabricate the traditional Michigan probe (Figure

2.1(A and B)) uses a merged bulk-micromachined 2P/1M CMOS process involving 16 masking steps [107, 108, 111]. Alternative methods have been developed to simplify silicon probe fabrication and reduce the overall size of 3D microassembled Michigan probes (Figure 2.1C) [112]. Both methods follow similar processing steps but deviate based on whether deep reactive ion etching (DRIE) or boron diffusion etch stops are used to etch and release the final silicon probe.

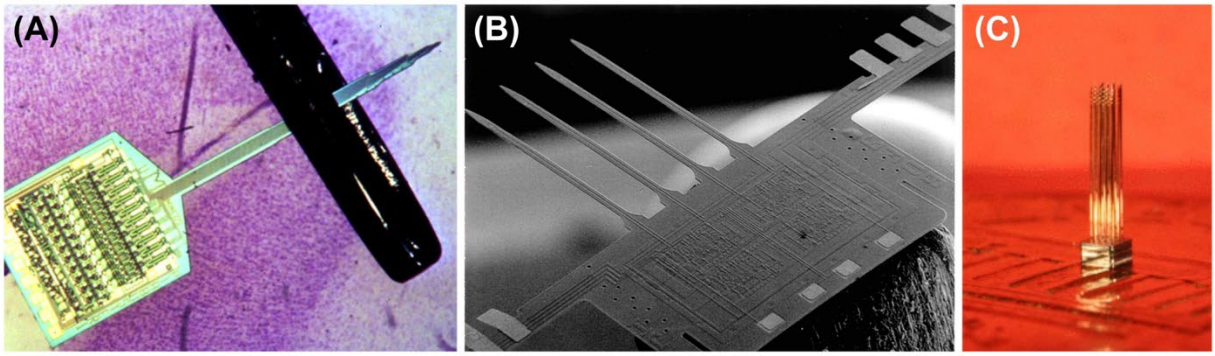

Figure 2.1 Architecture of Michigan arrays. (A) Single and (B) multishank arrays processed using boron diffusion etching and (B) microassmebled 3D arrays etched by DRIE. Reproduced with permission from (A) [111], (B) [107], and (C) [41].

Typically, silicon probe fabrication starts with a p-type monocrystalline silicon or a silicon-on-insulator (SOI) wafer. An insulating layer of silicon dioxide or nitride is deposited to insulate electrical components from the silicon shank. The oxide is patterned lithographically and later removed to define the probe tip and overall shape. Next, thin films of conductors (e.g. gold, platinum) are evaporated and patterned by lift-off. If DRIE is used to etch the silicon, an etch-stop layer is deposited to protect the metallic layers during plasma etching. Then, front side DRIE etches the top oxide layer to expose the areas outside the shank perimeter, pads, and recording sites, stopping at the buried oxide layer of the SOI. Finally, the backside DRIE removes the bottom silicon layer, releasing the probe shanks [112]. If deep boron diffusion etch stops are used, the probe perimeter is first defined with deep boron diffusion, followed by a shorter boron diffusion step to define the tip. An insulating layer of silicon oxide/nitride/oxide is deposited on top of the interconnects, followed by RIE to expose the recording sites and pads. Finally, the probe is released with isotropic wet etching where all areas of the wafer, not defined by boron diffusions, are etched away [108].

2.4 Utah electrode array

Researchers at the University of Utah began developing a penetrating microelectrode array in 1991, initially to interface with the visual cortex for cortically based visual prosthetics. The Utah electrode array (UEA) was designed to overcome the limitations of planar cortical neural interfaces, which, at the time, were based on a large substrate with long lead wires that caused issues closing the skull after implantation, compromising the stability of chronic recordings. As such, new manufacturing techniques were needed to build the UEA [113]. The UEA silicon-based array consists of 100 penetrating electrodes on a thin substrate, which facilitates skull closure after implantation, making it uniquely suited for cortical implantation (Figure 2.2). The UEA has been used in some of the most extended chronic implants to date and is now manufactured by BlackRock Neurotech to record from the motor cortex in humans to control muscle movement using brain-computer interfaces [114].

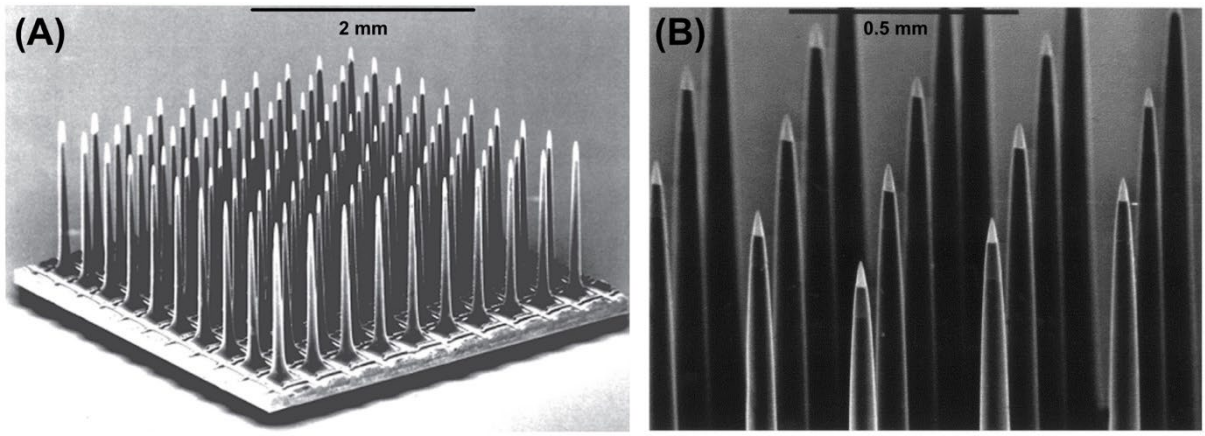

Figure 2.2 The Utah electrode array. SEM of (A) 100 microelectrodes projecting from a 4 mm x 4 mm silicon substrate and (B) platinum-coated tips. Reproduced with permission from [115].

The device is micromachined from silicon to build the UAE architecture using glass reflow, dicing, and etching [115, 116]. First, a dicing saw cuts grooves on the surface of squares cut from p-type silicon <100> wafers in the two orthogonal directions parallel to the sides of the square. Using a glass reflow process, a layer of glass is melted on top of the silicon square to fill the grooves and create insulating regions. The platinum bond bands for wire-bonding were deposited using standard lithography techniques on the glass squares between the grooves. A dicing saw is used to cut two orthogonal sets of cuts into the side without glass deep enough to barely cut into the glass, leaving

tall square silicon columns separated by a layer of insulating glass. The square piece is then cut into individual arrays and subjected to two acid etching steps to taper the columns. The array is slowly rotated for the first acid etch while mounted and suspended in a stirred acid bath to thin the columns without changing the shape. The array is placed at the bottom of a container of acid to sharpen the tips, with the columns positioned upward. The solution is not stirred, resulting in reduced activity of the etching solution at the column base and preferential etching at the top, resulting in a sharp, polished needle.

A platinum or iridium oxide layer is selectively deposited on the tips by pushing the electrode shanks through a thin square of aluminum foil and evaporating or sputtering the conductive material. An insulating layer of Parylene-C is coated onto the shank and de-insulated by masking below the tip with aluminum foil and subjecting the tips to reactive ion etching [117]. Finally, the electrode arrays were wire-bonded using insulated wire. The final shank has a diameter of 80-100 um at the base, a radius curvature of two to three microns at the tip and a length of 1.5 mm. The array's substrate is only 200 um thick, providing a thin profile sitting close to the cortex, allowing for skull to close after implantation [115].

2.5 Unconventional architectures and form-factor probes

Connecting rigid microelectronics to the soft, dynamic environment of the brain presents significant challenges. Ongoing research addresses the limitations of conventional implanted electrodes, whose rigidity often leads to device encapsulation and reduced recording and stimulating capabilities. Neural probes designed to match the brain’s flexibility, softness, and movements can adapt to its motions [57, 118]. These advanced neural probes feature smaller dimensions and more flexible materials, often diverging from traditional designs and insertion techniques [119].

Flexibility is typically quantified by Young’s modulus, which evaluates a material's stiffness and its ability to resist elastic deformation. Softness, in contrast to hardness, refers to a material’s capacity to deform when subjected to force applied to a point on the surface. When the stiffness and softness of an implanted object significantly diverge from that of the brain, the result can be a force generated between them during asynchronous movements, potentially causing ongoing inflammation and immediate injury [120]. Probes made from polymer materials featuring a lower

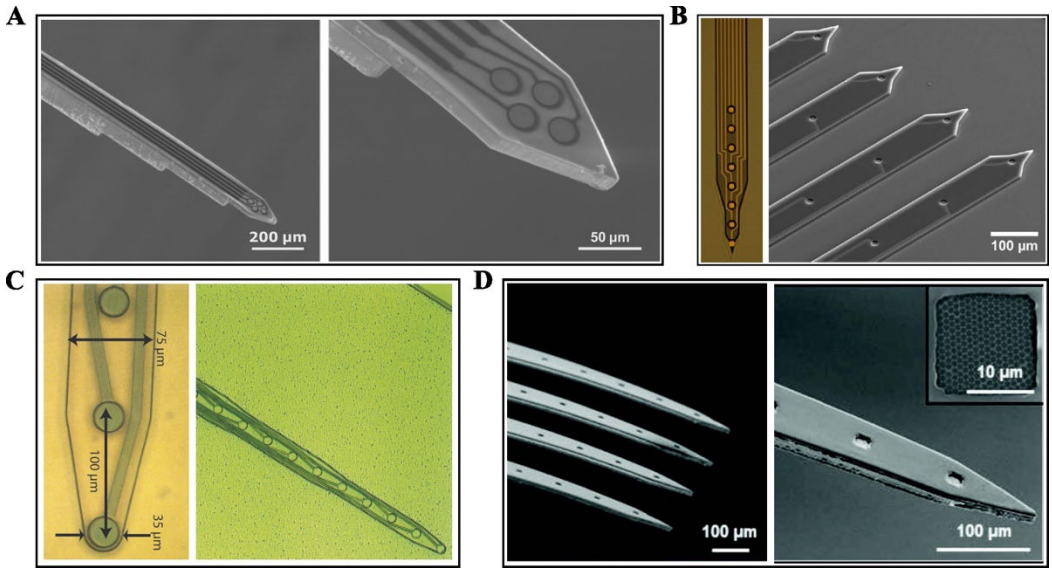

Figure 2.3 Flexible polymer neural probes. **A** SU-8, **B** Parylene-C, **C** Polyimide, **D** Parylene/SU-8. Reproduced with permission from **A** [125], **B** [126], **C** [127], and **D** [94].

Young's modulus can improve softness and flexibility. Flexible neural probes (Figure 2.3) have been developed using polymers such as parylene-C [121, 122], SU-8 [123], and polyimide [124].

Flexible polymers typically exhibit lower stiffness and hardness compared to silicon and metal, yet they have a Young's modulus that is several magnitudes higher than that of brain tissue. Research indicates that the mechanical mismatch between inserted probes and tissue should consider additional material properties, including the compliance of the probe. Compliance corresponds to a material's bending stiffness and relates to an elastomer's ability to deform when subjected to external forces. Greater compliance in a probe leads to reduced force on the tissue. The bending stiffness of a material is directly proportional to its width and the cube of its thickness [128]. Therefore, smaller probes made from identical materials will enhance mechanical properties.

Ultra-small flexible electrodes exhibit excellent compliance, featuring innovative designs aimed at optimizing tissue-probe integration and facilitating high-density, long-term neural recordings. Recently, a single long probe made from a syringe-injectable 3D mesh of SU-8 ribbons (Figure 2.4A), 1.5 µm thick and 10 µm wide, was implanted across four brain regions in both hemispheres. A study published this year introduced NeuroRoots (Figure 2.4B), which consist of multiple parylene-based microelectrode "roots," each 7 µm wide and 1.5 µm thick, clustered into tetrode formations and self-assembled around a microwire. These electrode roots mimic the compliance,

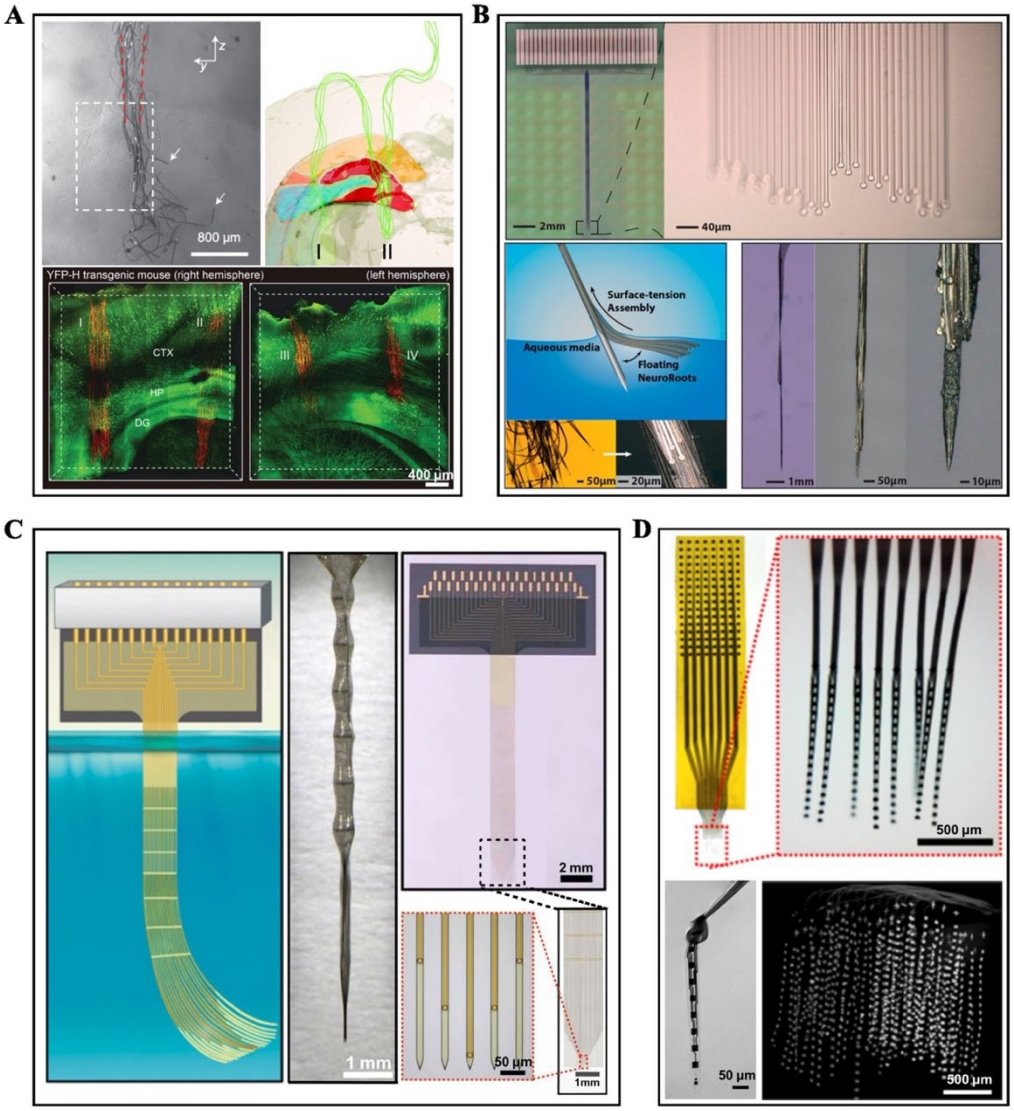

Figure 2.4 Ultraflexible neural probes. **A** Syringe injectable 3D mesh constructed from 10 µm wide, 1.5 µm thick SU-8 ribbons implanted into four brain regions across both left and right hemispheres. **B** NeuroRoots: Parylene-C devices consisting of independent microelectrode 1.5 µm thick and 7 µm wide "roots," organized into clusters of tetrodes. **C** Neurotassels: A polyimide-based microelectrode array composed of individual filaments with a 3×1.5 µm^2 cross-sectional area arranged in a plane-mesh structure. **D** NET: Nanoelectronic thread electrodes arranged in 3D arrays of individual 1 µm thick, 35 µm wide shanks based on SU-8. Reproduced with permission from **A** [129] and [130], **B** [131], **C** [132], and **D** [133] and [134].

spatial arrangement, and dimensions of axons. Meanwhile, Neurotassels (Figure 2.4C) consist of polyimide high-density microelectrode arrays and feature neuron-sized filaments (1.5 µm thick and

3 μm wide) with a plane-mesh design. These filaments are organized around a microwire through elastocapillary self-assembly. Recent volumetric mapping of neural networks has been accomplished using 3D microelectrode arrays (Figure 2.4D) made from 1 μm thick and 30 μm wide SU-8 nanoelectronic threads (NETs). These threads have demonstrated successful chronic recordings and minimal tissue inflammation over months of implantation.

The most unconventional geometries present significant challenges for implantation. A major limitation of flexible polymeric neural probes is their low buckling strength, which complicates their insertion into the brain, causing them to bend instead of being properly implanted. However, various strategies can help mitigate this issue, such as coating the probe with polyethylene glycol [135], or silk [136-139], or using mechanical carriers to guide the probe to the targeted brain area [140-142].

Advanced implanted neural devices facilitate long-term, minimally invasive neuronal recording and stimulation by utilizing soft materials, innovative device architectures, and varying feature sizes in each design. Future directions should prioritize maximizing safety and efficacy to develop the most reliably stable and biocompatible chronic interfaces that address neuroscientific and clinical needs, thereby advancing treatments for brain diseases.

2.6 PEDOT neural interfaces

2.6.1 Conjugated polymers

Organic conjugated polymers are electrically conducting polymers that can reach metallic-like conductivity in their oxidized form. The dynamic control of the coupling between ionic and electronic charge species in conjugated polymers has been widely utilized in various electronic applications such as organic electrochemical transistors [143] and organic light-emitting diodes [144].

Conjugated polymers are carbon-based semiconductors characterized by alternating single and double carbon-carbon bonds along the polymer backbone. The electronic configuration of carbon ($1s^2 2s^2 2p^2$) allows carbon atoms to form up to four covalent bonds. A double bond forms between carbon atoms through sp^2 hybridization, the mixing of the 2s orbitals with the $2p_x$ and $2p_y$ orbitals of adjacent carbons, resulting in three planar σ bonds and a single π bond with the third unhybridized $2p_z$ orbital located above and below the molecular plane (Figure 2.5(A,B)).

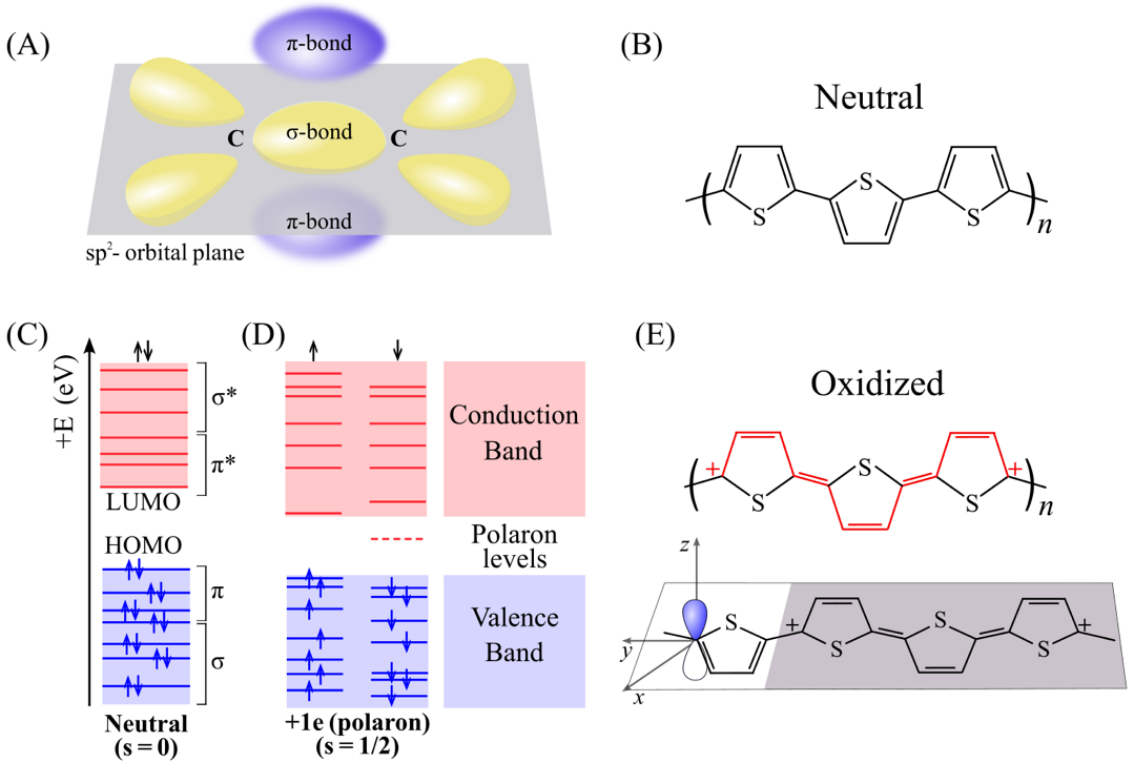

Figure 2.5 (A) Schematic illustrating σ bonds and π bonds between two sp^2-hybridized carbon atoms. (B) The chemical structure of a conjugated polymer (polythiophene) showing the alternating single and double bonds. (C) The electronic structure of a conjugated molecule with occupied σ and π orbitals and unoccupied σ^* and π^* orbitals and (D) the polaron states when a positive charge is added to the polymer chain. Occupied electronic levels in the valence band are shown in blue, with arrows representing electrons. The empty electronic levels in the conduction band are shown in red. The dashed red line represents unoccupied polaronic levels. (E) A charged conjugated polymer, in which 2+ charge is localized on three monomers (top) and a side-view showing the π-electronic densities perpendicular to the planar σ bonds. Adapated from (B and E) [145] and (C and D) [146].

Conjugated polymers consist of a continuous chain of sp^2-hybridized carbon atoms with overlapping p_z orbitals. The stability of the carbon chain arises from the strength of the σ bonds that form the backbone of the polymer. The overlapping p_z orbitals along the chain of atoms leads to the formation of delocalized π orbitals. These π orbitals form the highest occupied molecular orbital (HOMO) and the lowest unoccupied molecular orbital (LUMO) (Figure 2.5C). The π electronic density of two neighboring molecules can interact weakly, leading to the formation of electronic bands, with filled π bonding orbitals forming the valence states and the empty π^* antibonding orbitals creating the conduction states [147]. The delocalized π electron system

provides conjugated polymers with essential properties such as a small electronic band gap leading to low-energy electronic excitations, polymer chain oxidation or reduction through charge transfer with dopants, and large charge carrier mobilities that can achieve high electrical conductivities in the doped states.

Adding excess doping charges to the conjugated polymer chain creates new electronic states within the π band gap (Figure 2.5D) [145]. Conjugated polymers are generally classified as either *p*-type, acting as electron donors with low ionization potentials that are easily oxidized, or *n*-type, serving as electron acceptors with high electron affinities that are easily reduced. Excess doping charges tend to concentrate in specific areas, giving rise to singly and doubly charged quasi-particles called polarons (charge of ±1) and bipolarons (charge of ±2, Figure 2.5E). These quasi-particles are associated with localized alterations in the atomic lattice, marked by changes in bond length alternation and the emergence of new electronic states in the band gap due to strong electron-phonon coupling [148]. Electroneutrality in conjugated polymers is achieved through the intercalation of anions or cations within the bulk of *p*-doped or *n*-doped conjugated polymers, facilitated by weak interchain interactions governed by van der Waals forces, electrostatics, and π – π interactions.

2.6.2 PEDOT

Poly (3,4-ethylenedioxythiophene) (PEDOT) is a polythiophene derivative featuring two alkoxy groups at the 3 and 4 positions (β) of the thiophene ring, connected by an ethylene (C_{ether}) (Figure 2.6A). The 3 and 4 positions, being farther from sulfur, experience less steric hindrance and are less susceptible to electrophilic attacks compared to the 2 and 5 positions (α). Additionally, the electron-donating oxygen atoms stabilize free radicals and positive charge carriers within the conjugated backbone. Consequently, PEDOT demonstrates remarkable air stability in its doped state and exhibits high electrical conductivity [149].

Typically, PEDOT is *p*-doped, meaning the charge carriers consist of positively charged polarons or bipolarons, which remove electrons from the polymer chains. In *p*-doped conjugated polymers, the polaron (with charge q = +1e and spin s = 1/2) represents a hole localized across several monomer units. A bipolaron, characterized as a localized spin-degenerate quasiparticle (q = +2e and s = 0), forms when two holes with opposite spins occupy the same energy level. Bipolaron formation occurs when the energy gained from the electron−lattice interaction exceeds the energy

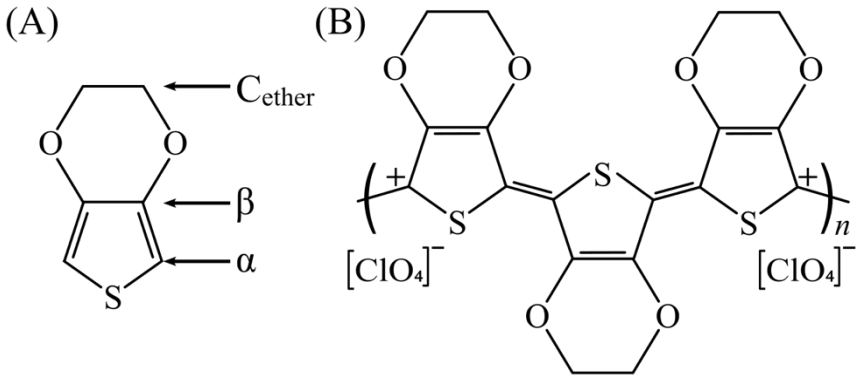

Figure 2.6 Structure of PEDOT. The chemical structures of (A) EDOT and (B) a charged PEDOT molecule, in which 2+ charge is localized on three monomers and is charge-balanced by two *p*-type dopant anions (ClO_4^-). Reproduced with permission from (A) [150] and (B) [145].

from the Coulomb repulsion between two charges of the same polarity [146]. When a potential is applied, polarons and bipolarons can migrate along the conjugated chain by hopping between neighboring molecules. In a *p*-doped PEDOT film that is charge-balanced with counteranions (Figure 2.6B), both electronic and ionic charge carriers exhibit mobility, which leads to mixed conduction properties vital for numerous applications.

2.6.3 Synthesis of PEDOT

PEDOT is the product of the polymerization of 3,4-ethylenedioxythiophene (EDOT) monomers, which can be synthesized through chemical or electrochemical methods. Anodic electropolymerization is one of the main electrochemical techniques for producing conducting polymers, allowing for the direct deposition of doped conducting polymers onto micro-sized or 3D electrode surfaces while offering precise control over the film thickness. The electrochemical synthesis of PEDOT involves a reaction sequence that requires two electrons per molecule for each coupling step [151]. This film-forming process starts with the oxidation of the neutral EDOT monomer at the anode, leading to the formation of a radical cation [152]. Two radicals then couple to form a dimer, which combines with additional monomeric radicals to create an insoluble oligomer comprising 6 to 20 EDOT monomers [153] that precipitate onto the electrode surface. The deposition of the polymer then continues through nucleation and growth processes [154].

The electrochemical setup typically consists of a three-electrode system: a working electrode, a reference electrode, and a counter electrode, all placed in a solution containing dissolved EDOT, the counter-ion, and the solvent. Potentiodynamic (cyclic voltammetry), galvanostatic (constant current), or potentiostatic (constant potential) techniques can be used to electrosynthesize a conducting polymer [29]. In potentiodynamic polymerization, a cyclic change of the electrode potential is applied during the deposition of the polymer onto the electrode, alternating between neutral and doped states, accompanied by a continuous exchange of electrolyte and solvent [155]. At the end of potentiodynamic polymerization, the deposited PEDOT is generally obtained in its neutral state. The galvanostatic method is characterized by an increase in potential for a few seconds after the onset of the current, depending on the applied current density, followed by a decrease [156]. Current control leads to a constant polymerization rate and control over the film thickness [157]. The potentiostatic method is characterized by significant changes in current and polymerization rate. Both potentiostatic and galvanostatic methods produce PEDOT in its doped state. The morphological and electrochemical properties of the deposited PEDOT film vary significantly with the synthesis technique, the formation potential, solvent, and counterions used in the polymerization [158, 159].

2.6.4 Advantages of PEDOT for neural interfaces

Achieving single-unit isolation in neural recordings or localized neural stimulation requires targeting neurons with high spatial resolution. While reducing electrode size improves resolution, it also decreases capacitance and increases impedance. As discussed in Section 1.4.1, elevated electrode impedance raises thermal noise and hinders charge transfer, which compromises both signal quality and stimulation efficacy. A key advantage of PEDOT in neural devices is its combined electronic and ionic conductivity, along with a high surface area. The porous nature of PEDOT coatings improves the conductive surface, enabling efficient transport of electronic and ionic charges to neural tissue [160]. This results in significantly lower impedance while maintaining a small electrode area.

Since the pioneering research by Martin and Cui in 2003 [161], PEDOT neural electrodes have been used in vivo to record and modulate neuronal signaling due to their stability in aqueous environments, biocompatibility, and superior recording and stimulation abilities. The improvement in long-term recording performance was linked to a reduction in impedance and associated thermal

noise, initially shown by Kip and colleagues in 2006 [162, 163]. Various counterions have been employed in PEDOT neural electrode coatings, with PSS being the most common [164]. Other counterions that enhance electrochemical performance and have been used for long-term neural recording and stimulation include ClO_4, pTS, carbon nanotubes, and BF_4. The choice of counterion (X^-) and the electrode underlayer (e.g., Au, Pt, IrOx) impacts the morphology of the PEDOT film and its electrochemical performance. Generally, electrodeposited PEDOT:X^- on neural microelectrodes (<150 μm diameter) exhibits an impedance at 1 kHz that is ≈100 times lower than that of the bare electrode when tested in PBS [165]. A comprehensive discussion on stimulation and recording performance is found in Chapters 3 and 4, as well as in several excellent reviews [165-168].

CHAPTER 3 ARTICLE 1: ELECTRODEPOSITED PEDOT:BF_4 COATINGS IMPROVE IMPEDANCE OF CHRONIC NEURAL STIMULATING PROBES IN VIVO

3.1 Authors

Jo'Elen Hagler[1], Jeeyeon Yeu[1], Xin Zhou[1], Guillaume Ducharme[2,3], Bénédicte Amilhon[2,3], and Fabio Cicoira[1]

[1] Department of Chemical Engineering, Polytechnique Montréal, Montréal, Canada

E-mail: fabio.cicoira@polymtl.ca

[2] Départment de Neurosciences Université de Montréal, Montréal, Canada

[3] CHU Sainte-Justine Research Center, Montréal, Canada

E-mail: benedicte.amilhon@umontreal.ca

Published October 19, 2022*, Advanced Materials Interfaces*

3.2 Abstract

Resulting from its many unique properties, such as mechanical compliancy, electrochemical stability, and high conductivity, the conducting polymer poly(3,4-ethylenedioxythiophene) (PEDOT) is a promising material for improving the stimulation efficiency of neural microelectrodes. The long-term electrochemical stability of penetrating PEDOT-coated electrodes undergoing high-frequency stimulation is not extensively studied in vivo and the inflammatory response of the brain to PEDOT-coated stimulating neural probes is not well understood. In this work, electropolymerized PEDOT doped with tetrafluoroborate (PEDOT:BF_4) is selectively deposited on the tip of platinum iridium (PtIr) neural probes and implanted for 2 weeks and 2 months to evaluate the effect of implantation on the electrical performance, and the foreign body response to the probes. Histological evaluation after 8 weeks of implantation reveals no difference in the degree of inflammation around PtIr and PEDOT probes. Additionally, PEDOT and PtIr probes are implanted for 60 days, subjected to daily high frequency stimulation and are monitored for changes in electrochemical properties. Impedance measurements reveal an overall lower impedance for PEDOT probes. These results indicate that PEDOT:BF_4 coatings offer a promising approach for improving the stability of neural interfaces for stimulation.

3.3 Introduction

Electrical stimulation of neurons via neural prostheses, for example, deep brain and spinal cord stimulators, restores motor function after damage from trauma or disease [169-171]. Penetrating probes, implanted deep into neural structures, require low-impedance at the electrode-tissue interface to maintain efficient charge injection during stimulation [160]. The impedance of the electrode sites of neural probes steadily increases with time during implantation due to the immune system's response to the insertion of the probes into tissue [172]. Conducting polymers have been widely explored as coatings for stimulating neural probes to reduce the impedance at the electrode-tissue interface [173, 174]. Among conducting polymers, poly(3,4-ethylenedioxythiophene) (PEDOT) has significantly contributed to improving the electrical stability of neural probes due to its high conductivity, electrochemical stability under chronic exposure to biological environments, and compliant mechanical properties which provide a softer interface between brain tissue and stiff probes [175-177].

The stability of PEDOT coatings on the electrode sites of neural probes is critical for ensuring the long-term functionality of the neural device [178]. One major mode of PEDOT coating failure is through coating delamination or cracking [179-182]. The coating must be able to survive mechanical stresses, swelling, and electrode corrosion in order to be considered for use in clinical applications [183]. Substantial improvements in PEDOT stability have been achieved through tuning the polymerization parameters, accurately selecting dopants and solvents used for polymerization, and incorporating additives into the PEDOT film [177, 184-187].

Chronic stability of PEDOT-based recording neural electrodes has been extensively studied and reviewed [57, 93, 175, 186, 188-194]. Studies of PEDOT coating stability under stimulation have been recently reviewed [174, 183, 184]. In one study, electropolymerized PEDOT, containing carbon nanotubes on Pt microelectrodes, was monitored over 3 months of soaking in phosphate buffered saline (PBS) with and without stimulation, and were reported to have stable impedance [195]. An in vivo study stimulated the Au electrode sites of a neural probe coated with PEDOT and carbon nanotubes for 1 h a day for 10 days (20 mA, 200 Hz). PEDOT demonstrated similar impedance values to Au electrode sites at the end of the study [196]. On the other hand, PEDOT doped with tetrafluoroborate (PEDOT:BF_4) electropolymerized on platinum iridium (PtIr) neural probes was implanted for 15 days, stimulated daily for 90 min (20 mA, 130 Hz) while monitoring

the impedance. At the end of the implantation period, PEDOT coated probes had a lower impedance than PtIr. However, the number of subjects were too small to derive statistical significance (n = 2) [185]. PEDOT coatings on neural microelectrodes is known to improve electrode performance and is stable under stimulation in vitro [195], but long-term in vivo experiments of PEDOT coated probes subjected to stimulation are lacking and are critical for assessing the potential of this organic polymer for clinical applications.

There exist few studies that include histological analysis of brain tissue chronically exposed to PEDOT, and most studies are done on recording neural probes [188, 190, 191]. One study reported immunohistochemical data of the tissue response of the brain after 12 weeks of being implanted with flexible polyimide probes containing Pt microelectrodes sites coated with PEDOT doped with poly(sodium 4-styrenesulfonate) (PEDOT:PSS) and PEDOT doped with the anti-inflammatory drug Dexamethasone (Dex) [197]. The study observed lower intensities corresponding to astrocytic scar tissue and macrophages/microglia for tissues in contact with PEDOT:PSS and PEDOT:Dex, however these differences were not statistically significant. Recently, long-term histological data from the muscle [198] and cochlea tissue [199] of rats exposed to PEDOT-based polymers was evaluated. Muscle tissue implanted with a soft wire made of an elastomeric conducting polymer composite consisting of a PEDOT-polyethylene glycol copolymer, silicone, and carbon nanotubes, was compared to muscle tissue implanted with a stainless-steel wire. The immunohistochemical analysis showed significantly less macrophages and scar tissue around the softer PEDOT wire. The cochlea tissue was implanted with a PEDOT hydrogel-coated Pt electrode array and stimulated over 5 weeks and the tissue inflammation was compared to cochlea tissue implanted with smooth Pt electrodes. The histological evaluation of tissue surrounding implanted PEDOT electrodes showed particulate polymeric material corresponding to delaminated PEDOT and significantly more widespread fibroblasts compared to the cochlea adjacent to Pt.

In this study, electrodeposited PEDOT:BF_4 was selectively deposited on PtIr neural microelectrodes. PEDOT coated and uncoated PtIr neural probes were implanted intracerebrally in mice for 2 weeks and 2 months to monitor the electrical performance and to evaluate the short- and long-term foreign body response. The histology analysis was performed on tissue sections that contained the PEDOT coated microelectrode. We observed no statistically significant difference between the inflammation intensity in tissue surrounding PEDOT and PtIr probes. Notably, the histology evaluation revealed that PEDOT coatings did not adversely affect inflammation when

compared to PtIr, suggesting that rigidity of the underlying PtIr is the main factor driving the foreign body response. Additionally, PEDOT:BF_4-coated PtIr probes were implanted for 60 days and subjected to daily stimulation and electrochemical impedance measurements to assess the electrical stability of the coatings under chronic implantation and stimulation. During the 60 days of implantation and stimulation, PEDOT probes provided an overall lower mean impedance magnitude when compared to PtIr. PEDOT:BF_4 coatings on neural microelectrodes show promising performance and stability, and offer a valuable approach for improving neural interfaces.

3.4 Electrochemical measurements in vitro

The electrochemical stability of PEDOT coated probes exposed to phosphate buffered saline solutions (PBS) and subject to 24 h of stimulation with biphasic current pulses at an of amplitude of 20 µA per phase (18.4 µC cm^{-2} per phase) at a frequency of 100 Hz was investigated. Impedance measurements were performed before and after the stimulation protocol. After stimulation, the impedance magnitude at 1 kHz (Figure 3.1) shows a statistically significant decrease of 14.3 Ω in the mean impedance of PEDOT probes when compared to PtIr. Optical microscopy revealed that all PEDOT coatings were fully intact and adherent to the in vitro probes after 24 h of stimulation.

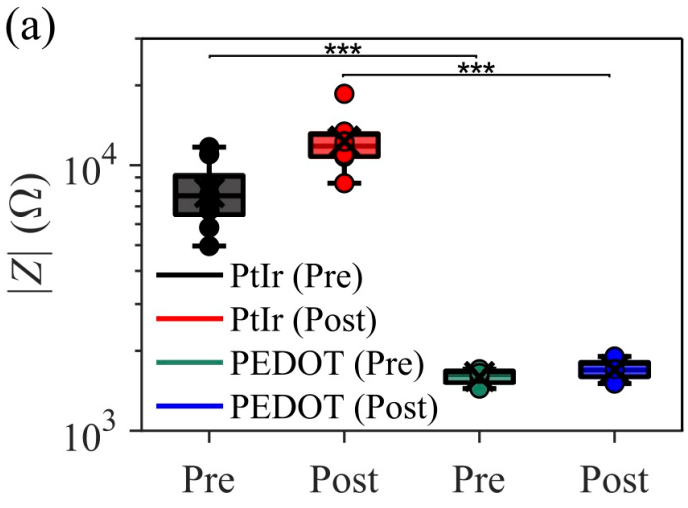

Figure 3.1 Electrochemical measurements measured in vitro from PEDOT and PtIr probes before (Pre) and after (Post) 24 h of stimulation. (a) Median, mean, and interquartile range of Z measured at 1 kHz. PEDOT: n=4, PtIr: n=8, p-values are calculated using an independent two-tailed t-test, in box plots: x = mean, o = raw data points, ***p≤0.001.

3.5 In vivo electrochemical stability

PEDOT-coated PtIr microelectrodes have lower impedance than uncoated PtIr when measured in PBS in vitro (Figure A.1, Appendix A). The electrical properties of penetrating neural probes change when implanted in tissue, and the electrical stability may be impacted by the foreign body response over time. To investigate the impact of the acute and chronic phases of the foreign body response on PEDOT coated neural probe performance, probes were implanted for a duration consistent with the acute (2 weeks) and chronic (2 months) inflammation phase. The electrochemical performance of PEDOT and PtIr probes are shown in Figure 3.2. The impedance magnitude (Figure 3.2a) of PEDOT probes after 2 weeks was significantly lower than PtIr at

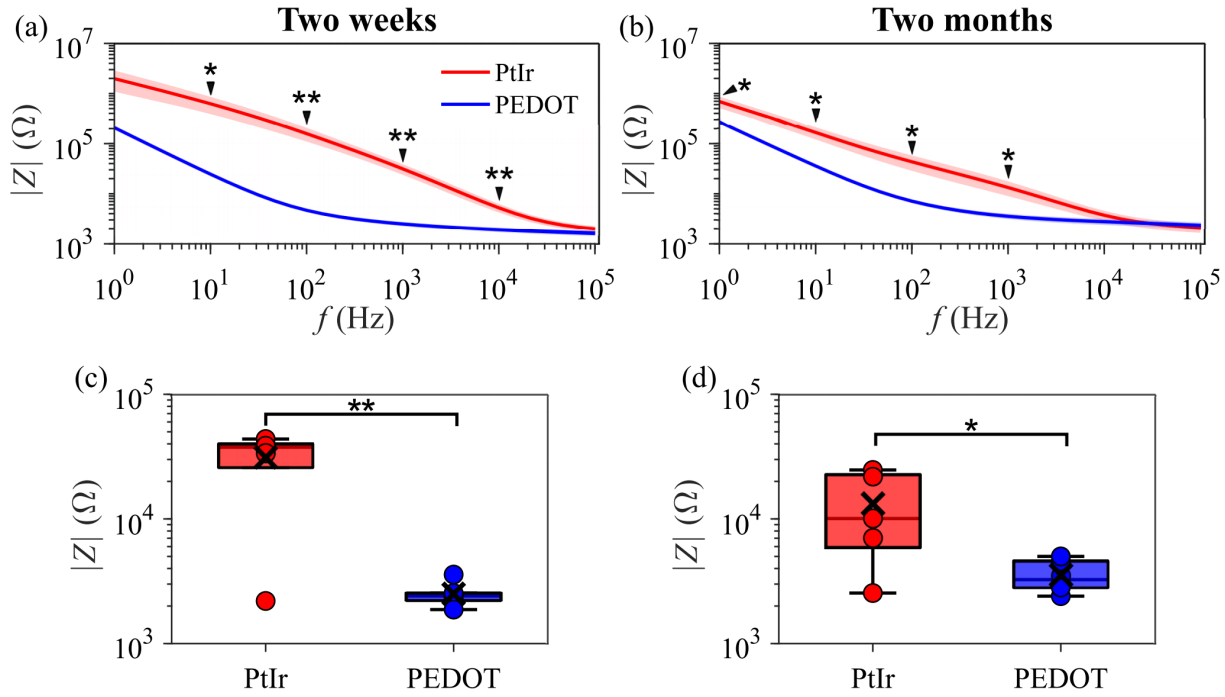

Figure 3.2 Electrochemical measurements of probes implanted in vivo for 2 weeks (left), and 2 months (right) measured following explantation. (a, b) Mean ± standard error of the mean (SEM) impedance magnitude ($|Z|$) vs. frequency (f) for PtIr (red) and PEDOT (blue) electrodes. (c, d) Median, mean, and interquartile range of Z measured at 1 kHz for PtIr and PEDOT probes. Shaded area represents SEM, 2 weeks: n=6, 2 months: n=6, p-values are calculated using an independent two-tailed t-test, in box plots: x = mean, o = raw data points, *p≤0.05, **p≤0.01.

frequencies ranging from 10 Hz to 10 kHz. After 2 months of implantation, the impedance magnitude (Figure 3.2b) of PEDOT probes was significantly less than the impedance magnitude of PtIr at frequencies ranging from 1 Hz to 1 kHz. Figure 3.2c,d shows the impedance at 1 kHz of

PtIr and PEDOT probes measured after 2 weeks and 2 months, respectively. The mean difference in impedance at 1 kHz of PtIr and PEDOT probes after 2 weeks implantation was 28.7 kΩ. For electrodes implanted for 2 months, the mean difference in impedance at 1 kHz was 9.7 kΩ. The impedance magnitude of PEDOT probes increased after 2 months of implantation above the impedance measured at 2 weeks. The increase in impedance is likely due to the presence of insulating scar tissue that is formed in the chronic phase but is not present in the acute phase. The impedance of PtIr decreased after 2 months of implantation when compared to the impedance measured after 2 weeks, which has been observed in previous studies [91]. Previously, the suggestion was that the impedance decrease was caused by the formation of a conductive IrOx layer that forms on the surface of the PtIr electrode, that may act to lower the impedance. Notably, the impedance values measured from PEDOT probes show less dispersion than PtIr, seen in the individual raw data of Figure 3.2c,d. The impedance is consistent and near the mean for individual PEDOT probes, while the impedance of PtIr varies widely from the mean impedance. This may be due to the variation in reactivity of PtIr surfaces in aqueous environments, or leakage underneath the insulation at the electrode tip, which may be minimized when PEDOT coatings are present.

3.6 Immunohistochemical analysis

The immune response following the initial impact of insertion starts a cascade of complex processes that function to heal the wound and break down foreign material [58]. Following injury, cells called microglia are activated and appear around the implant site within 1 day and start to produce enzymes to degrade foreign materials. If the body fails to degrade the implant or the implant is not removed, a chronic foreign body response occurs. This reaction is characterized by the presence of reactive astrocytes which form a glial scar to encapsulate and separate the object from healthy tissues. Astrocytes are characterized by filaments of polymerized glial fibrillary acid protein (GFAP). Microglia are characterized by the expression of the ionized calcium binding adaptor molecule 1 (Iba1), a calcium-binding protein.

The PEDOT:BF_4 coatings on PtIr electrodes have a porous morphology [185] and studies have demonstrated that porous PEDOT materials increase neuronal cell growth and attachment, and do not exhibit cytotoxicity in vitro [200]. Additionally, the recorded amplitude of extracellular single-unit action potentials from single neurons varies inversely with the distance between the neuron and the recording electrode [201]. Therefore, neurons able to attach to the electrode sites increase

the amplitude and signal-to-noise ratio of recorded electrical signal [14, 202]. Thus, it is important to understand if PEDOT decreases or, especially, increases the inflammatory response when implanted in vivo.

Here, the inflammatory tissue response to implanted PtIr microelectrodes coated with PEDOT over 2 weeks and 2 months of implantation was quantified to assess the acute and chronic immune response. To evaluate the degree of the foreign body reaction toward the implanted probes, the brain was sliced in the horizontal plane and immunohistochemically stained. Staining was performed for Iba1 and GFAP which provides information about the microglia activity and chronic formation of scar tissue surrounding the probe, respectively. Figure 3.3 shows tissue sections containing the electrode sites. The top schematic of Figure 3.3 shows the coronal plane of a mouse brain with PEDOT and PtIr electrodes at the approximate placement in the thalamus. After 2 weeks of implantation, GFAP and Iba1 staining for PtIr (Figure 3.3a,d) and PEDOT (Figure 3.3b,e) shows an increase in intensity around the electrode sites. The mean normalized GFAP intensity profiles along concentric circles extending 300 μm from the probe surface were averaged over all slices per animal group (Figure 3.3c). The observed difference in mean GFAP intensity surrounding PtIr was not statistically significant from the GFAP intensity surrounding PEDOT after 2 weeks. Iba1 staining, representing microglia, after 2 weeks of implantation, showed a similar intensity profile between PtIr and PEDOT electrodes and the observed difference in intensity was not statistically significant (Figure 3.3f).

After 2 months implantation, the ongoing presence of the stiff implant in the tissue drives further inflammation. The GFAP and Iba1 staining for PtIr (Figure 3.3g,k) and PEDOT (Figure 3.3h,l) show increased intensity around the electrode sites. The observed difference in mean GFAP intensity surrounding PtIr and PEDOT sites was not statistically significant as can be seen from the fluorescent intensity profiles (Figure 3.3i). Additionally, the mean Iba1 intensity surrounding PtIr was not significantly different from PEDOT (Figure 3.3l). The presence of the underlying stiff PtIr electrode is expected to cause a prominent inflammatory response, and here we confirm that the PEDOT coating was not sufficient to offset those effects. Similar observations have been made in a study by Boehler et al. where CV sweeps were employed for releasing an anti-inflammatory drug, Dexamethasone (Dex), from PEDOT:Dex coated electrode sites [203]. The impact of the release of Dex on the immune response was evaluated over 12 weeks in vivo. They found that differences

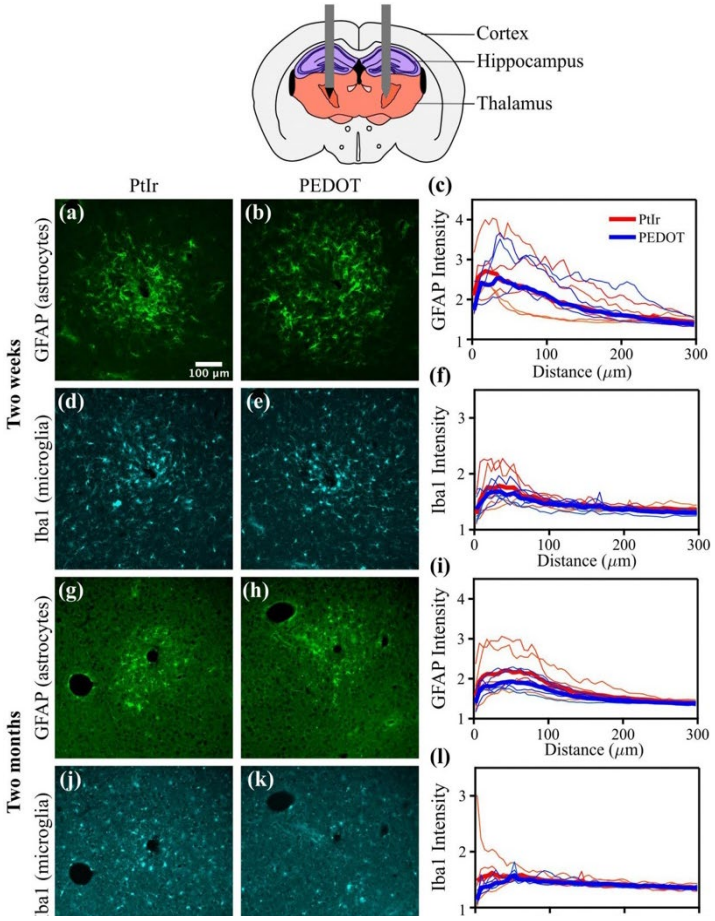

Figure 3.3 Acute (2 weeks) and chronic (2 months) histology images and analysis. (Top) Coronal section of a mouse brain showing electrode placement of PtIr (right hemisphere) and PEDOT (left hemisphere) electrodes. After 2 weeks implantation: GFAP (astrocyte) staining around a) PtIr and b) PEDOT implant location and c) mean normalized GFAP intensity vs. distance from PtIr (red) and PEDOT (blue) track. Iba1 (microglia) staining around (d) PtIr and (e) PEDOT implant location and f) mean normalized Iba1 intensity vs. distance from track. After 2 months implantation: GFAP staining around g) PtIr and h) PEDOT implant location and i) mean normalized GFAP intensity vs. distance from track. Iba1 staining around j) PtIr and k) PEDOT implant location and l) mean normalized Iba1 intensity vs. distance from track. Thick lines indicate the mean intensity calculated from intensity data acquired from each mouse (thin lines), 2 weeks: n=6, 2 months: n=7.

in GFAP and ED1 (representing activated microglia) intensity of PEDOT:Dex coated probes and IrOx probes were not statistically significant.

3.7 In vivo electrochemical stability with stimulation

To understand the impact of stimulation on the long-term electrical stability in vivo, we monitored the electrochemical impedance of PEDOT and PtIr probes over a period of 2 months. The protocol

for stimulation and recording is shown in Figure 3.4. Electrochemical impedance spectroscopy (EIS) was performed immediately before surgery (ex vivo), and following surgery (in vivo), and performed daily until the end of the experiment. The stimulation protocol began 7 days following surgery to allow for recovery. Stimulation with biphasic current pulses (20 μA and 18.4 μC

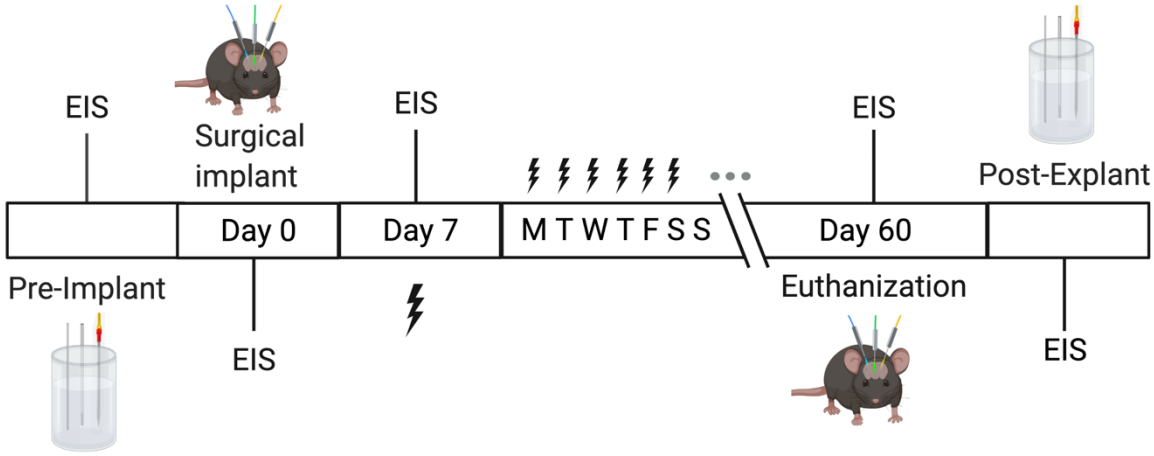

Figure 3.4 Timeline for EIS measurements and stimulation of neural probes during 2 months implantation in vivo. Prior to surgical implant and following explantation of probes, EIS was recorded with a three-electrode cell (illustrated). The stimulation protocol (indicated by the lightning symbol) began 7 days after implantation. Stimulation was delivered and EIS was measured for 5-6 days per week for a period of 60 days. After explantation, EIS was measured in a three-electrode cell. MTWTFSS refers to the days of the week, i.e., Monday, Tuesday, etc. Created with BioRender.com.

cm^{-2} per phase at a frequency of 100 Hz) was delivered for 30 min a day for 5–6 days per week until the end of the experiment. At the end of the experiment, following explantation and rinsing with PBS, the EIS measurements were immediately measured. The mean impedance magnitude at 1 kHz of PtIr and PEDOT probes, measured daily throughout 2 months implantation, is shown in Figure 3.5a. On day 1, the impedance of PEDOT was lower than PtIr. The impedance of both PEDOT and PtIr probes increased steadily from day 1 to day 6, likely due to the formation of an insulating layer of cells around the probe as a result of the acute inflammatory response [198]. Notably, the impedance of PEDOT and PtIr probes decreased on day 7 due to effects of the first stimulation. This decrease in impedance following stimulation has been observed in several other studies for electrodes containing Ir, in which a conductive, and porous activated IrO_2 layer formed on the surface following stimulation which acted to decrease the impedance [185, 187]. The

impedance of PEDOT remained lower than PtIr probes prior to day 40. Figure A.3, shows the individual impedance magnitude at 1 kHz, measured on day 40–60 for five PEDOT probes. Four of the five PEDOT probes maintained low impedance across the entire experiment, while one probe demonstrated a sudden impedance increase on day 40, likely due to PEDOT delamination. Figure 3.5b shows the impedance at 1 kHz of PtIr probes, four PEDOT probes, excluding the damaged probe, and all five PEDOT probes, including the damaged probe.

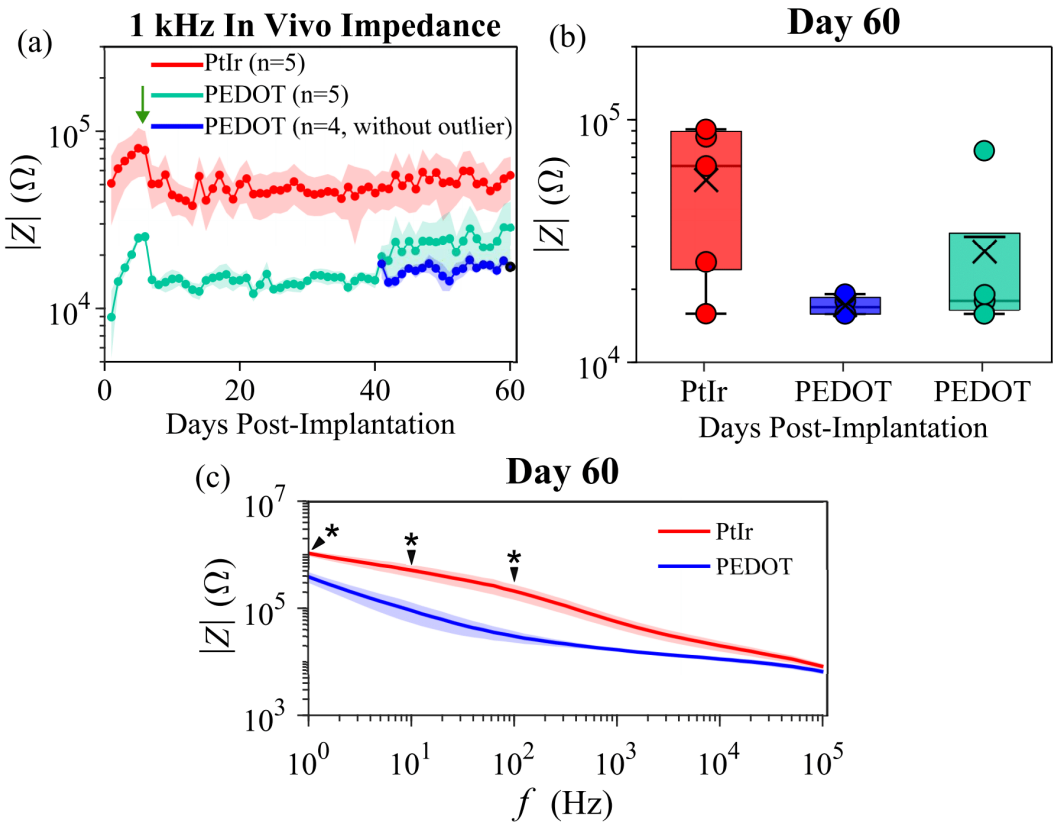

Figure 3.5 In vivo electrochemical measurements recorded daily following stimulation, over 2 months of implantation. a) Mean ± SEM impedance magnitude ($|Z|$) vs. number of days following implantation of PtIr (red) and PEDOT (blue) probes. PtIr: n=5, PEDOT: n=5, green arrow indicates beginning of daily stimulation. b) Median, mean, and interquartile range of $|Z|$ measured at 1 kHz recorded in vivo on day 60, the last day of implantation, for PtIr (red), PEDOT without outlier (blue), and PEDOT including outlier (green). In box plots: x = mean, o = raw data points, PtIr: n=5, PEDOT (blue): n=4, PEDOT (green): n=5. c) Day 60 mean ± SEM PtIr and PEDOT impedance magnitude ($|Z|$) vs. frequency (f) calculated without the data from the PEDOT outlier. Black arrows indicate the frequency that significance was measured. Shaded area represents the SEM, p-values are calculated using an independent two-tailed t-test, *p≤0.05.

When considering only probes with intact PEDOT coatings, the impedance of PEDOT probes at the end of the 60-day experiment was lower than the impedance of PtIr. This difference was however not found to be statistically significant for the impedance at 1 kHz ($p = 0.058$). The impedance magnitude of PEDOT probes at 1 to 100 Hz was lower than PtIr and statistically significant ($p < 0.05$). Notably, the impedance values of PEDOT probes do not vary widely from the mean impedance, while PtIr electrodes display a large variation from the mean impedance. The wide dispersion of impedance values for PtIr probes indicates that PEDOT coated PtIr probes are more electrochemically stable under stimulation than PtIr probes without a PEDOT coating. Figure 3.5c shows the impedance spectra on day 60. The mean difference in impedance between PtIr and PEDOT probes at 1 kHz is 39.3 kΩ.

An equivalent circuit model was used to quantify the factors influencing neural probe impedance. The circuit models were fit to measured impedance data to examine changes that occur after electrode implantation and stimulation. Modeling was performed on impedance data measured after probe implantation. This model was adapted from previously used models used to understand the electrode-tissue interface in microelectrode stimulation and recording applications with and without PEDOT coatings [204, 205].

The neural probe impedance was examined as a function of time after implantation by performing EIS measurements periodically after implantation. Figure 3.6a displays Nyquist impedance plots from a typical data set for a PtIr probe where substantial changes in the impedance spectra can be seen in the days following implantation. Conversely, the Nyquist impedance plots in Figure 3.6b from a PEDOT probe show relatively minor changes in the impedance spectra throughout the implantation period.

We compared the impedance data measured on the first day after implantation and day 10, 20, 40, and 60 after implantation using the model in the inset of Figure 3.6. The PtIr electrode was represented by a constant phase element (CPE) according to the following equation:

$$\mathrm{CPE} = \frac{1}{Q(j\omega)^{\alpha}} \tag{3.1}$$

where Q is the coefficient of the CPE capacitance (F $s^{\alpha-1}$), α is a phase factor defined for $0 < \alpha < 1$, $j = \sqrt{-1}$, and ω is the angular frequency (rad s^{-1}). The tissue layer impedance (R_s) and the

tissue/PEDOT impedance is represented by a resistance (R_s) in series with a parallel combination of a resistance (R_{CT}) and a CPE.

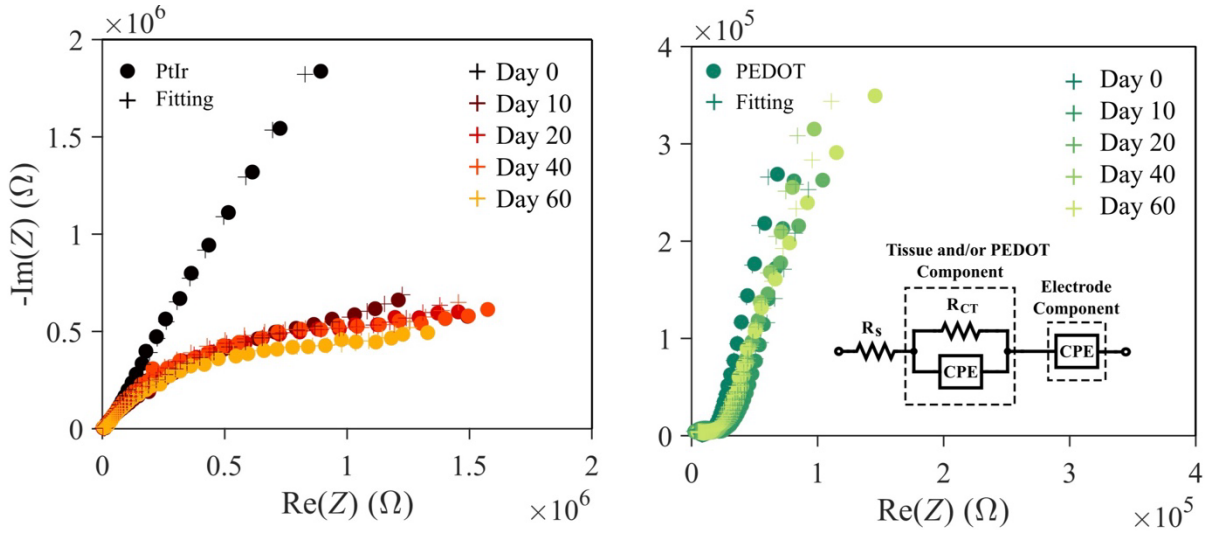

Figure 3.6 Representative Nyquist impedance plots (o) and data fitting (+) of (a) PtIr and (b) PEDOT neural probes after implantation at days 0, 10, 20, 40, and 60. Day 0 corresponds to the first day of implantation. The inset in (b) shows the equivalent circuit model used for PtIr and PEDOT probes.

The model analysis gave the parameters shown in Table 3.1. Day 0 corresponds to the first day of implantation without stimulation and Day 10 is after stimulation began. For both the uncoated and coated probes, after 10 days of implantation, and following stimulation, the CPE coefficient representing the PtIr electrode, Q_t, decreased, which corresponds to an increase in the magnitude of capacitive impedance. For both probe types, the CPE coefficient representing tissue encapsulation increased after 10 days of implantation, corresponding to a decrease in the magnitude of capacitive impedance. This trend is seen in Figure 3.6, where the impedance after the start of stimulation caused a decrease in total impedance of both PtIr and PEDOT probes. The parallel tissue resistance (represented by R_{CT} for PtIr) of the tissue encapsulation of PtIr probes increased more than three orders of magnitude after 10 days of implantation and remained high throughout the 60 days of implantation. While the charge transfer resistance (represented by R_{CT} for PEDOT coated probes) was relatively stable throughout the implantation period. The series tissue resistance (R_s) had a mid-range resistance value throughout the implantation

Table 3.1 Model parameters from EIS data acquired after electrode implantation.

Electrode	Day	R_s [Ω]	R_{CT} [Ω]	Q_t [F $s^{\alpha-1}$]	α_t	Q_e [F $s^{\alpha-1}$]	α_e	$X^2/\|Z\|$
PtIr	0	9.84E+03	6.35E+03	2.94E–08	0.73	7.74E–07	0.56	0.05
PtIr	10	6.77E+03	1.12E+06	5.30E–07	0.66	7.63E–08	0.66	0.15
PtIr	20	1.09E+04	1.00E+06	5.59E–07	0.53	4.26E–08	0.74	0.05
PtIr	40	1.20E+04	1.04E+06	5.24E–07	0.54	3.13E–08	0.77	0.07
PtIr	60	1.37E+04	1.05E+06	7.11E–07	0.58	4.86E–08	0.68	0.05
PEDOT	0	6.37E+03	2.75E+04	6.98E–07	0.92	7.25E–06	0.33	4.11E–03
PEDOT	10	9.81E+03	3.64E+04	8.05E–07	0.85	1.32E–06	0.30	7.40E–02
PEDOT	20	9.11E+03	4.25E+04	7.67E–07	0.88	5.04E–06	0.23	6.15E–02
PEDOT	40	7.83E+03	1.44E+04	6.68E–07	0.87	7.81E–07	0.50	3.79E–02
PEDOT	60	6.70E+03	1.91E+04	6.00E–07	0.84	1.37E–06	0.44	3.60E–02

3.8 Conclusions

Coatings of PEDOT:BF_4 were electrodeposited onto PtIr neural stimulation microelectrodes. These PEDOT and PtIr probes were implanted intracerebrally in mice for 2 weeks and 2 months to assess the impact of electrodes on the foreign body response. The PEDOT coating displayed significantly lower impedance compared to PtIr after 2 weeks and 2 months of implantation. Additionally, the inflammation intensity surrounding PEDOT coated electrode tips was assessed and compared to the intensity of inflammation surrounding PtIr. None of the conditions tested demonstrated a difference in inflammation intensity that was statistically significant. Finally, PEDOT and PtIr probes were implanted 60 days, during which they were subjected to daily stimulation and electrochemical measurements. In vivo measurements of the impedance over the implantation period were overall lower for PEDOT when compared to PtIr. While the impedance decreased by

the presence of PEDOT, the bulk stiffness of the underlying PtIr remains high, resulting in a similar degree of inflammation between the two probe types. In the future, we aim to fabricate ultra-thin neural electrodes based on PEDOT implanted with a stiff shuttle that would degrade quickly upon implantation, to improve the foreign body reaction.

This in vivo study is the first to report on the electrochemical performance of electrodeposited PEDOT:BF_4-coated PtIr neural stimulating probes when subjected to long-term exposure to biological environments and stimulation. It suggests that the ionic conduction provided by the PEDOT coatings can improve neural stimulating probes by reducing the impedance during an implantation period of 60 days. In addition, the foreign body response to either electrode was assessed and found to be the same, indicating that PEDOT probes have similar levels of insulating scar tissue at the surface as PtIr. These results indicate that PEDOT:BF_4 coatings decrease the impedance of PtIr probes for up to 40 days when subjected to in vivo conditions and daily stimulation, however, the coatings would benefit from increased adhesion which may be achieved by modifying the PtIr surface to be more porous. Electrodeposited PEDOT:BF_4 is an excellent candidate for decreasing impedance of metallic neural probes for chronic in vivo stimulation applications.

3.9 Experimental section

Materials: 3,4-ethylenedioxythiophene (EDOT) and acetonitrile (anhydrous, 99.8%) were purchased from Millipore-Sigma. Tetraethylammonium tetrafluoroborate ($TEABF_4$, 99%) was purchased from Acros Organics. All the chemicals were of analytical grade. Platinum iridium (PtIr, 80:20 alloy) neural electrodes, with a 231 μm shank diameter, were purchased from MicroProbes for Life Science (Gaithersburg, MD). The PtIr electrodes were supplied with an insulating coating of Parylene-C along their length and had an exposed conical tip with an average base diameter of 40 μm and an average length of 152 μm, for an average total exposed surface area of 10,889 μm^2. However, the exposed surface area on different electrodes ranged from 6,000–11,000 μm^2. Before electrodeposition and characterization, PtIr electrodes were cleaned by rinsing in an acetone, isopropyl alcohol, and deionized water, then dried with a stream of N_2. The PtIr electrodes were examined as received from the manufacturer prior to experiments to determine if there was parylene C delamination by examining electrodes using a microscope. If delamination was observed, the electrodes were excluded from the experiment.

Electropolymerization of PEDOT:BF_4: Electrochemical polymerization of PEDOT:BF_4 onto untreated PtIr electrodes was performed galvanostatically, using a three-electrode setup, consisting of a PtIr working electrode, a Pt coil counter electrode (BioLogic, France) and an Ag/AgCl reference electrode (ALS RE-1B, Japan) in an electrolyte solution containing 10 mL of acetonitrile, 0.02 M EDOT, and 0.12 M $TEABF_4$. The deposition was carried out for 50 s at 315 nA, with a final polymerization charge density of ≈0.2 C cm^{-2}.

Electrochemical Characterization: EIS was performed in a three-electrode cell with a potentiostat (VSP-300, BioLogic, France) equipped with an EC-lab software in PBS at room temperature (≈22 °C). Impedance measurements in vivo were performed in a two-electrode configuration using a stainless-steel screw as the reference/counter electrode (see Surgery section below). The screw was equidistant from the PtIr and PEDOT electrodes.

EIS was performed at frequencies ranging from 1 Hz to 100 kHz at 10 points per decade with an applied AC voltage of 10 mV_{rms} and a bias of 0 V versus Ag/AgCl reference electrode. Bode (impedance magnitude vs frequency) and phase angle plots were generated for each measurement.

Equivalent Circuit Analysis: An equivalent circuit model was used to quantify the factors influencing neural probe impedance. The circuit models were fit to measured impedance data to examine changes that occur after electrode implantation and stimulation. Modeling was performed on impedance data measured after probe implantation on days 0, 20, 40, and 60. Day 0 corresponds to the first day after implantation. This model was adapted from previously used models used to understand the electrode-tissue interface in microelectrode stimulation and recording applications [204, 205]. Parameter estimates were calculated using Z Fit, which is the EC-Lab impedance fitting tool.

In Vitro Stimulation: Probes were stimulated while submerged in PBS at ≈22 °C using a Model 4100 isolated high-power stimulator (A-M Systems, USA). Stimulation was delivered using charge-balanced, biphasic, cathodic-first current pulses at 100 μs per phase with a 10 μs interphase period, at 100 pulses per second (pps) and a current intensity of 20 μA per phase, a current density of 183.7 mA cm^{-2} per phase, delivering a charge of 2 nC per phase, and a charge density of 18.4 μC cm^{-2} per phase. These values fall in the non-damaging regime of the Shannon-plot, and were chosen to stay under the recommended safety limit of 30 μC cm^{-2} and below 4 nC per phase, values that were reported to avoid tissue damage while still eliciting a response in the neurons [206, 207].

Charge-balanced biphasic stimulus waveforms decreased the probability of electrode corrosion and tissue damage [208]. In addition, these parameters were found to not cause the onset of water reduction or oxidation from measuring voltage transients performed for the same probe and PEDOT coating [185]. The frequency of 100 Hz is clinically relevant since symptoms of Parkinson's are reported to be relieved over a large range of stimulation frequencies (50–6000 Hz) [206]. A Pt wire served as the ground electrode. Before and immediately following stimulation, EIS was recorded.

Surgical Procedures: All procedures involving animals were conducted in accordance with Canadian Council of Animal Care guidelines and approved by the CHU Sainte-Justine Research Center Animal Ethics Board (CIBPAR). Three sets of mice (2–4 months age) were used in three separate experiments with varying time points and conditions. Set 1 mice underwent 2 weeks of implantation. Set 2 mice underwent 2 months of implantation. Set 3 mice underwent 2 months implantation with stimulation and daily impedance measurements. The time point and number of subjects in each experiment are: (1) 2 weeks implantation of six uncoated and six PEDOT-coated PtIr neural stimulation electrodes tested on six C57BL/6J mice (Jackson Laboratory stock no. 000664, n = 6, 3 males, 3 females), (2) 2 months implantation of seven uncoated and seven PEDOT-coated PtIr neural stimulation electrodes tested on seven C57BL/6J mice (Jackson Laboratory stock no. 000664, n = 7, 4 males, 3 females), and (3) 2 months implantation and daily stimulation of five uncoated and five PEDOT-coated PtIr neural stimulation electrodes tested on five C57BL/6J mice (Jackson Laboratory stock no. 000664, n = 5, 4 males, 1 female). The animals were maintained under controlled environmental conditions (23 °C, 12 h light/dark cycle) with food and water provided ad libitum. They were initially anesthetized with 5% isoflurane in O_2 and surgeries were performed under anesthesia with 2% isoflurane. For surgery, the head of the mouse was immobilized in a stereotaxic apparatus. The body temperature was kept constant at 37.5 °C with a heating pad. Each mouse was implanted bilaterally with one coated and one uncoated PtIr electrode. A miniature stainless-steel screw, attached with wire to an Au pin connector, was driven into the skull above the cerebellum and served as ground/reference electrode, along with a stainless-steel anchor screw located toward the posterior of the brain. After locating Bregma, holes were drilled into the skull and electrodes were implanted at final coordinates: (experiment (1) and (2)) −1.94 mm anterior/posterior, +/−1.08 mm medial/lateral, and −2.96 mm dorso/ventral, relative to Bregma, and (experiment (3)) −1.70 mm anterior/posterior, +/−1.00 mm medial/lateral, and

−3.00 mm dorso/ventral, relative to Bregma. Electrodes were placed in holders attached to the stereotaxic arm and positioned over the holes in the skull. A hole was made in dura just below the tip of the electrode and then the electrode was lowered to the surface of the cortex. The electrodes were lowered using a micropositioner to the final depth. The external part of the electrodes was fixed to the skull using dental cement (Paterson Dental). Au pins, connected to the electrodes, were exposed on the surface of the implant. Impedance measurements were collected within 1 h following surgery. In experiment (3), animals were allowed to recover for one week following surgery before stimulation protocols began. In experiment (1) and (2), after electrodes were implanted, the animals were left undisturbed for the duration of the experiment. A schematic of the electrode placement is shown at the top of Figure 3.3.

In Vivo Stimulation and Measurements: The animals were stimulated for 30 min per day for 5 to 6 days a week using the same stimulator and stimulation parameters described in the "In vitro Stimulation" section. A miniature stainless-steel screw in the skull served as the ground electrode. After stimulation, EIS was recorded in vivo following the protocol described previously. The timeline of experiment (3) in this study is illustrated in Figure 3.4 and the relevant experimental parameters are reported in

Histology: Following termination of experiments, animals were deeply anesthetized with a ketamine/xylazine/acepromazine cocktail (80/12.5/2.5 mg kg^{-1}) via an intraperitoneal injection. Animals were transcardially perfused with 45 mL of 4% w/v paraformaldehyde (PFA) in 1× phosphate buffered saline (PBS). Extracted brains were then soaked in 4% w/v PFA for 2 weeks to preserve electrode tracks. Once fixed, the tissue was cryoprotected by a 24 h long soak in 15% w/v sucrose in 1× PBS. Next, tissue was embedded in optimal cutting temperature (OCT) compound and frozen to −20 °C in methyl butane. The frozen sample was sectioned into 25 μm slices using a cryostat (Thermo CryoStar NX50) and placed into individual wells containing 1× PBS and 0.02% w/v azide. To ensure that the interface evaluated corresponded to the conductive tip of the implanted electrode, sections were serially collected before the tip location and after the implant site was no longer visualized by eye and confirmed after staining via fluorescent microscopy. Approximately three tissue sections per electrode, corresponding to the location of the conductive tip of the implanted electrode, were considered for analysis. All collected sections were immunostained for each marker

Table 3.2 Summary of animal groups and stimulation parameters

Electrode ID	Implant duration [days]	Hours stimulated	Days stimulated
PtIr01	60	23.5	47
PtIr02	60	23	46
PtIr03	60	23.5	47
PtIr04	60	24	47
PtIr05	60	24	48
PEDOT01	60	24	48
PEDOT02	60	23	46
PEDOT03	60	23.5	47
PEDOT04	60	23.5	47
PEDOT05	60	24	48

Immunohistochemistry: All tissue sections were stained at the same time to minimize sample to sample variability. Free-floating sections were first incubated in 0.45% w/v gelatin and 0.25% w/v Triton X-100 in 1× PBS (PGT) for 3 × 15 min under gentle agitation to permeabilize tissue and block non-specific tissue binding. Two polyclonal primary antibodies were used for the visualization of different cell types; guinea pig anti-GFAP (1:2000 dilution) (173-004 Synaptic Systems, Germany) for the labeling of astrocytes, and rabbit anti-Iba1 (1:3000 dilution) (019-19741, Wako, Japan) for visualizing microglia. The sections were incubated with primary antibodies diluted in PGT overnight at 4 °C. After incubation, the sections were triple rinsed under gentle agitation, for 15 min each, in a solution of PGT. Slices were then incubated in a solution of PGT and the secondary antibodies Alexa 555 Goat anti-Guinea Pig IgG (1:2000 dilution) (A-21435, Thermo Fisher Scientific), and Alexa 647 Donkey anti-Rabbit IgG (1:2000 dilution) (A-31573, Thermo Fisher Scientific) at 21 °C (room temperature) for 1 h 30 min. Following incubation, sections underwent three washes in 1× PBS for 5 min each. Finally, slices were mounted in 4,6-diamidino-2-phenylindole (DAPI) Fluoromount-G (SouthernBiotech, USA) and stored in the dark at 4 °C.

Imaging Analysis: A DMi8 wide-field inverted fluorescence microscope (Leica, Germany) was used to image the stained brain slices. For each antibody, images were acquired using the same intensity and exposure time to reduce variability during data analysis. Pixel-based image intensity-based radial analysis was performed using an open source MATLAB file package, I.N.T.E.N.S.I.T.Y. v2.0 [209] used in the histology analysis of several peer-reviewed publications [190, 210-212].

For data analysis accomplished using these MATLAB scripts, images of the implant insertion site were compared to images of control data taken at ≈500 μm from the insertion sites. The control data was used to determine the background noise intensity threshold. This was calculated by initially removing all pixels considered "signal," that is, with an intensity above the mean pixel intensity reduced by one standard deviation. Then, the value of the background noise intensity threshold was calculated from the pixel intensity one standard deviation below the mean intensity of the remaining pixels. Bins with intensity values dimmer than average intensities of the control images were considered as holes in the tissue and were not included in the intensity analysis. For each image, the center and edges of the electrode track were identified manually using MATLAB. The script generated masks of 25 concentric rings every 10 μm from the edge of the track, for 300 μm. An example image with the concentric rings overlaid is shown in Figure A.2 (Appendix A). Electrode tracks were identified as holes in the tissue surrounded by an increased intensity fluorescence. The average gray scale intensity for all pixels above the background noise intensity threshold in each ring was calculated, normalized against the background, and plotted as a function of distance. For each animal group, the data was averaged across all images containing the electrode tip and reported as mean and standard error of the mean.

Statistical Analyses: All statistical analyses were performed with MATLAB functions or custom-made MATLAB scripts. To test the claim that PEDOT coatings have a mean impedance magnitude different than PtIr, an independent two-tailed t-test was performed. To compare measurements of PEDOT electrodes measured at different time points, a dependent t-test was performed.

On box plots, the line inside the box indicated the median, bottom, and top edges of the box indicated the 25th and 75th percentiles, respectively, and whiskers extended to 1.5 times the values of the 25th and 75th percentiles, and data that falls outside these values were considered outliers. Statistical significance was set at levels below $p = 0.05$.

CHAPTER 4 ARTICLE 2: FLEXIBLE AND STRETCHABLE PRINTED CONDUCTING POLYMER DEVICES FOR ELECTRODERMAL ACTIVITY MEASUREMENTS

4.1 Authors

Jo'Elen Hagler[1], ChiHyeong Kim[1], Pierre Kateb[1], Jeeyeon Yeu[1], Noémy Gagnon-Lafrenais[1], Erin Gee[2], Sofian Audry[3], and Fabio Cicoira[1]

[1] Department of Chemical Engineering, Polytechnique Montréal, Montréal, Canada

[2] Department of Music, Université de Montréal, Montréal, Canada

[3] Department of Media, Université du Québec, Montréal, Canada

Published February 18, 2022, *Flexible and Printed Electronics*

E-mail: fabio.cicoira@polymtl.ca

4.2 Abstract

Highly stretchable and flexible bioelectronics should form close contact with skin and tissues while being able to withstand the stresses and strains endured by the body in order to reliably monitor physiological signals over time. Here, we report highly stretchable poly 3,4-ethylenedioxythiophene: polystyrene sulfonate (PEDOT:PSS) films printed on thermoplastic polyurethane (TPU) substrates. We established the stability of the device conductivity under high strains up to 600%. The printed PEDOT:PSS film enabled the fabrication of printed organic electrochemical transistors with an ON/OFF ratio of ~450 on a flexible substrate. We also acquired physiological signals from measuring the skin conductance arising from changes in sweat volume by directly interfacing a printed PEDOT:PSS-based sensor on TPU with human skin. Stretchable printed PEDOT:PSS films on TPU provide a facile method of producing highly stable stretchable sensors for bioelectronic applications, enabled with simple and direct printing fabrication.

4.3 Introduction

The skin is the source of a wide range of physiological signals that are important indicators of a person's health. Skin-like sensors are used to track physical, electrical, and chemical physiological signals from the surface of human skin or within the body [213, 214]. Wearable and implantable devices are highly desirable for health monitoring [215], medical implants [216], and medical treatments [217, 218]. Wearable electronics should be stretchable to accommodate strains typically

experienced by the skin (~30%), and implantable devices need high flexibility to conform to curvilinear surfaces of tissues inside the body [219, 220]. In addition, to remaining functional under strain, the performance of stretchable electronics should remain stable, i.e. insensitive to strain, in order to obtain reliable recordings of physiological signals [221].

Progress in materials engineering and device fabrication have led to the development of stretchable electronics [222, 223]. Organic electrochemical transistors (OECTs) employing conducting polymers as channel materials have gained attention for their flexibility and stretchability, both required for wearable electronics [224]. The conducting polymer, poly 3,4-ethylenedioxythiophene (PEDOT) doped with polystyrene sulfonate (PSS), known as PEDOT:PSS, has contributed significantly to the rapid progress of flexible and stretchable electronics [175, 176, 225]. Stretchable PEDOT:PSS films are used as electrodes in bioelectronic devices, to record both electrical and chemical physiological signals [214]. PEDOT:PSS based sensors have been used to record electrical signals from the human body, such as action potentials generated in the muscles, with electromyography [168], the polarization and depolarization of cardiac muscle cells, with electrocardiography [226], and biopotential waveforms generated by the brain, with electroencephalography [227]. As chemical sensors, PEDOT:PSS films have been studied to analyze sweat for biomarkers such as glucose, peptides, and various ions [228].

Several techniques are currently available to attain highly stretchable electronic devices with conductances insensitive to strain. One approach includes creating composites by blending conducting polymers with other polymers such as polyurethane, PEG, or polydimethylsiloxane (PDMS), which lead to a decrease of the Young's modulus of the material, and an increase in stretchability [229-231]. Though such composites show high stretchability, their conductivity can be limited by the insulating nature of the additives. Further, the conductivity of the composite films is typically strain-sensitive [231]. Recently, in order to improve the stretchability of PEDOT:PSS, elastomers such as Zonyl and Triton X-100 have been used. Zonyl acts to enhance the wettability of PEDOT on several substrates and enables deposition on hydrophobic surfaces while also acting as a conductivity enhancer [232, 233]. Triton is a plasticizer that improves the stretchability of PEDOT [234, 235]. The stretchability of the conducting polymer film can also be increased by reducing the film thickness [231]. A highly reliable method to increase insensitivity of the film conductance to strain is through pre-stretching the substrate [236]. After releasing a prestretched substrate, buckling (wave-like structures) occurs out- of-plane, which improves stretchability. The

out-of-plane structures of prestretched substrates may be disadvantageous for bioelectronic devices requiring even and regular active surfaces to form intimate contact between the device and skin. Another approach to increase stretchability uses rigid materials at the sensor location connected by stretchable interconnects [221]. Still, mechanically stable interfaces between rigid and stretchable components are challenging to realize.

In this work we produced conductive films through printing methods, using a PEDOT:PSS screen printing ink on a polyurethane (TPU) substrate. The films were reversibly stretchable, i.e. the resistance after stretching did not signifigantly change upon release, without requiring pre-stretching, modification of the substrate or additives to the commercial formulation. The films showed about 3 times increase in resistance when stretched up to 100%. They also showed moderate stability under electrical cycling and high performance when employed as channel materials in printed OECTs. To demonstrate the potential use of the PEDOT:PSS films in wearable electronics, PEDOT:PSS was used as the sensor in a printed electrodermal activity (EDA) sensor that measures electrical changes of the skin, possibly related to the body's response to stress and other emotional stimuli. Currently, EDA is measured in commercial bioelectronic devices that monitor physiological signals and track important health metrics. Here, we indicate that this materials system and fabrication method can produce moderately stretchable electrodes, using simple and direct printing techniques, that are able to detect physiological signals such as EDA, advancing current bioelectronic device designs.

4.4 Experimental methods

Materials: The PEDOT:PSS screen printing paste (Clevios SV3 STAB), which contains a significant amount of glycols, was purchased from Heraeus. The company reports a sheet resistance of 700 Ohm sq^{-1}. The ink was homogenized in a planetary mixer (ARM-310, THINKY Co.) for 3 min at 2000 rpm and filtered (CHROMSPEC UV Syringe Filters, 25 mm diameter, 5.0 µm pore size), before printing. The silver (Ag) ink used for contacts (Ag paste 520 EI) was donated by Chimet S.p.A (Italy). Polyethylene terephthalate (PET) and thermoplastic polyurethane (TPU) on removable silicon paper (Elecrom Stretch White, thickness of 80 µm) were purchased from Policrom Screens (Italy). The PET was cleaned with isopropyl alcohol (IPA) and deionized water (DIW); TPU was cleaned with only DIW to avoid damaging the surface material, immediately before printing. A silicone elastomer kit (SYLGARD® 184), used to prepare PDMS, was

purchased from Dow Corning. Gallium Indium eutectic (EGaIn) was purchased from Millipore Sigma. Phosphate buffered saline solution (PBS, 0.0027 M potassium chloride and 0.137 M sodium chloride, pH 7.4, at 25 °C) tablets were purchased from Millipore Sigma and prepared by dissolving in DIW. Cylindrical wells (PYREX® cloning cylinder, Corning®) with an outer diameter of 10 mm, for containing the gating medium used in the OECT, were purchased from VWR (Canada). To prepare the activated carbon gate for OECTs, the carbon paper (Spectracarb 2050 A) was purchased from Fuel Cell Store (USA), the activated carbon (Norit), Nafion and IPA were purchased from Millipore Sigma. Kapton® polyimide tape was purchased from Digi-Key Canada.

Fabrication and electromechanical characterization of PEDOT:PSS films: The PEDOT:PSS solution was screen printed onto the flat surface of a stretchable TPU substrate, and heated on a hot plate (Corning®) in ambient air at 100 °C for 60 min. The samples were then allowed to cool for at least 30 min at room temperature. A cutting die consisting of two razors mounted parallel (3 mm spacing) to each other on a metal mount was used to cut the samples into rectangles (3 mm wide and ~45 mm long). After cutting, the silicon support substrate was removed from the back of the TPU leaving the PEDOT:PSS on the TPU device. This device configuration was used in all mechanical tests. The thickness of all PEDOT:PSS films was measured with a Dektak 150 profilometer. Film conductivity was measured with a 4-point probe (Jandel) and a Keysight B2902A source/measurement unit.

Optical micrographs were taken with a Carl Zeiss AX10 microscope at 50× magnification. To take images of films stretched to 10%, 30%, 100%, or 600%, both ends of the film were attached to an adhesive tape and fixed to a glass slide at the desired strain (Figure B.1, Appendix B). Optical images were taken in the stretched state.

Impedance measurements were conducted on the film during tensile testing, stretched at a rate of 10% s^{-1} using a mechanical tester (model Mach-1 v500csst, Biomomentum Inc., Canada) (Figure B.2, Appendix B). The PEDOT:PSS side of the film was placed in direct contact with the sensing Ag/AgCl electrodes (D = 2 mm) located on both sides of tensile grips (model MA068, Biomomentum) and connected to a Source/Measure Unit (Keysight SMU B202A) under an applied current of 10 μA (Figure B.3, Appendix B). The film resistivity was found using a first-order approximation, assuming the film is an ideal conductor, and calculated using the measured resistance and the device length during stretching.

OECT fabrication and characterization: The PEDOT:PSS OECTs were fabricated by a printed circuit board printer (Voltera V-One PCB printer). Source and drain electrodes were printed with Ag ink on a PET substrate and baked at 130 °C for 15 min on a hotplate (Corning®). Subsequently, PEDOT:PSS ink was printed in between the source and drain electrodes to serve as the channel material (channel dimensions: W = ∼1 mm, L = ∼1.5 mm, H = ∼1 μm) and baked at 120 °C for 30 min on a hot plate (Corning®). Then, PDMS (silicone elastomer with curing agent at a ratio of 10:1, mixed in the compounds mixer for 3 min at 2000 rpm) was printed in the uncured state over the Ag electrodes, placed on the hot plate and cured at 120 °C for 30 min. The PDMS layer served as a hydrophobic barrier between the Ag ink and the gating medium aqueous solution used in the OECT.

The gating medium (PBS) of the OECT was confined to an area over the channel with a plastic cylindrical well. Activated carbon on carbon paper was used as the gate electrode. To prepare the gate electrode, carbon ink containing 28 mg ml^{-1} of activated carbon and 1.4 mg ml^{-1} Nafion was dissolved in IPA, then the carbon ink was drop-cast on carbon paper and heated at 60 °C for 5 h to remove traces of IPA. The OECT output and transfer measurements were performed with a PXIe-4141 source/measurement unit controlled using LabVIEW software in ambient conditions. The microscope images of the channel, source and drain electrodes, and PDMS (Figure 4.7(a)) were taken with a Carl Zeiss Primovert Inverted Microscope.

Electrochemical characterization: Cyclic voltammetry (CV) and electrochemical impedance spectroscopy (EIS) of pristine PEDOT:PSS electrodes were performed with a Bio-Logic SP-300 Potentiostat. The CV and EIS tests used an Ag/AgCl reference electrode and a Pt counter electrode and were performed in a 20 ml glass vial filled with 10 ml of PBS, which served as the electrolyte. The scan rate for CV was 100 mV s^{-1} and the applied voltage was from −0.6 V to 0.8 V. The EIS was performed by applying a 10 mV sine wave potential around 0 V at frequencies ranging from 100 kHz to 1 Hz.

Fabrication and characterization of PEDOT:PSS EDA sensors: The EDA sensors were fabricated by first printing the Ag ink on the surface of TPU with a PCB printer (Voltera) and baking at 100 °C for 30 min. Using the same PCB printer, a 5 mm × 5 mm square of PEDOT:PSS ink was printed in contact with the Ag, with PEDOT:PSS overlapping with the Ag electrodes ∼1 mm, and baked at 100 °C for 60 min. The resulting PEDOT:PSS film had a thickness of ∼30 μm. The silver

interconnect was then insulated using Kapton® tape to avoid contact between the skin and Ag during acquisitions (Figure 4.9(b)).

Electrodermal activity measurements: The protocol for human experiments was approved by the ethical committee of Polytechnique Montreal (approval number CER-2021-04-D).

To perform EDA measurements, PEDOT:PSS (or reference stainless steel) sensors were placed on the tips of the middle and pointer fingers of a volunteer. To acquire signal from the skin/sensor interface, a cable was attached via an alligator clip to the Ag interconnect in contact with the electrode. The sensors were fixed to the fingers with a small Velcro band. To acquire the measurement, the volunteer underwent a visual stimulation protocol designed to evoke EDA. The volunteer sat in an environment of around 21 °C (room temperature) to ensure their hands were not sweating. While recording EDA from the fingertips using the PEDOT:PSS or steel electrodes, the volunteer listened to audio through headphones and watched a video recording on a monitor. The video recording started with 2–3 min of viewing a meditative setting followed by a brief audiovisual stimulation, during which the EDA signal was acquired.

The EDA was acquired and buffered through a home-made operational amplifier with no additional filtering circuitry. The raw physiological signal is encoded at a sampling rate of 1000 Hz into a 10-bit ADC via a Teensy 3.2 development board with an ARM Cortex-M4 processor and written to an SD card. After acquisition, the data was low-pass filtered using a toolbox for EDA signal processing (BioSPPy).

4.5 Results and discussion

4.5.1 Evolution of PEDOT:PSS resistance with strain

To determine the lifetime and suitability of stretchable conducting films for wearable electronics, it is important to characterize their strain sensitivity and reversibility. The screen-printed PEDOT:PSS films on TPU had a thickness of ∼240 nm and an initial (unstretched) average conductivity (number of samples (n), n = 5) of 60 ± 15 S cm^{-1}. The adhesion of the PEDOT:PSS to TPU was determined using a tape test. No PEDOT:PSS was removed during the tape test (Figure B.4, Appendix B) indicating excellent adhesion to TPU. Next, we measured the resistance versus strain of a PEDOT:PSS film screen-printed on a TPU substrate. Figure 4.1(a) shows the evolution of normalized resistance, R/R_0, versus time, t (s), as a PEDOT:PSS film underwent ten cycles of

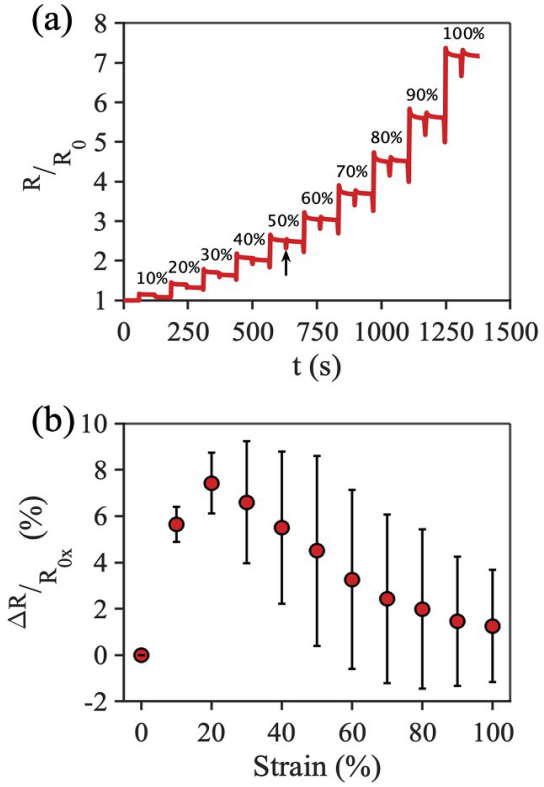

Figure 4.1 Evolution of stretchable PEDOT:PSS film resistance with applied strain. (a) Normalized resistance (R/R_0) vs time, t (s), for one film under incremental stretching from 0% to 100% strain. (The strain was applied for 60 s in the sequence of 0%, 10%, 0%, 20%, 0%, 30%,…,0%, 100%, 0%). R is the resistance measured in time and R_0 is the resistance at t = 0 s. Black arrow points to R/R_0 when the strain is released from 50% to 0%. (b) Average $\Delta R/R_{0X}$ vs strain, where R_{0X} is the resistance in the released state after the application of X% strain shown in (a), and ΔR is $(R - R_{0X})$ where R is the resistance in the stretched state. Error bars are standard deviation of $\Delta R/R_{0X}$ (n = 3).

loading of strain. The strain was applied for 60 s in the sequence of 0%, 10%, 0%, 20%, 0%, 30%,…,0%, 100%, 0%). R is the resistance measured in time, and R_0 is the resistance at t = 0 s. Under 10% strain, the normalized resistance increased by <20%, while under ~700% strain, the resistance increased by 100%, with respect to the initial value. A similar behavior was demonstrated for three additional PEDOT:PSS films (Figure B.5, Appendix B). Figure 4.1(b) shows the average $\Delta R/R_{0X}$ versus the strain applied to the films, where ΔR is $(R - R_{0X})$ with R indicating the resistance in the stretched state and R_{0X} the resistance in the released state after the application of X% strain shown in Figure 4.1(a). The error bars are derived from the standard deviation of the average $\Delta R/R_{0X}$ (n = 3). This ratio is an important benchmark of resistance variation and reversibility after undergoing strain. The resistance in the stretched state (under X% strain, X = 0 to 100) changes by <10% after the film is released (from X% to 0% strain) indicating small conductivity variation between the stretched and released states. That is, the conductivity of the film is rather insensitive to external strains after applying a preset strain. For instance, after applying a preset strain of 100%, applying additional strains within 100% causes a resistance variation of <10%. The stable value of the resistance upon release indicates the device is capable of meeting the strain requirements for stretchable wearable electronics, which require a stable resistance for precise recordings of physiological signals.

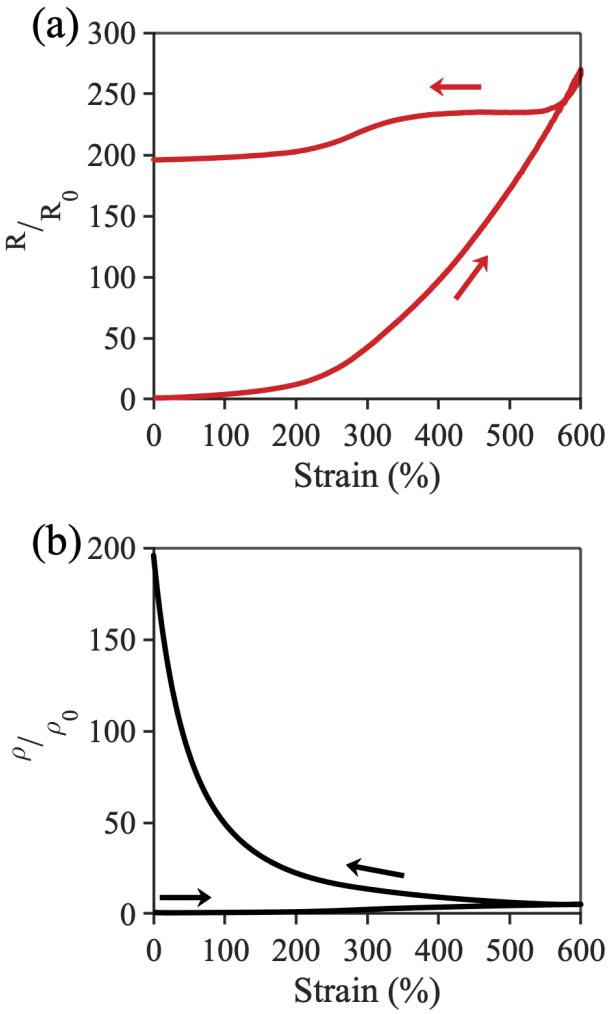

Figure 4.2 (a) Normalized resistance (red) and (b) normalized resistivity vs. strain (%) of a PEDOT:PSS film on TPU when stretched from 0% to 600% to 0% strain.

After observing that the films were able to withstand 100% strain, we measured their resistance (Figure 4.2(a)) and resistivity versus strain (Figure 4.2(b)) when stretched from 0% to 600% and back to 0% strain. The resistance after stretching from 0% to 100% strain was ~3 times larger than the initial value. Upon stretching from 100% to 600%, the resistance was ~250 times larger than the initial one. After releasing to 0% strain, the normalized resistance was ~200 times greater than the initial one. The resistivity versus strain of an ideal conductor is constant as the length is increased. The resistivity shown in Figure 4.2(b) demonstrates that the resistivity is relatively constant while stretching from 0% to 600% strain, then increases to 200 times the initial value as the film was released from 600% to 0%. The increase in resistivity is due to the film length decreasing to its initial length while the resistance decreased only slightly lower than the fully stretched state, causing a higher resistance per unit area than initially observed. The resistance after stretching remained higher than the initial value, due to irreversible cracking of the PEDOT:PSS film after a certain strain. The final conductivity of the film was ~0.3 S cm^{-1} after stretching to 600% strain and releasing. The data of three additional films undergoing the same experiment demonstrate similar behavior (Figure B.6, Appendix B). Optical images of the films under strains of 10%, 30%, 100%, and 600% (Figure 4.3) show that no visible cracking occurs at 10% or 30% strain, while cracks are visible at 100%. The cracks explain the observed increase in final resistance compared to initial resistance after stretching and releasing (Figure 4.2). However, even under

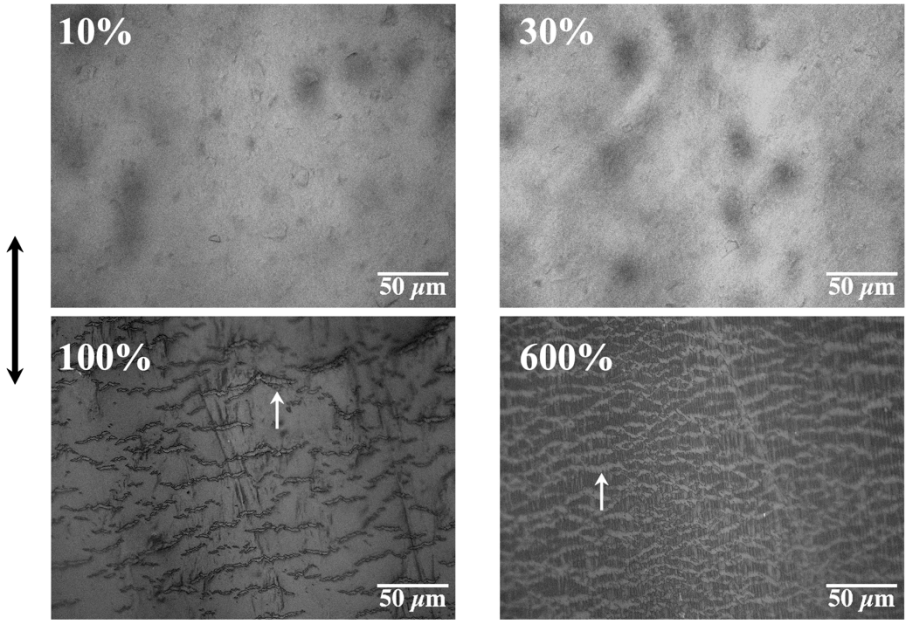

Figure 4.3 Optical images of PEDOT:PSS films on TPU in the stretched state at a strain of 10%, 30%, 100%, and 600%. Double arrow indicates direction of strain. White arrows point to cracks in PEDOT:PSS film.

600% strain, when the crack density is rather high, the films show a morphology of an interconnected network which may account for the moderate conductivity. The normalized resistance at 100% and 600% strain demonstrates the conductivity of the films is moderately stable under stretching when compared to stretchable conductive films currently available [237, 238], indicating that the PEDOT:PSS films on TPU are valid candidates for stretchable bioelectronics.

We subjected the films of PEDOT:PSS screen printed on TPU substrates to cyclic applications of strain. Figure 4.4(a) plots the representative normalized resistance, R/R_0, versus time, t (s), of 1000 cycles of strain applied to PEDOT:PSS films from 0% to 10%, 30%, or 100%. Figure 4.4(b) shows the first 200 s of Figure 4.4(a). The largest increase in resistance occurs in the first stretch, i.e. upon stretching to 10%, 30%, and 100%, the resistance, R, increased, respectively, by 20%, 50%, and 500%, with respect to the initial value, R_0, while after 1000 cycles, the increase, respectively, was of 30%, 60% and 650%. These results demonstrate that PEDOT:PSS films can withstand 1000 cycles of stretching with moderately stable resistance values, especially when stretched to 10% and 30% strain. The same experiment for three additional samples show similar behaviour (Figure B.7, Appendix B).

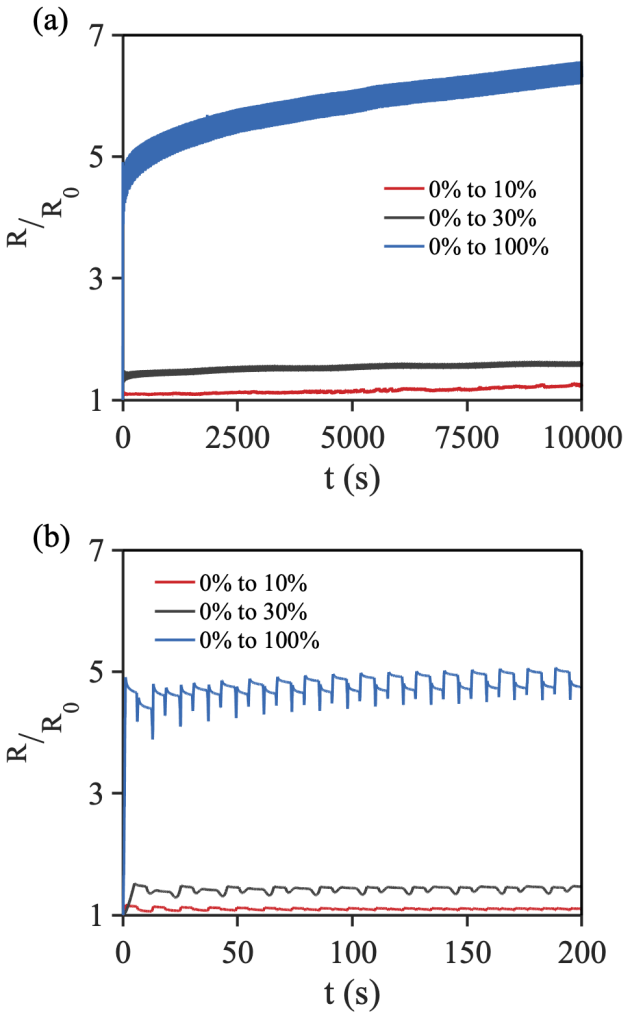

Figure 4.4 Evolution of resistance with cyclic loading of strain. (a) normalized resistance vs. time over 1000 cycles of 10%, 30%, and 100% strain and (b) the same samples as in (a) during the first 200 s.

Following these studies, to determine if the stability of the resistance would change with increasing thickness, we studied the average normalized resistance of PEDOT:PSS films with a thickness of 250 nm, 750 nm, or 1250 nm, when undergoing strains from 0% to 100% to 0% (Figure B.8, Appendix B). After undergoing 100% strain and returning to the unstretched state, the films with 250 nm and 750 nm thickness had a resistance that increased ~10× with respect to the initial value, while the resistance of the films with a thickness of 1250 nm increased to ~4× its initial value. When the PEDOT:PSS film was reduced to <1 µm, the stability of the resistance under strain decreased slightly. Based on these results, further work should consider using films with a thickness of at least 1 µm.

4.5.2 Evolution of PEDOT:PSS resistance with bending

The flexibility of the PEDOT:PSS film is an important parameter for wearable electronics, which requires devices to bend to the curvature of the recording surface. We measured the stability of the PEDOT:PSS resistance by measuring the resistance in the flat and bent state (Figure 4.5). Measurements under bending were achieved by fixing the PEDOT:PSS film on TPU on a semi-circular plate with a 20 mm radius. The resistance of PEDOT:PSS under bending was not significantly different than the resistance in the flat state, indicating the PEDOT:PSS film is stable under bending.

4.5.3 Characterization of flexible PEDOT:PSS OECTs

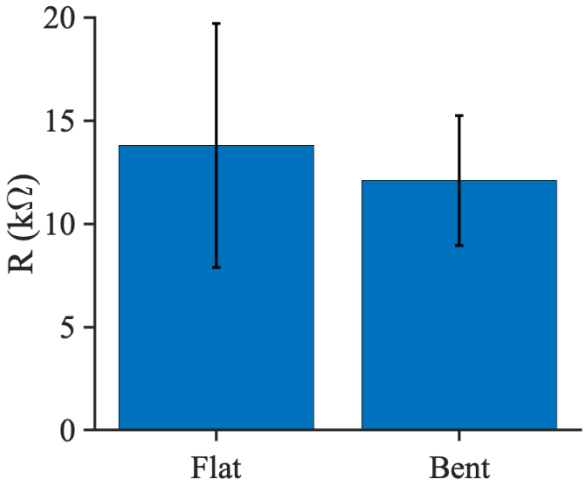

Figure 4.5 Average resistance and standard deviation of three PEDOT:PSS on TPU samples measured in the flat state and under bending to a 20 mm radius.

After observing these PEDOT:PSS films were electrically stable under mechanical testing, we demonstrated their ability to be used as the channel material in OECTs. To determine the optimal channel thickness, we measured the performance of OECTs with thicknesses of 600 nm, 1 µm, and 1.4 µm. From the transfer curves we extracted ON/OFF ratios of 843 ± 302, 1836 ± 266, and 1494 ± 210 for a channel thickness of 600 nm, 1 µm, and 1.4 µm, respectively (Figure 4.6). Based off these results, the OECTs in all subsequent studies were printed with a channel thickness of 1 µm.

The flexible printed PEDOT:PSS OECT for studying the OECT stability under bending is shown in Figure 4.7(a). The device characteristics were measured when the OECTs were flat and subjected to bending. To measure the characteristics of the printed OECT in a bent state, the substrate of the transistors was fixed on semi-circular plate, with a 30 mm radius (Figure B.9, Appendix B). The average transfer (figure 7(b)) and output (Figure 4.7(c)) curves of the OECTs (n = 3) show behaviour typical of PEDOT:PSS OECTs working in depletion mode. The individual OECT transfer curves in the flat and bent state are shown in Figure B.10 (Appendix B), and the individual OECT output curves in Figure B.11 (Appendix B). The flexible OECTs show no significant changes in transfer and output curves between a flat and bent state. The average ON/OFF ratio of the OECTs being 440 ± 10 in a flat state and 420 ± 20 while bent. In addition, the

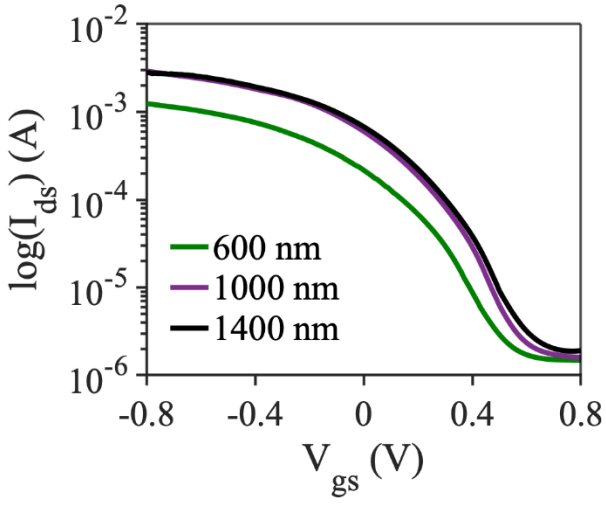

Figure 4.6 Average transfer curves of printed OECTs with PEDOT:PSS channel thickness of 600 nm, 1000 nm, and 1400 nm.

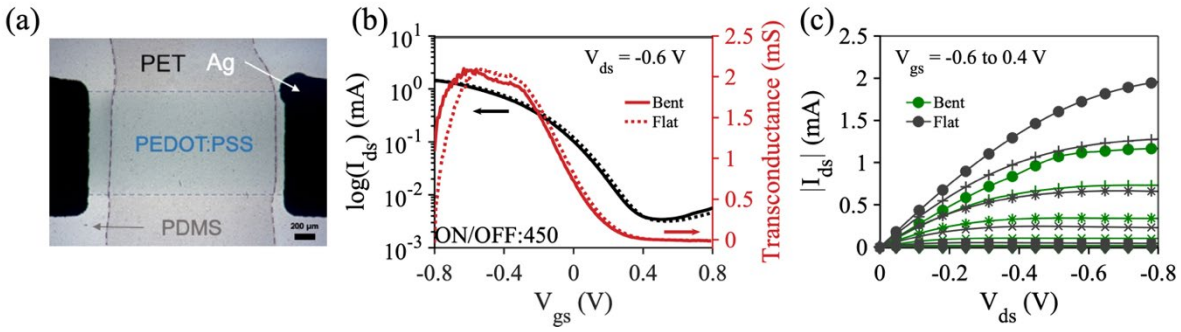

Figure 4.7 (a) Optical microscope image of PEDOT:PSS channel, Ag source/drain electrodes and PDMS on a PET substrate. Scale bar is 200 μm. Average transfer and output curves of flexible OECTs (n=3) with printed PEDOT:PSS channels, printed Ag source and drain electrodes, PBS gating media, and an activatedcarbon gate electrode measured while flat and bent. (b) Flat (dashed) and bent (solid) OECT drain current (black) and transconductance (red) vs gate voltage at a drain voltage of −0.6 V. (c) Flat (grey) and bent (green) OECT drain current vs drain voltage measured while applying a constant gate voltage ranging from −0.6 to 0.4 V.

average maximum transconductance of both flat and bent OECTs was calculated as 2.10 ± 0.20 mS. These results indicate that the performance of flexible OECTs is not significantly altered when bent to a radius of 30 mm.

The performance of our OECTs is compared to that of other OECTs using similar PEDOT:PSS formulations (Table 4.1). Ersman et al. reported screen-printed OECTs with two OECT configurations: one fabricated using carbon as source and drain electrode, the other with PEDOT:PSS source and drain electrodes [239]. Zabihipour et al. showed fully screen-printed OECTs on PET [240]. The OECTs discussed in these examples showed high performance, however, they employed a solid electrolyte and required a high gate voltage ($V_{gs} \approx 1.2$ V) to turn off the OECT. Sensi et al. studied the performance of carbon gate OECTs fabricated through screen-printing on a PET substrate, which showed a maximum transconductance of 0.7 mS [241]. With respect to the above examples, our OECTs shows a higher transconductance of 2.1 mS and a similar ON/OFF ratio, in the range of gate voltage from 0 V to 0.8 V.

Our results demonstrate that screen-printable PEDOT:PSS paste can be used to print electronic devices on flexible substrates using a PCB printer, and our printed flexible OECTs demonstrate performances similar to screen-printed PEDOT:PSS OECTs. The PCB printer can make increasingly complex designs that are easily modified compared to screen-printing methods.

Table 4.1 OECT materials and performance values

Method	Channel	LxWxH	Electrolyte	Gate	Source/ Drain	V_{ds} (V)	V_{gs} (V)	ON/OFF ratio	Ref.
Screen printing	PEDOT :PSS SV3	200 μm× 200 μm× 0.4 μm	PolyDDA	PEDOT :PSS SV3	PEDOT :PSS SV3	−1.5	0 – 1.2	10^4	[239]
Screen printing	PEDOT :PSS SV3	200 μm× 200 μm × 0.4 μm	PolyDDA	PEDOT : PSS SV3	Carbon	−1.5	0 – 1.2	10^2	[239]
Screen printing	PEDOT :PSS SV4	200 μm× 200 μm× 0.5 μm	PolyDDA	PEDOT : PSS SV4	Carbon	−1.0	0 – 1.5	10^3	[240]
Screen printing	PEDOT :PSS SV3	2 mm× 3 mm× 0.3 μm	PBS	Carbon	Carbon	−0.4	0 – 2.0	10^2	[241]
Screen printing	PEDOT :PSS SV3	1 mm× 1.5 mm× 1 μm	NaCl	Carbon	Silver	−0.6	−0.8 – 0.8	10^3	Current

Consequently, these OECTs can be easily integrated with multiple electronic components to facilitate the development of a printed bioelectronic device that can acquire, transmit, and process biological signals.

4.5.4 Characterization of PEDOT:PSS EDA sensors and measurements of EDA

Electronics can be used for epidermal stimulation, pain relief, muscle rehabilitation, and other treatments [227]. Stimulation requires electrodes to inject small amplitudes of current into the skin. In Figure 4.8(a), 200 cycles of a cyclic voltammogram (CV) applied to the PEDOT:PSS film on TPU are shown. Electrochemical testing occurred in PBS, an electrolyte that contains ionic species at concentrations that are biologically relevant, thus revealing information of how the system may operate when in contact with an aqueous environment, such as human sweat. As the voltage is cycled between −0.6 V and 0.8 V, the PEDOT:PSS film is reduced and oxidized causing a change in the current. The area of the curve traced by the current is the amount of charge exchanged during potential sweeping and is known as the charge storage capacity (CSC) of the electrode, which gives an indication of the ability of PEDOT:PSS electrodes to inject charge to the surrounding environment and stimulate tissues [32]. To increase the lifespan of a stimulating device the CSC

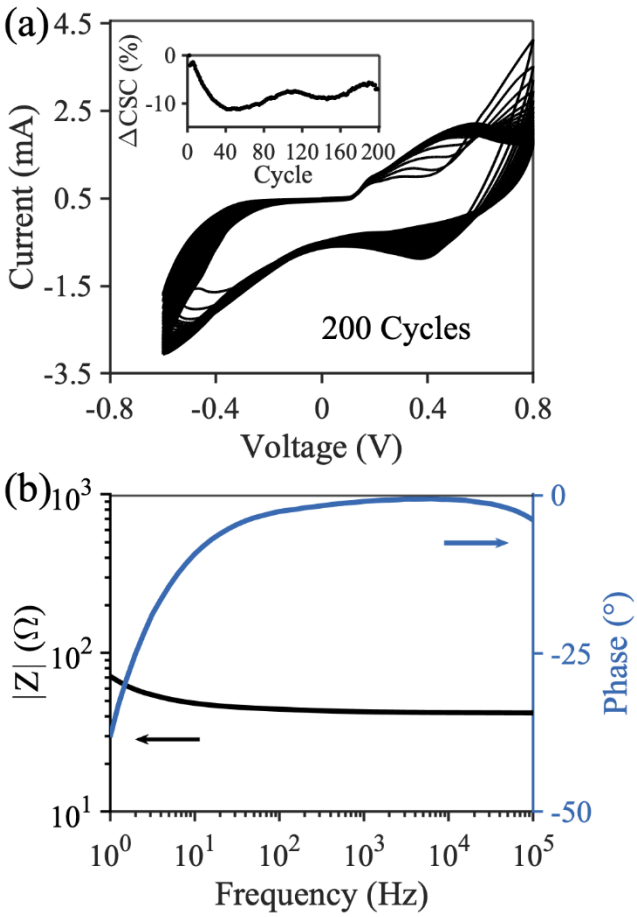

Figure 4.8 Electrochemical characteristics of PEDOT:PSS electrodes on stretchable TPU substrates. (a) Cyclic voltammogram (CV) of 200 cycles of applied voltage ranging between −0.6 V and 0.8 V and the resulting current in PEDOT:PSS on TPU electrodes. Inset shows the change in the charge storage capacity (%) from the second cycle to the 200th CV cycle. (b) Bode plot of impedance magnitude and phase vs frequency from EIS performed on PEDOT:PSS on TPU.

should be stable under repeated electrical loading. In the first cycle of CV, the CSC was ~30 mC. After 40 cycles of CV, in the CSC decreased by ~12% from the initial CSC. However, after repeating 200 cycles, the film regained ~5% of the CSC. Thus, the electrical performance of the films is stable after 200 repetitions of electrical loading in an aqueous environment, demonstrating the ability of these devices to be used for repeated epidermal stimulation.

To record electrophysiological signals accurately, it is important the electrode has low impedance at the low to high frequencies of signals found in the body (0.1–1000 Hz). In Figure 4.8(b), the impedance magnitude and phase of the PEDOT:PSS film on TPU acquired during EIS are shown. The phase of the impedance approaches 0° as the frequency increases, indicating the impedance of the device is almost purely resistive at high frequencies, a well-observed behavior of PEDOT:PSS electrodes in aqueous solutions. Therefore, the electrical activity measured with CV and the impedance magnitude is dominated by the PEDOT:PSS electrode in PBS. Additionally, the impedance, Z, of the film is low (<100 Ω) when measured at all frequencies, indicating excellent electrical performance, and demonstrating the potential for these films to be used to record signals at all the frequencies tested.

To further demonstrate the feasibility of printed PEDOT:PSS on a stretchable TPU substrate to function as a wearable electronic sensor, we measured the EDA during audiovisual stimulation in humans. EDA is a physiological signal registered on the skin and arising from the sweat glands

[242]. This bio-signal can be modulated by emotional states and consequently constitute a physiological indicator of an individual's temporary psychological state. EDA sensors can be also used as thermistors and photocells to capture physiological markers of emotions. EDA is sometimes assigned a threshold and used as a trigger for interactive art and as a tool to create data-driven music.

The EDA arises from the volume of sweat and change in ionic concentration in sweat on the skin. Figure 4.9(a) shows the PEDOT:PSS sensors placed on a volunteer while recording EDA. The PEDOT:PSS sensors are able to transduce the ionic current caused by change in sweat volume during stimulation, into conductance that is recorded by the data acquisition system. The signal was numerically filtered after acquisition using a fourth-order Butterworth low-pass filter at a cut-off frequency of 5 Hz. The resulting signal is the low frequency component of the EDA known as the skin-conductance level. The EDA was recorded with both standard stainless-steel electrodes (Figure B.12, Appendix B), and printed PEDOT:PSS electrodes (Figure 4.9(b)). The PEDOT:PSS electrode is mounted on a Velcro band, which is wrapped around the fingertip with the electrode in contact with the skin. Electrical connection is made with an alligator clip connected to the portion of the uninsulated Ag. The recorded conductance versus time measured with three PEDOT:PSS electrodes is shown in Figure 4.9(c), and has features typical of EDA signal. The rapid increase in

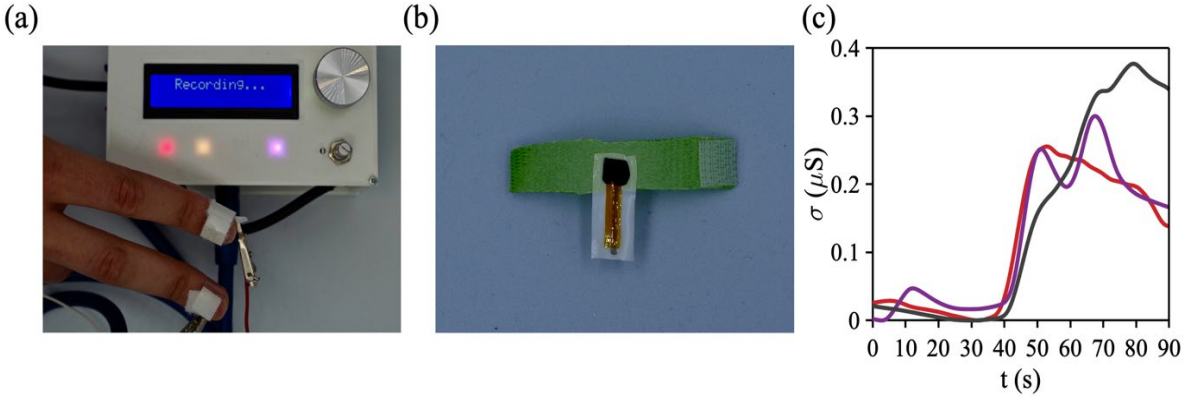

Figure 4.9 Photographs of the EDA signal acquisition device and the PEDOT:PSS EDA sensors and EDA measurements. (a) Recording EDA using PEDOT:PSS electrodes on a volunteer. (b) PEDOT:PSS (black square) in contact with Ag interconnect, insulated with Kapton tape (yellow), and printed on TPU (white). The electrode system is mounted on a Velcro band (green). (c) EDA signal in conductance vs. time acquired with PEDOT:PSS on TPU electrodes (n = 3). Conductance was measured on the same volunteer at 3 different time points using three different audiovisual stimulations.

conductance occurs due to a rise in sweat volume on the hands, which is part of the body's autonomic reaction to the audiovisual stimulation. The conductance versus time recorded without audiovisual stimulation is shown in Figure B.13(a) (supporting information) and displays a steadily decreasing flat curve. The properties of the EDA signal, such as, peak conductance, and rise time, i.e. the time between stimulus and peak conductance, depend on many factors that vary depending on the person under test, how often they have been exposed to the testing stimulus, and how well the electrode contacts the skin. To demonstrate this phenomenon, we recorded EDA signal from the same volunteer under identical testing conditions, using PEDOT:PSS electrodes, but recorded at three different time points (three curves in Figure 4.9(c)). The rise time, peak conductance, and number of peaks vary significantly even though the signal was acquired under the same conditions. Thus, the conditions in this experiment were not able to reproduce the recorded EDA signal, and the results are limited as a proof-of-concept indicating the PEDOT:PSS electrodes are suitable for recording EDA. As an example of the standard EDA signal acquired with a typical recording system, we measured the EDA signal recorded during stimulation with a standard EDA stainless-steel recording electrode (Figure B.13(b)). Although the EDA signal recorded with PEDOT:PSS electrode cannot be directly compared to that recorded with the stainless steel electrode due to the issues with signal reproducibility, there a few noteworthy advantages of the PEDOT:PSS electrodes. The main advantages of the PEDOT:PSS EDA sensor is its moderate conductivity, stability under stretching and bending, and conformability with the skin to make close contact, whereas the stainless steel screw is rigid and unable to make reliable contact with the skin. Additionally, the stability of the PEDOT:PSS electrodes in aqueous conditions is improved compared to stainless steel, especially since stainless steel corrodes when exposed to water for long time periods especially if a potential is applied to the system. Finally, the stable CSC of the PEDOT:PSS electrodes over 200 cycles of CV, is excellent for future applications where small amounts of current are used to stimulate EDA. An electrode with relatively high CSC can apply smaller potentials to generate the required currents to stimulate a physiological response, increasing the window of current injection for safe stimulation. Finally, the data demonstrates the ability of PEDOT:PSS stretchable electrodes to record EDA signals from the surface of the skin with onsets and peaks, characteristic of EDA bio-signals.

4.6 Conclusion and perspectives

We have demonstrated an adherent, highly stretchable and conductive PEDOT:PSS film screen-printed on a stretchable substrate using only commercially available, unmodified materials printed on unstretched, flat substrates using direct printing methods. The mechanical properties of the PEDOT:PSS device are moderately stable under 100% strain and were shown to be stretchable up to 600% strain with a resistance variation of 200 times the initial value. In the future, there should be a focus on enhancing the conductivity of the screen-printed PEDOT:PSS for large-area electronic circuit applications, however, the advantage lent by these films is their moderate conductivity that is stable under moderate levels of bending and stretching. In addition, the PEDOT:PSS ink was used as a channel material in a flexible OECT and the OECT possessed a moderately high ON/OFF ratio of ~1800. Further investigation is required to print a fully stretchable OECT and understand the printed OECT performance under stretching. Finally, we used PEDOT:PSS on TPU to directly interface with human skin and sense ion concentration variation in sweat and were able to detect an EDA signal. This electrochemical material system combines highly stable conductivity with facile fabrication processes to produce mechanically robust devices to reliably record biological signals for future applications in bioelectronics as well as in performing arts to monitor emotional states.

CHAPTER 5 A CURVED AND FLEXIBLE NEURAL PROBE FOR TARGETING DEEP BRAIN STRUCTURES

5.1 The complexity of recording from the vHp – a novel approach toward targeting deep brain structures

Recording with microelectrodes positioned at a controlled angle to the horizontal plane is crucial for analyzing brain activity in deep regions. For instance, current-source density mapping (detailed in Section 1.3.3) necessitates multiple recording sites oriented perpendicular to neuronal layers [243]. In the ventral hippocampus (vHP), attaining this orientation with linear probes is particularly challenging due to its complex three-dimensional structure and depth [244]. Nonetheless, conducting current-source density analysis in the vHP would yield essential information about the spatial and temporal organization of synaptic inputs in space and time, offering novel insights into the inputs driving vHP activity [16].

Complex brain functions require the cooperative interaction of both local and distant neuronal assemblies. Synchronized neuronal network activity is observed as large-amplitude, periodic fluctuations in local field potential (LFP) recordings, commonly referred to as brain rhythms. Research into neuronal activity has shown consistent correlations between rhythmic changes in extracellular voltage recorded from groups of neurons and their cognitive processes [245].

Specifically, investigations of the hippocampus have highlighted distinct differences in neuron physiology and functionality along the dorso-ventral axis [246]. The dorsal hippocampus (dHP) is crucial for spatial navigation and memory, while the ventral hippocampus (vHP) plays an essential role in emotional and social behaviors [247]. Notably, the most ventral third of the hippocampus exhibits marked differences from the rest of the structure, supported by studies on internal connectivity, gene expression, and input-output patterns [248].

Hippocampal rhythms are categorized by frequency, including delta (1 to 4 Hz), theta (6 to 10 Hz), and gamma (25 to 100 Hz), each associated with specific cognitive functions. For instance, the theta rhythm is observed during specific sleep stages or when animals explore new environments, and it has been connected to the encoding of new information. Rhythmic variations in extracellular voltage mainly arise from synaptic currents, which are inputs from different hippocampal subfields or brain regions, resulting in ion movements across neuronal membranes. Current source density

analysis allows for the examination of the distribution of these transmembrane currents within hippocampal layers, providing significant insights into the origins and characteristics of hippocampal rhythms.

A significant limitation in conducting current source density analysis is that recording sites need to be equally spaced and oriented in specific directions. For the hippocampus, these sites must be perpendicular to the pyramidal cell layer. This recording configuration in the vHP is extremely difficult to achieve using linear probes. Typically, 2D or 3D microelectrode arrays are necessary to accurately position the recording sites perpendicularly to the pyramidal cell layer. However, even with these architectures, the placement remains limited to an orthogonal approach, and some deeper structures are inaccessible. Successfully aligning linear electrode arrays perpendicularly to neuronal layers in deep brain regions can be achieved using oblique probe trajectories. Nevertheless, in the ventral hippocampus (vHP), this technique may necessitate crossing both brain hemispheres, resulting in considerable tissue damage.

We created an innovative solution for this problem by designing a unique probe with curved multisite electrodes. The subsequent sections will cover the fabrication of a flexible, curved microelectrode array implanted with silk shuttles. We improved the electrical properties of the probe with optimized electrodeposited PEDOT:BF_4 coatings and analyzed their performance using electrochemical impedance spectroscopy, examining both scenarios with and without the silk shuttle. To assess electrode placement precision, the silk-shuttled curved probes were tested using a rotating implantation device to target both the dorsal and ventral hippocampus. Finally, we validated the probe's recording abilities by implanting it with electrodes aligned along the CA1-dentate gyrus axis of the dorsal hippocampus to record local field potentials and unit activities.

5.2 Strategies for implantation of compliant neural probes

Silk shuttles have become essential for effectively implanting advanced flexible neural interfaces, especially those made with materials like parylene and equipped with conductive polymer coatings, such as PEDOT, on microelectrode arrays [170]. These flexible probes provide significant advantages over rigid implants, including enhanced biocompatibility, precise microscale spatial resolution, and the ability to adapt to brain tissue movement while preserving high signal quality [170]. However, their natural lack of stiffness makes direct insertion into brain tissue extremely difficult, often resulting in buckling or damage to the tissue [139]. To overcome this issue, silk

fibroin acts as a temporary, stiffened shuttle, offering crucial mechanical support for the delicate probe during. This silk support system is advantageous due to its proven biocompatibility, adjustable high mechanical strength (which can be optimized through processing), and its ability to degrade into safe amino acids within the body. The shuttle aids in the accurate delivery and conformal placement of the flexible probe, ensuring that the microelectrodes maintain close contact with the target neural surface for optimal recording, after which the silk structure safely dissolves. This combination of adaptable temporary mechanical support, precise delivery capability, and harmless resorption makes silk an exceptionally suitable, and often superior, option compared to other biodegradable polymers or insertion techniques for implementing delicate, high-performance flexible neural electronics.

5.3 PEDOT-based neural recording electrodes

PEDOT is an optimal conducting polymer for neural recording applications due to its excellent chemical stability and electrical characteristics [249, 250]. Its capacity to convert ionic signals into electronic signals allows PEDOT electrodes to outperform traditional metallic ones, a quality that has spurred decades of research focused on using PEDOT electrodes in vivo for neural signal recording [251]. Modifying electrodes with PEDOT enhances the effective surface area and reduces impedance, producing recording electrodes with a high signal-to-noise ratio (SNR) making it an ideal choice for interfacing with neuronal environments [89, 202, 252]. Furthermore, PEDOT has been shown to foster tissue regeneration [253], and its capability to incorporate charged species into its film has been leveraged for organic electron-ion pumps aimed at controlled drug delivery [254].

Due to the crucial role of PEDOT electrodes as ion-to-electron transducers, optimizing their electrical and surface properties is essential for effective recording. Key factors influencing the electrical characteristics of the PEDOT coating include the electrochemical deposition technique, the selection of dopants, and the quantity of material deposited, which is determined by the charge during electrodeposition [255]. Furthermore, both the dopant and film thickness can greatly affect surface properties [256]. The surfaces of PEDOT films show nodular features that vary based on the electropolymerization employed. Studies reveal a direct correlation between surfaces with increased roughness and nodularity, demonstrating a decrease in electrical impedance and improved charge transfer capabilities [257, 258].

5.4 Microfabrication of organic materials

Microfabrication must be performed in a clean room to minimize the introduction of contaminants and particles that could reduce product yield and quality. A clean room is defined according to the ISO standard 14644-1 as:

"A room in which the concentration of airborne particles is controlled, and which is constructed and used in a manner to minimize the introduction, generation, and retention of particles inside the room and in which other relevant parameters, e.g. temperature, humidity, and pressure, are controlled as necessary."

The work presented here was performed in a Class 100 cleanroom (FS209E classification – equivalent to an ISO 5 cleanroom), which allows a maximum of 100 particles smaller than 0.5 micrometers per cubic foot. In comparison, a standard office building has between 500,000 to 1,000,000 particles of 0.5 microns or larger per cubic foot. Although it is the third cleanest environment according to the FS209E classification, achieving this level of cleanliness requires a rigorous process.

Chemical vapor deposition of parylene C: Parylene is a polymer derived from poly-(para-xylylene), belonging to a group of semicrystalline, hydrophobic polymers that includes parylene N, parylene C, parylene D, and parylene HT (Figure 5.1). Parylene C is distinguished by the presence of a single chlorine atom on its benzene ring and is frequently employed as an insulating layer in various bioelectronic applications. This is due to its chemical inertness, electrical resistivity, low moisture permeability, and certified biocompatibility [259]. Parylene is applied as thin films at room temperature using chemical vapor deposition (CVD). Chain-growth polymerization forms the polymer, where monomer units are added sequentially to the expanding chain. In the CVD process, the dimer di-para-xylylene is initially sublimated into vapor at ~150°C under low pressure (1 Torr). When heated above 550°C in a vacuum of less than 1 Torr, the dimer

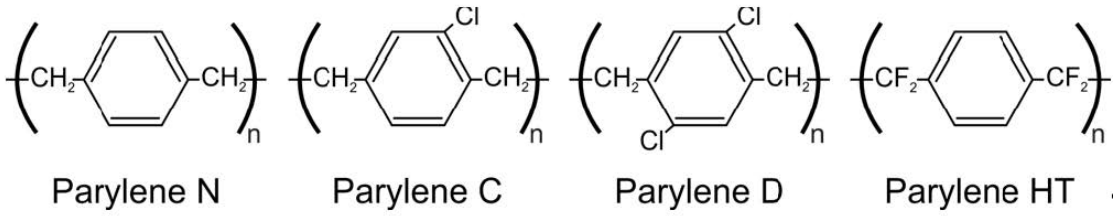

Figure 5.1 Chemical structure of parylene types. Reproduced with permission from [1]

undergoes pyrolysis, resulting in the formation of two para-xylylene monomer units. A pressure gradient then moves the monomers into a room-temperature deposition chamber, where they adhere to the surface and spontaneously polymerize, creating high-molecular-weight parylene thin films.

The chemical vapor deposition of parylene thin films is a solvent-free process that generates no by-products, effectively circumventing challenges common to other polymerization techniques such as dipping, spraying, or spin-coating. These alternative methods often suffer from non-uniform film thickness, pinholes, and poor film conformality. In contrast, parylene CVD produces conformal coatings, with monomer molecules penetrating deeply into crevices to create pinhole-free films. This process has been demonstrated to fill sub-micron gaps and deliver highly uniform coatings, even over large and complex substrates.

Photolithography: Micro-patterning of inorganic or organic materials utilizes photosensitive solutions known as photoresists (Figure 5.2). A thin, uniform layer of photoresist on the wafer surface is achieved through spin coating (Figure 5.2(i-iii)). The resist is then exposed to UV light via a photomask containing the pattern to be transferred (Figure 5.2(iii)). Photoresists can be categorized as positive or negative. In positive resists, the photochemical reaction during exposure weakens the polymer, which increases its solubility to the developer, resulting in the removal of the exposed areas (Figure 5.2(iv)). Conversely, in negative photoresists, exposure causes the photoresist to polymerize, allowing the developer solution to remove only the unexposed areas, leaving the negative resist pattern. The development process typically occurs in a basic aqueous solution. When exposed, the photosensitive compounds induce a chemical reaction that transforms the insoluble positive resist into a highly soluble acidic compound or cross-links the soluble negative resist, rendering it insoluble in the basic developer.

Metal evaporation: This method allows for the deposition of nanometer-thin metal layers using a high-energy electron beam (Figure 5.2(v)). A heated filament induces the thermionic emission of electrons, supplying the necessary energy for the material's evaporation. The metal is placed in a crucible, where it is thermally evaporated and then condensed onto substrates located above the crucible. This evaporation occurs under low vacuum with a typical pressure of 10^{-6} Torr to avoid contamination from other vapors and ensure unobstructed transfer of the metal particles to the substrate. Once the metal has been deposited, the resist has fulfilled its role and can be removed

using an appropriate solvent. The *lift-off* technique involves directly transferring the desired pattern via the resist. In this process, the resist is dissolved in the solvent, which eliminates the metal from the areas covered by the resist while retaining the deposited metal in the regions that were not protected (Figure 5.2(vi)).

Reactive-ion etching: Parylene's chemical inertness makes chemical etching impractical. As a result, selective etching of parylene generally relies on dry etching techniques. Reactive ion etching (RIE) enables the removal of parylene through a chemically reactive plasma. Substrates patterned with a thick photoresist mask (Figure 5.2(vii-viii)) are placed in a vacuum chamber (10^{-3} Torr), where a gas is introduced and ionized via a radiofrequency electromagnetic field. This process generates reactive plasma that removes the unprotected (organic) material (Figure 5.2(ix)). The volatile byproducts released from the substrate are drawn away via a vacuum pump. After RIE, photoresist stripping using acetone or other organic solvents removes the resist etch masks, resulting in the final parylene probe (Figure 5.2(x-xi)).

5.5 Methods

5.5.1 Microelectrode array fabrication

PaC–based curved probes with thin–film Au microelectrode arrays, comprising sixteen 12 x 12 μm electrodes with a 75 μm interelectrode distance center-aligned along a 7 mm radius circular path, were designed using AutoCAD and KLayout and fabricated by lithography (Figure 5.3(A-D)) and fabricated by lithography. First, glass wafers (4" diameter, 0.5 mm thick, WaferPro) were cleaned with acetone, IPA, and deionized water (DIW). A 2 μm thick PaC film was deposited on the wafer by chemical vapor deposition (SCS Labcoter® 2, PDS 2010). The patterning for the Au layer was performed by photolithography and a lift-off process. First, LOR5A photoresist (MicroChem, USA) was spin-coated on the parylene-coated glass wafer at 4000 RPM for 30 s and baked at 170 °C for 3 min followed by OIR 674-11 (FUJIFILM, USA), spin-coated at 4000 RPM for 30 s, and baked at 90 °C for 90 s. The wafer was exposed to UV light (45 mJ cm^{-2}) in a mask aligner (MA-6, Suss MicroTec, Germany), and developed for 75 s using AZ726 developer (Merck, Germany). Before metal deposition, the wafer was plasma treated with reactive-ion etching (RIE) using O_2 plasma (100 W, 10 sccm O_2, 1 min) to improve the adhesion of the metal layer to parylene. 10 nm of Ti and 100 nm of Au were deposited by electron beam evaporation (Thermionics, USA), followed by lift-off in MICROPOSIT™ REMOVER 1165 (The Dow Chemical Company, USA)

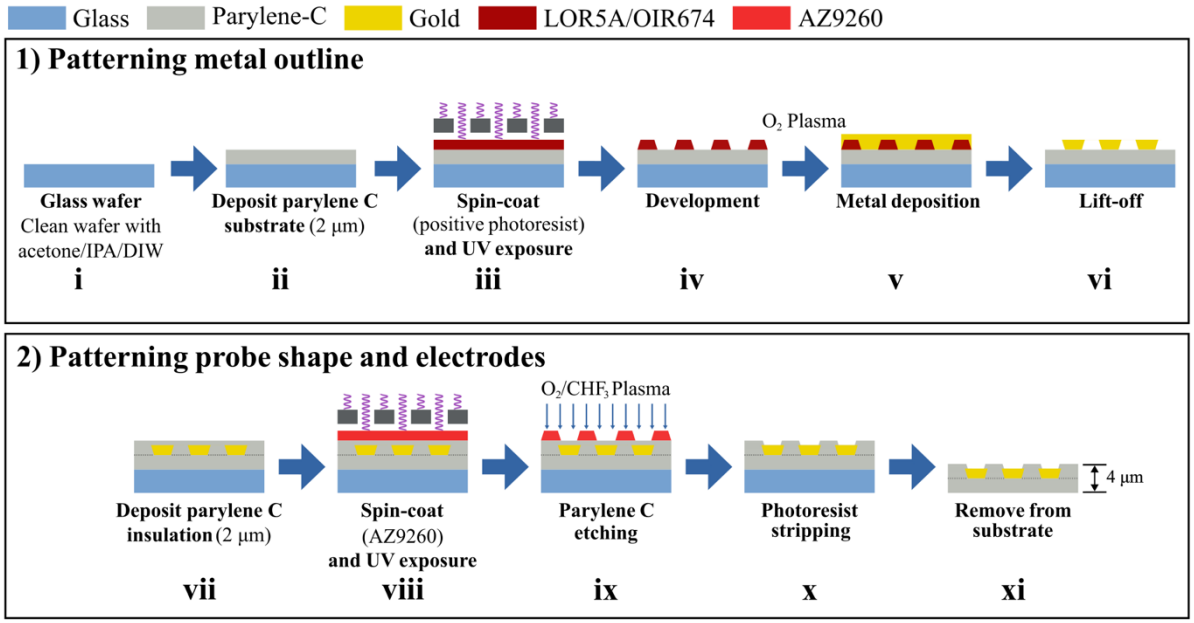

Figure 5.2 Illustration of the photolithography process using a parylene coated glass wafer. In step (1) the gold electrodes, traces, and connection pads are patterned for by step (2) where a thick positive resist (AZ9260) is patterned to create a protective mask during the parylene etching process. The result is free-standing probe containing exposed gold microelectrodes and pads with the traces insulated between two parylene layers.

for 24 h. After lift-off, a second 2 µm-thick PaC film was deposited to insulate the metal traces. Outlines of the individual probes and the Au electrodes and contacts were patterned by photolithography with AZ9260 photoresist (AZ Electronic Materials, USA) spin-coated at 2400 RPM for 40s, baked at 110 °C for 160 s, exposed to UV light (500 mJ cm^{-2}) and developed in deionized water (DIW) and AZ400 K (AZ Electronic Materials, USA) at a 4:1 ratio for 3 min and 45 s, for a final resist layer thickness of ~12 µm measured with a profilometer (KLA Tencor). Patterning was achieved by dry etching the 4 µm PaC film with RIE. O_2 (20 sccm) and CHF_3 (2 sccm) were used for etching at 200 mTor pressure and 200 W plasma power for ~25 min. The photoresist was removed by submerging the wafer in acetone for 1 min and rinsing with DIW. Subsequently, the wafer was visually inspected for defects with optical microscopy (Olympus BX51).

5.5.2 Neural probe assembly

The PaC probes were released from the glass wafer by immersing them in DIW and carefully lifting a corner of the parylene layer with a surgical blade. This step allowed water to seep beneath the

parylene, releasing the probe. Once released, the probe was transferred using fine-tipped brushes onto a transparent, flexible polyethylene terephthalate (PET) substrate for alignment and bonding. To improve the electrical connection of the 4 µm thin parylene probe, a flat flexible cable (FFC, 0.25 mm pitch, 17 contacts, Molex) was electrically bonded to the probe's contact pads. This was

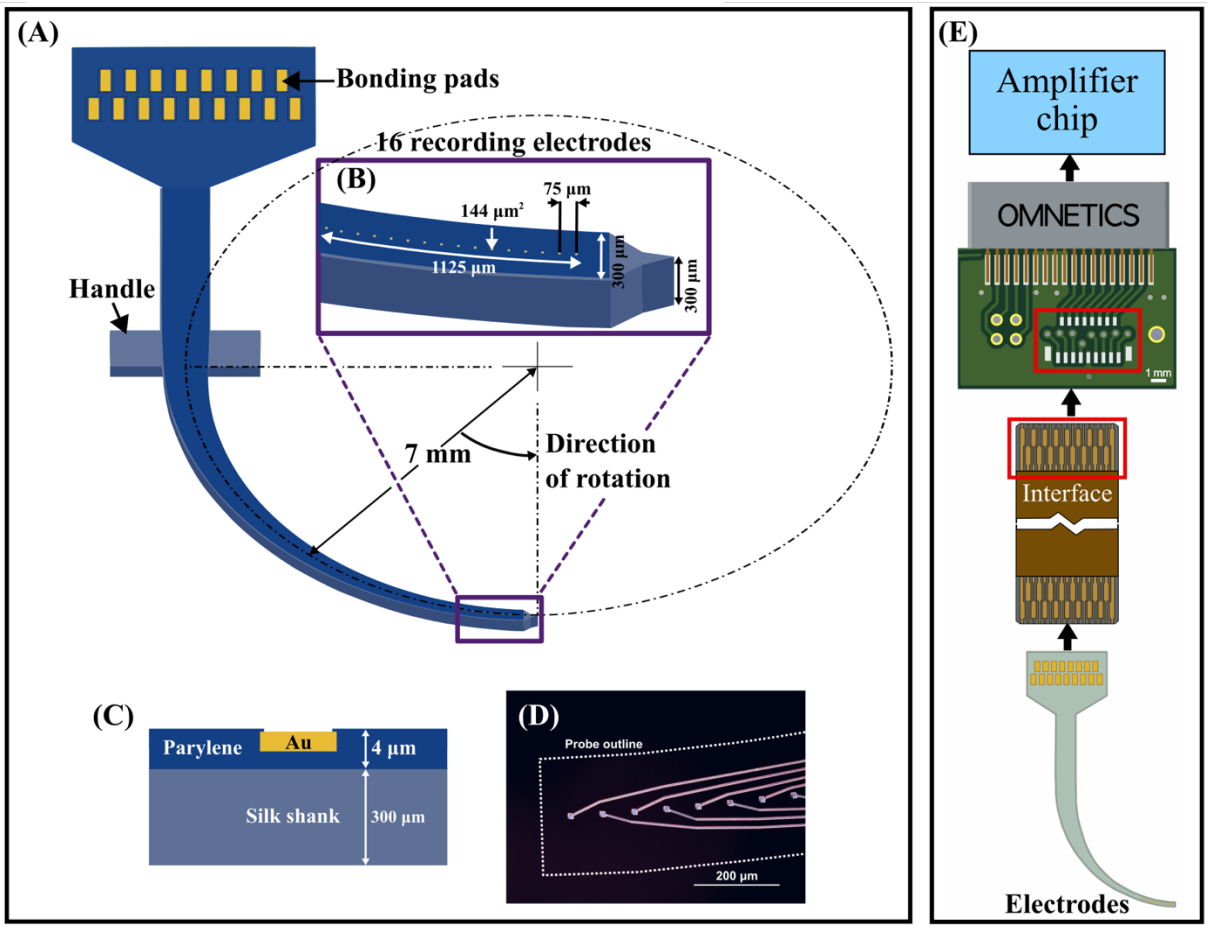

Figure 5.3 Design of a curved microelectrode array adhered to a silk shank shuttle. (A) 3D schematic of overall probe desion as well as (B) close ups of 16 gold recording sites. (C) Cross-section of an electrode showing the silk shank and parylene probe with exposed electrodes. (D) Microscope image of recording sites and parylene probe outline (dashed lines). (E) Electrodes connected to the external circuit through a cable that interfaces with the probe and a PCB.

achieved using an anisotropic conductive film (ACF) containing silver filler (128-32-F1, 1 mil thick, Creative Materials). ACFs consist of micron-sized conductive particles embedded in thermosetting polymer resins. When pressure is applied to both the top and bottom connection pads of two circuits by a heated element, the adhesive flows, fixing the compressed conductive particles between the contacts and establishing an electrical connection. Due to the low filler content (1-5%)

and the z-axis constrained compression, electrical connectivity occurs only along that axis, preventing short-circuiting between adjacent contacts.

The ACF created a conductive path between the metal contacts of the FFC and the connector pad of the parylene probe. It was applied to a cable attached to a glass substrate maintained at 60 °C. The parylene probe, which was lightly adhered to transparent PET, was positioned over the probe's contact pads under a microscope. A silicone-lined metal clamp, preheated to 130 °C, applied pressure to the probe/ACF/cable during curing (130 °C for 3 min). After the assembled probe was released from the clamp, epoxy was applied around the cable/probe connections to secure them. Additionally, a PCB was designed to interface with a flexible printed circuit (FPC) connector and a miniature connector (36-pin, NPD-36-DD-GS, Omnetics). The free end of the cable in the cable/probe assembly was inserted into the FPC connector, allowing this setup to connect with external circuits for conducting electrochemical and neural recording experiments in the subsequent sections (Figure 5.3E)

5.5.3 Electrode surface characterization

Electrodeposition and in vitro electrochemical characterization studies were conducted using a potentiostat (BioLogic) connected to a three-electrode glass cell. All electrochemical experiments were conducted within a Faraday cage (BioLogic) because of the high signal noise caused by the small dimensions of the microelectrodes. The gold microelectrodes (144 μm^2) of the parylene probe served as the working electrode, with a platinum coil acting as the counter electrode, and a Ag/AgCl (3 M NaCl) (RE-5B) electrode functioning as the reference. Electrochemical impedance spectroscopy (EIS) was acquired at open circuit potential using a 10 mV amplitude sinusoidal voltage input with frequencies ranging from 1 Hz to 100 kHz.

Electrochemical cleaning and surface restructuring of gold microelectrodes: All gold electrodes underwent electrochemical cycling and EIS in deaerated 0.2 M H_2SO_4, with a nitrogen blanket maintained during the measurement. The potential was cyclically swept within a potential range of 0 V to +1.6 V vs Ag/AgCl at a scan rate of 0.3 V s^{-1} for a maximum of 50 cycles.

Parameters for electrodeposition of PEDOT:BF_4: The galvanostatic deposition of PEDOT films on separately prepared, electrochemically cleaned, gold electrodes was conducted in deaerated solutions of acetonitrile containing 0.02 M EDOT and 0.12 M $TEABF_4$. For galvanostatic electropolymerization, the current density was maintained at 1 $mAcm^{-2}$ (current, i = 1.44 nA) for

various durations (t = 50 s to 50 min) to achieve a total charge during polymerization (i x t/planar surface area) ranging from 50 to 3,000 $mCcm^{-2}$.

Electrode electrochemical characterization: CV and EIS were performed for electrode characterization in deaerated PBS (0.01 M phosphate buffer, 0.0027 M potassium chloride and 0.137 M sodium chloride, pH 7.4, at 25 °C) (Sigma Aldrich). CV was used to record five potential cycles between –0.8 V and +0.6 V vs Ag/AgCl at a scan rate of 0.1 Vs^{-1}. EIS measurements from silk-shuttled microelectrode arrays were recorded immediately after submerging the probe in PBS. Silk dissolution occurs upon electrolyte contact, so the time in solution may be a relevant factor in the impedance outcome. The first electrode was measured within one minute of contact, and the 16th electrode of the array was measured within twenty minutes of solution contact.

Electrode surface characterization: All scaning electron microscope (SEM) images were acquired using a Quattro variable pressure SEM (Thermo Fisher) with accelerating voltages ranging from 10 kV to 20 kV, a current of 100 pA or 140 pA, and a pressure of 80 Pa. Working distances varied between 7 mm and 10 mm. Energy dispersive X-ray spectroscopy (EDS) was used to confirm the cleaning of the Au surface.

5.5.4 Development of silk shuttle

Preparation of aqueous silk solution: Aqueous silk fibroin solution was regenerated from *Bombyx Mori* cocoons following a protocol established in the literature [260-262]. Twelve cocoons were cut into eight pieces each and boiled in an aqueous solution of 0.02 M Na_2CO_3 for 1 h. The resulting fibers were rinsed once in boiling deionized water (10 min), then three times (10 min each) in room temperature (~21 °C) DIW and dried for 24 h in ambient conditions. The dried silk fibers were solubilized by dissolving in a 9.3 M LiBr solution at 60 °C for 1 h to yield a 20% w/v solution. This solution was dialyzed (3.5k MWCO, SnakeSkin™, ThermoFisher) against DIW for 48 h, changing the water three times (after 1 (1^{st}), 4 (2^{nd}), and 24 h (3^{rd})). After dialysis, the solution was filtered through a 5 µm syringe filter, placed in fresh dialysis tubing, and covered with poly(ethylene glycol) powder (molecular weight, M_N = 8,000, Sigma-Aldrich) to increase the concentration of silk. The final concentration of the aqueous silk solution was 10−12% w/v. The silk solution was stored at 4 °C for later use.

Microfabrication for the PDMS mold: The overall shape and tip of the silk shuttles were designed in AutoCAD to have the shaft center aligned along a circular path with a radius of 7 mm, a shaft width of 300 μm, and a sharp tip (Figure 5.3A,B). A 4-inch silicon wafer (1 mm thick, UniversityWafer) was used to prepare the PDMS mold. The microfabrication process for patterning the wafer was performed identically to the parylene lithography (for steps (i) through (vi), Figure 5.2), except that a layer of Al_2O_3 (120 nm) was deposited as a metal etch mask. After lift-off, the patterned wafer was etched using deep reactive-ion etching (DRIE) (PlasmaLab ICP System 100, Oxford Instruments) to create ~300 μm high silicon structures. To create the PDMS mold, PDMS was cast, cured, and peeled off the patterned silicon structures to be utilized to contain silk fibroin and shape the silk shuttle.

Probe alignment and silk deposition: To facilitate probe alignment in the mold, the mold was first filled with DIW. The parylene neural probe was positioned in the PDMS mold with the electrode face down to prevent silk from covering the electrode surface. This was achieved using a micropositioner, a rotation stage, and making adjustments with fine-tip paintbrushes. After the water evaporated, the parylene adhered lightly to the PDMS. An aqueous silk fibroin solution was drop-cast in the mold on top of the parylene probe and left to dry overnight under ambient conditions. Once dry, the silk-shuttled parylene probe was carefully removed from the mold with forceps and held lightly clamped for at least 12 hours between two sections of soft silicone, to ensure the curved probe lay flat in the rotation plane without deflection, and stored in ambient conditions for 12-24 h before implantation.

5.5.5 Rotating implantation of the curved probe

To successfully implant the curved probe, several design considerations for the implantation device were necessary. The small radius of the approach curve, the height of the mouse skull and surrounding tissues, along with spatial limitations in the surgical area, constrained the available design space. Considering these factors, we used AutoCAD to model the surgical environment and determine the appropriate dimensions. High-precision machining (CNC) was used to create the device parts.

Figure 5.4(A) displays a schematic of the rotating implantation and probe placement. The curved probe was attached to a holder that kept the centerline of the curve at a distance of 7 mm from the axis of rotation, effectively constraining it to a circular path with a 7 mm radius in the rotation

plane. The top and bottom sections of the probe holder ensured proper alignment, while magnets integrated into the holder secured the probe, allowing for the mount's removal post-implantation. The probe holder was connected to the manipulator arm of the stereotax, enabling movement in the x and y directions, as well as rotation around the z-axis in the x- and y-planes, using a screw located at the center of rotation (Figure 5.4(B)).

Using target coordinates and a reference map of the mouse brain, we determined the angle of rotation and the probe's insertion point on the brain's surface with AutoCAD software [263]. We

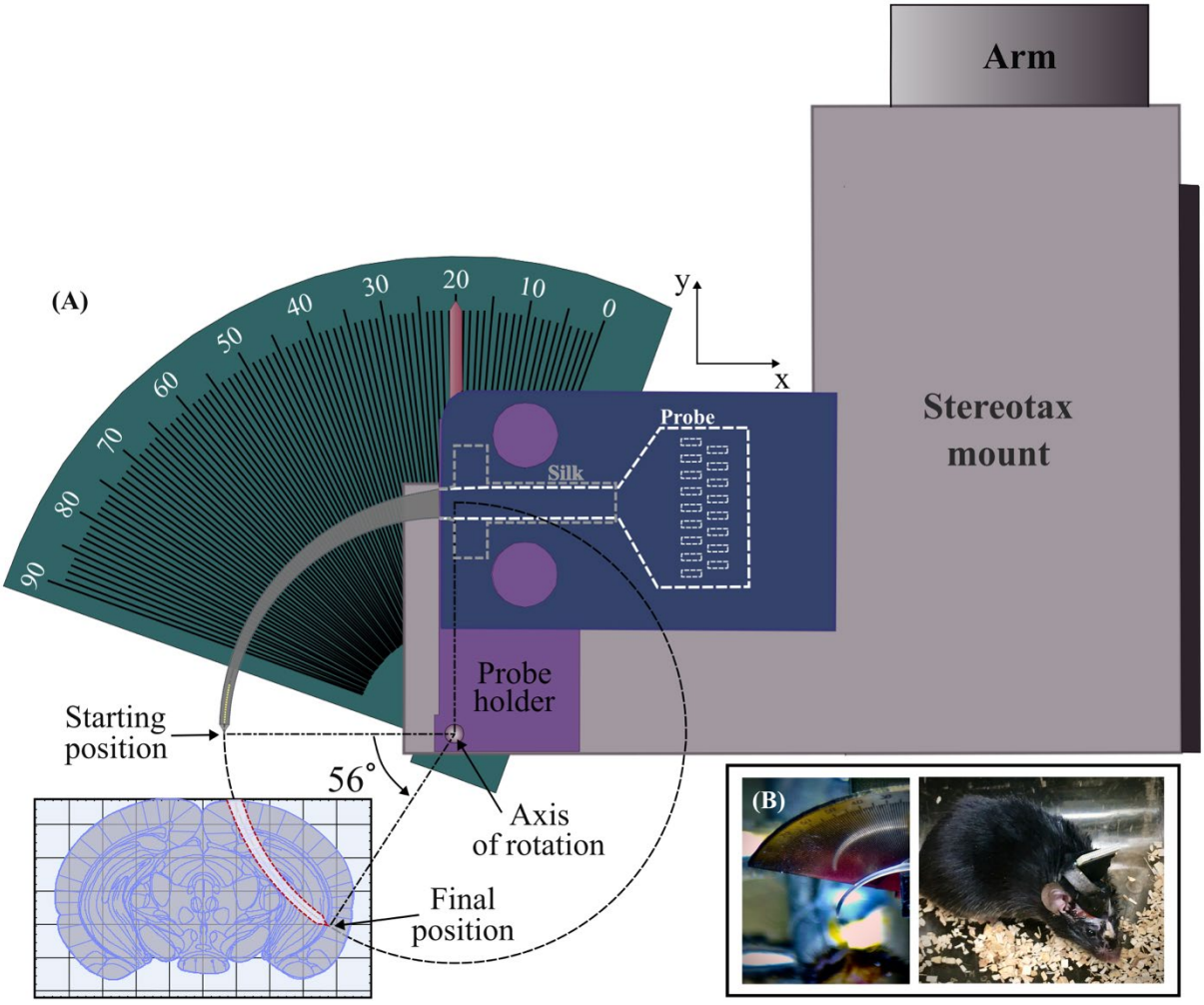

Figure 5.4 Strategy for the rotating implantation of the silk-shuttled flexible curved probe in the vHP. (A) The silk probe is secured in a holder and mounted on a rotating implantation device. The probe initiates its rotation with the tip perpendicular to the y-axis and rotates a predetermined amount around the z-axis to achieve the final position, with the tip placed at the target coordinates. (B) Images of the mounted silk probe immediately before implantation (left) and of a mouse implanted with a probe connected to a PCB, with the connector pins exposed (right).

overlaid a model of the probe's geometry onto the reference brain. The approach curve was chosen to ensure that the electrode sites were perpendicular to the CA1 pyramidal layers while minimizing the volume of tissue disrupted in the implantation path. Our aim was to prevent damage to both hemispheres while reaching the target. Once the probe was positioned at the target, we calculated the angle of rotation based on the arc length from the target to the point on the curve that is perpendicular to the y-axis.

5.5.6 Implantation of the curved probe in vivo

Surgical Procedures: All procedures involving animals were conducted in accordance with Canadian Council of Animal Care guidelines and approved by the CHU Sainte-Justine Research Center Animal Ethics Board (CIBPAR). Two sets of C57BL/6J mice (Jackson Laboratory stock no. 000664 (2–4 months age) were used in two separate experiments: (Experiment 1) Mice were implanted with probes in either the ventral or dorsal hippocampus, to determine whether the probe was correctly oriented and positioned in the brain. (Experiment 2) Mice were implanted with probes in the dorsal hippocampus and underwent 1 week of implantation followed by recording during wake and sleep vigilance states. The number of subjects (n) in each experiment was: (1) n=5 (2 males, 3 females), and (2) n=2 (males). The animals were maintained under controlled environmental conditions (23 °C, 12 h light/dark cycle), with food and water provided ad libitum. They were initially anesthetized with 5% isoflurane in O_2 and surgeries were performed under anesthesia with 2% isoflurane. For surgery, the head of the mouse was immobilized in a stereotaxic apparatus. The body temperature was kept constant at 37.5 °C with a heating pad.

Each mouse was implanted with one silk-shuttled curved probe. A miniature stainless-steel screw, attached with wire to an Omnetics connector, was driven into the skull above the cerebellum and served as a ground/reference electrode, along with a stainless-steel anchor screw located toward the posterior of the brain. After locating Bregma, holes were drilled into the skull at the brain surface coordinates (determined with AutoCAD): (ventral hippocampus) –3.08 mm anterior/posterior, 0.39 mm medial/lateral, relative to Bregma, or (dorsal hippocampus) –1.94 mm anterior/posterior, –2.52 mm medial/lateral, and –2.12 mm dorso/ventral, relative to Bregma. The silk-shuttled curved probes were placed in holders and attached to the rotating implantation device described in the previous section.

Using the stereotaxic arm, the probe tip was positioned at the surface coordinates, and a hole was created in the dura just below the tip. The probe was then rotated so that the tip aligned perpendicular to the y-axis, above the brain. This marked the point where the rotation began. The probes were subsequently rotated, lowering them to the surface of the cortex until the probe rotated a total of (ventral hippocampus) 56° or (dorsal hippocampus) 63° measured from the point perpendicular to the y-axis to penetrate the tissue and reach the target coordinates: (ventral hippocampus) −3.08 mm anterior/posterior, 3.80 mm medial/lateral, and −3.79 mm dorso/ventral, relative to Bregma, and (dorsal hippocampus) −1.94 mm anterior/posterior, −1.26 mm medial/lateral, and −2.12 mm dorso/ventral, relative to Bregma.

The external part of the electrodes was affixed to the skull using dental cement (Paterson Dental). At this point, the probe holder was carefully removed and the flexible cable of the probe was attached to the mechanical FPC connector of the PCB, followed by additional dental cement to fix to the skull. Connector pins, attached to the top of the PCB, were exposed on the implant's surface (Figure 5.3(E) and Figure 5.4(B)). For mice in experiment (1), after probes were implanted, the animals were left undisturbed for the duration of the experiment (2 weeks). Mice in experiment (2) were permitted to recover for one week following surgery before recording experiments began.

Acute recordings: Neural signal recordings were amplified and digitized using a 32-channel Intan RHD electrophysiology amplifier array with an on-chip 16-bit analog-to-digital converter and a serial peripheral interface. The signals were high-pass filtered at 1 Hz, amplified with a gain of 192 V/V, and recorded at sampling rates of 30 kSamples/s per channel. The amplified signal was acquired using an Open Ephys acquisition board and processed and visualized with the Open Ephys GUI [264]. Recordings were filtered between 1 and 300 Hz to display the local-field potentials component and filtered between 400 Hz and 12 kHz to reveal single-unit activity (the firing of a single neuron).

Histology: Following termination of experiments, animals were deeply anesthetized with a ketamine/xylazine/acepromazine cocktail (80/12.5/2.5 mg kg^{-1}) via an intraperitoneal injection. Animals were transcardially perfused with phosphate-buffered saline (PBS). Extracted brains were then soaked in 4% w/v PFA for 1 week to preserve electrode tracks. The sample was sectioned into 100 µm slices using a Vibratome (Leica VT 1200S) with an oscillating razor blade. The sample was attached to a metal block placed inside a container filled with PBS and then transferred with a

brush to multi-well plates filled with 1×PBS and 0.02% w/v azide. This ensured that the evaluated interface corresponded to the probe, which was confirmed after staining via fluorescent microscopy. Finally, slices were mounted in 4,6-diamidino-2-phenylindole (DAPI) Fluoromount-G (SouthernBiotech) and stored in the dark at 4 °C.

5.6 Results

5.6.1 Cleaning process and surface reconstruction of the Au microelectrodes

SEM images of the as-prepared microfabricated curved Au microelectrode array are shown in Figure 5.5. The images in Figure 5.5(A-C) reveal the well-defined outline of the parylene probe, the exposed metallic microelectrode surface, and the parylene-insulated traces. The high-resolution SEM image in Figure 5.5D shows that the surface of the thin film gold microelectrodes, prepared from thermally evaporated Au, exhibits a polycrystalline structure characteristic of thermally evaporated thin gold films [265]. The deposition of gold using a thermal evaporation process occurs through gas-phase nucleation of charged nanometer-sized gold clusters, which deposit a dense polycrystalline thin film with {111}, {100}, and {110} facets on the substrate surface [266].

Gold is an electrochemically active surface that experiences oxidation via anion replacement, adsorption, and place-exchange with oxygen species in solution, leading to the formation of an oxide layer [267]. A stable solid gold oxide with a +III oxidation state can arise from the reaction: $2Au + 3H_2O \rightarrow Au_2O_3 + 6H^+ + 6e^-$. It is well-known that peaks of electrochemical oxidation in cyclic voltammetry (CV) curves correspond to specific surface facets of gold electrodes based on their surface energy (γ) with $\gamma_{(111)} < \gamma_{(100)} < \gamma_{(110)}$ [268] [269]. Repeated cycling of the electrochemical potential causes the restructuring of the gold surface, influenced by the surface energy of the facets. Research indicates that electrochemically restructured gold surfaces with a predominant fraction of {111} facets exhibit lower onset oxidation potential and higher peak currents during the cycling of electrochemical potential [270].

The quality of the electrochemically active gold surface greatly influences the outcomes of electrochemical experiments [271]. Typically, both the peak currents recorded during cyclic voltammetry and the frequency response seen in electrochemical impedance spectroscopy rely on the gold surface's composition. Notably, research has shown that the initial stages of electropolymerization of conducting polymers depend on the electrode's chemical properties and reactivity [272]. After the microfabrication process of the curved microelectrode array, these

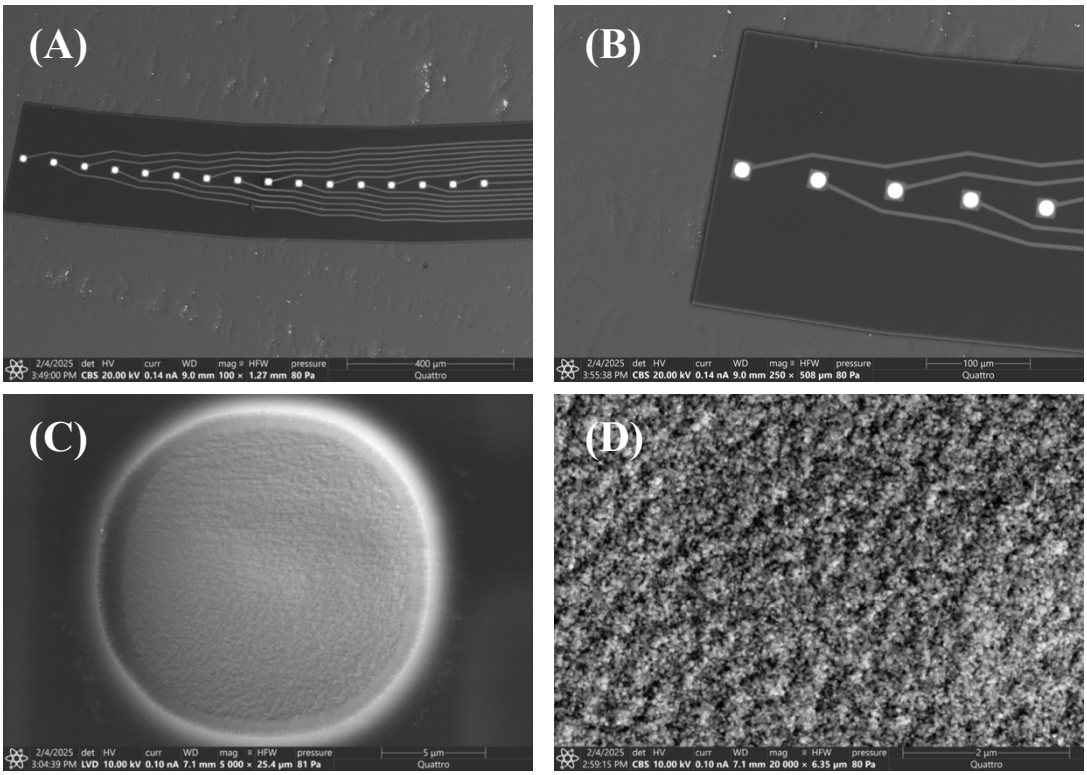

Figure 5.5 SEM of unmodified gold microelectrodes taken at magnifications of (A) 100x, (B) 250x, (C) 5,000x and 20,000x with an accelerating voltage of (A and B) 20 kV and (C and D) 10 kV.

microelectrodes encounter various ambient contaminants outside the cleanroom environment. Furthermore, contamination can occur during microfabrication. For example, metal impurities can deposit during the metal evaporation step, and incomplete removal of the photoresist etching mask or the parylene layer can result in residual organic and sulfur contaminants on the electrode surface [121]. Therefore, it is essential to clean evaporated gold before it undergoes electrochemical modification. An effective technique for removing impurities involves electrochemical potential cycling in a diluted sulfuric acid solution until a stable CV scan is achieved [273].

The curved microelectrode array was cleaned with acetone, isopropanol (IPA), and deionized water (DIW), remaining otherwise unmodified. An elemental analysis of the electrode surface, conducted through energy-dispersive X-ray spectroscopy (EDS) (Figure 5.6(D)) revealed residual metal impurities, including iron, nickel, and aluminum, alongside other contaminants found on the surface.

Cyclic voltammetry was utilized to clean and reconstruct the gold microelectrodes' surface. The potential window was established between 0 V and +1.6 V, covering the complete spectrum of gold oxidation and reduction reactions, as shown in Figure 5.6(A). The initial CV displays a wide peak believed to be related to the polycrystalline structure of the electrode surface. As the cycling progressed, two peaks began to appear gradually. After 50 cycles, the voltammogram revealed two distinct anodic peaks, originating from the broader peak, located at +1.16 V and +1.32 V, alongside a single cathodic peak at +0.84 V. The lower potential anodic peak is attributed to the oxidation of Au {100} facets, while the broader peak at a higher potential, corresponds to the oxidation of Au {111} facets [270]. With the increase in cycle number, the ultimate shape, potential, and current intensity of the broader anodic peak changed, reflecting surface reconstruction [270, 274].

Microelectrode cyclic voltammograms are distinctly affected by the scan rate, particularly at slower rates where the transport of charged particles to the electrode surface mainly occurs through hemispherical diffusion [270, 275, 276]. Consequently, the scan rate plays a vital role in determining the reconstructed surface structure of microelectrodes. Previous studies indicate that the electrochemical behavior shown in Figure 5.6A points to a preference for forming {100} and {111} facets [270]. This process involves the selective oxidation of gold atoms at high-energy {110} sites during the forward scan, which can then dissolve into the electrolyte at the maximum potential limit. During the reverse scan, these mobile atoms are redeposited onto lower-energy stable facets like {111} and {100}, which minimizes surface energy [277]. However, because of the rapid scan rate, not all reduced gold atoms from the higher-energy {111} facets may have adequate time to attain the lowest energy state, resulting in the observed formation of intermediate energy {100} facets. Overall, the changes in cyclic voltammograms after cycling indicate a reorganization of the initially prepared polycrystalline gold microelectrode surface into a more stable structure.

Changes in the cathodic and anodic peak areas are evident from the first to the last cycles. The integration of anodic (Q_a) and cathodic (Q_c) charges indicates a Q_a/Q_c ratio of 1.52 during the first cycle, while this ratio nears unity (0.88) by the 50th cycle. This observation suggests an additional irreversible oxidative process occurring during the initial forward scan, possibly associated with the oxidation of metal impurities from the electrode surface into the electrolyte solution as part of the cleaning process. The EDS analysis conducted after potential cycling corroborates this finding (Figure 5.6(E)). Notably, metal impurities such as trace amounts of Al, Fe, and Ni in the

unmodified gold, along with sulfur, likely from sulfur-based compounds in the residual photoresist, were eliminated from the surface.

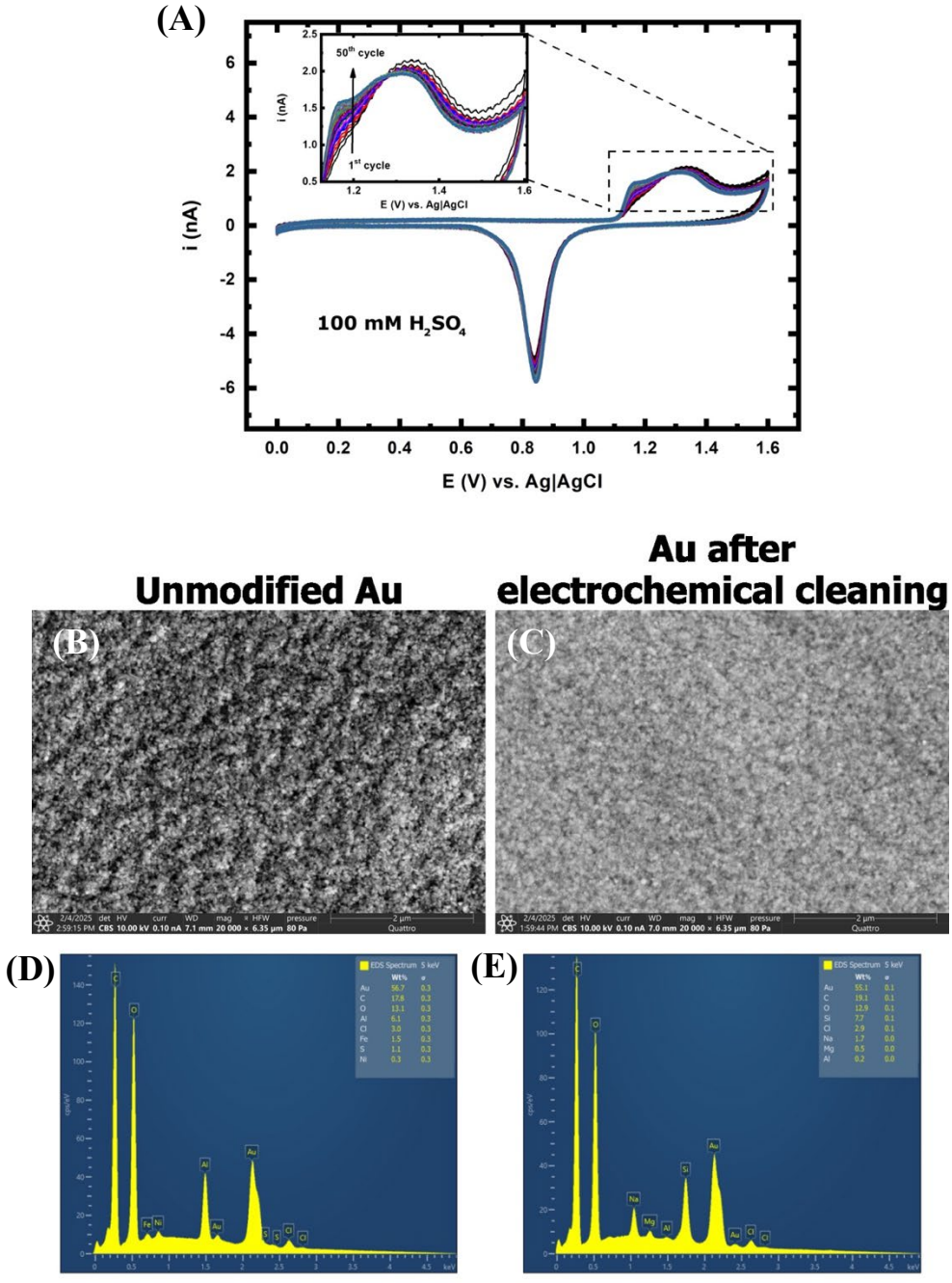

Figure 5.6 Electrochemical cleaning of Au microelectrodes. (A) 50 cycles of CV performed in 100 mM H_2SO_4 at a scan rate of 200 mVs^{-1}. (B) SEM image and (D) EDS of Au before CV and (C) SEM and (E) EDS after CV.

The SEM images of both unmodified and cleaned gold reveal a polycrystalline film with a distinct grain structure. The image of the unmodified gold (Figure 5.6(B)) displays a stronger shadow contrast on its prominent features, while the clean gold image (Figure 5.6(C)) has reduced contrast, implying a more uniform surface. This uniformity may arise from the oxidation and redeposition of high-energy crystal facets at the edges of prominent structures, transitioning to lower energy surface states. Additionally, the electrical characteristics improved following electrochemical cleaning, as reflected in the electrode impedance measurements taken before and after potential cycling (Table 5.1). The data indicated at least a 31% reduction in impedance across all monitored frequencies, signifying that the more stable surface of the electrochemically cleaned gold enhances electron/ion charge transfer at the electrode.

Table 5.1 Values of impedance for unmodified gold and electrochemically cleaned gold

Frequency (Hz)	Before cleaning |Z| (MΩ)	After cleaning |Z| (MΩ)	Change (%)
1	1.8×10^3	1.1×10^3	–37
10	212.6	147.1	–31
100	26.4	17.6	–34
1,000	3.8	2.4	–36
10,000	0.6	0.3	–39
100,000	0.1	0.05	–41

5.6.2 Electrodeposition of PEDOT:BF_4

The mechanism of EDOT electropolymerization remains under examination, although some general principles are widely recognized within the scientific community [278, 279]. Classical nucleation theory outlines the primary nucleation process as having two phases: the induction period and the steady (or stationary) nucleation period. During the initial induction phase, EDOT monomers diffuse from the solution to the electrode surface. Once EDOT is oxidized at the electrode, it forms a doubly charged sigma-dimer, which then becomes an aromatic, neutral dimer following proton elimination [157]. This dimer is quickly oxidized and couples with a radical cation monomer, initiating the oligomerization process. The oligomerization of conducting polymers begins in the solution near the electrode surface. Research shows that the onset of the

oligomer deposition process is influenced by the chemical properties and reactivity of the electrode [272]. The next stage is the deposition of these oligomers. Once the oligomers saturate the diffusion layer adjacent to the interface, they start to precipitate onto the electrode, leading to the formation of conducting polymer nuclei that initiate the growth process. At this stage, the process is diffusion-controlled, relying on the movement of monomers.

The initial nuclei formed at the start of the process continue to grow through progressive nucleation. This is characterized by an increasing number of nuclei that form on the electrode surface during electropolymerization. Consequently, this process leads to nucleation in directions both parallel and perpendicular to the electrode. As polymerization advances, the nuclei merge to create polymer globules made up of species with varying conjugation lengths [272]. The main activities during the nucleation phase include the expansion of polymer chains and the growth of globules on the electrode surface. When the oxidation potential is applied for a designated time, the globules start to overlap, eventually achieving complete coverage of the surface with polymer globules [258]. With longer polymerization time, a second layer of significantly larger polymer globules forms. Continuous application of potential or current causes PEDOT films to undergo rapid 2D and 3D growth, driven by mass transport and charge transfer mechanisms [280].

In the curved microelectrode array, gold electrodes underwent PEDOT:BF_4 deposition through galvanostatic electrodeposition (Figure 5.7(A)). Initially, during the electropolymerization process,

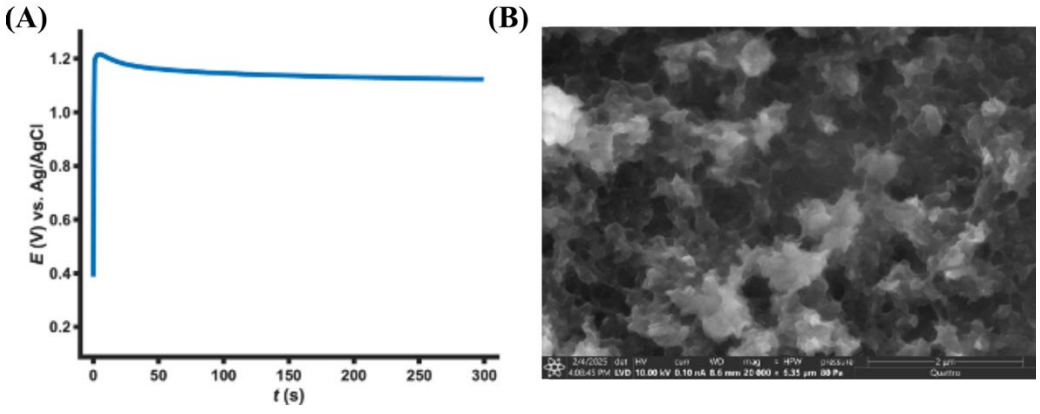

Figure 5.7 PEDOT on gold microelectrodes. (A) Chronopotentiometric curve acquired during galvanostatic deposition for a total charge density (C_d) of 0.3 Ccm^{-2} (i = 1.3 nA; j = 1 $mAcm^{-2}$; t = 300 s). (B) SEM of PEDOT-coated Au microelectrode taken at 20,000x magnification with an accelerating voltage of 10 kV.

the potential rises briefly before decreasing after several seconds, a phenomenon that is well-documented in galvanostatic electropolymerization studies. The peak potential's intensity is affected by the applied current density. This rise in potential indicates the onset of oligomerization, during which the initial polymer is consumed. At the same time, charged oligomers accumulate at the electrode, causing a reduction in the oxidized monomer species and leading to the potential drop observed after a few seconds [156].

The morphology of the PEDOT:BF_4 coating was examined through SEM analysis (Figure 5.7B). The conducting polymer layer on the gold microelectrodes displayed a porous morphology, defined by a vast interconnected network of agglomerated areas. SEM images further indicated that these regions feature an open structure that serves as ion transport pathways, essential for improving interaction with the biological medium [185, 281]. Consequently, conducting galvanostatic deposition under these conditions facilitates faster PEDOT electropolymerization kinetics, likely leading to the noted porous morphology [282].

5.6.3 The influence of deposition charge on the electrical properties of PEDOT

The surface of PEDOT films exhibits nodular features that change based on the electropolymerization conditions used. The thickness of PEDOT films, determined by the charge applied during electrodeposition, leads to increased surface roughness and nodular structures. Research shows a direct correlation between surfaces that exhibit greater roughness and nodularity and a reduction in electrical impedance, as well as an enhancement in charge transfer capability [89]. The surface topography also plays a crucial role in the adhesion and growth of cells on PEDOT films. Rougher films have been shown to boost neural cell adhesion and proliferation, while nodular films attract fewer cells [256]. Furthermore, the advantages of PEDOT films on cell viability decline past a specific thickness, as high levels of unreacted EDOT monomer and mobile dopants can remain trapped within thicker films.

Here, we aim to investigate the effect of film thickness on the electrical properties of PEDOT:BF_4 films. Figure 5.8 shows the images of PEDOT:BF_4 films produced with various amounts of charge through electrodeposition. As the charge during electropolymerization was increased, the impedance of the final PEDOT coatings decreased (Figure 5.9) and the coatings became darker and more opaque. The color and thickness of the electrodeposited films are primarily determined by the amount of charge applied to form them. As the films grew thicker, they became more opaque

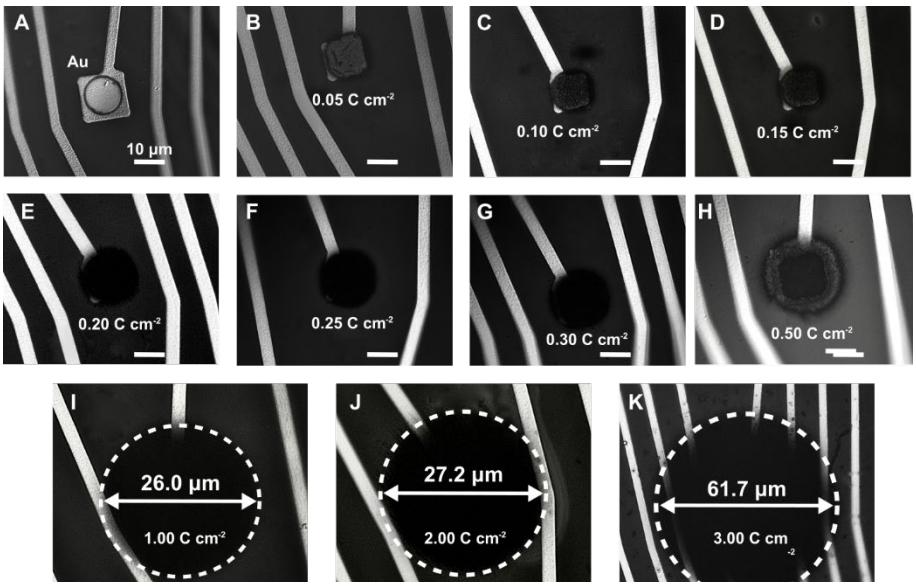

Figure 5.8 Optical microscope images of (A) Au and PEDOT deposited at (B) 0.05, (C) 0.1, (D) 0.15, (E) 0.20, (F) 0.25, (G) 0.3, (H) 0.5, (I) 1.0, (J) 2, and (K) 3 Ccm^{-2}.

and darker in color. The thin PEDOT films, synthesized with 0.05 and 0.1 $Ccm^{-2,}$ were semi-transparent light blue (visible to the eye), whereas the thick films, formed at higher charge densities, were opaque and dark blue.

The SEM image shown in Figure 5.7 illustrates PEDOT:BF_4 deposited at 0.3 Ccm^{-2}. The typical nodular morphology of PEDOT is evident in the film, corresponding to the opaque film observed in the optical image of the 0.3 Ccm^{-2} films (Figure 5.8G). At 0.5 Ccm^{-2}, PEDOT overgrowth is observed, with thicker PEDOT accumulating around the edges of the microelectrode. As charge deposition increases, the PEDOT films grow progressively wider and thicker, extending far beyond the microelectrode area onto the parylene. Above 0.3 Ccm^{-2}, the thickness of the PEDOT films is likely to negatively impact cell viability. Furthermore, the adhesion of the PEDOT film is compromised, particularly for the PEDOT that has grown atop the parylene. Mechanical stress applied to the flexible probe due to bending or to the PEDOT film during implantation could easily damage or dislodge the coating. Additionally, the spread of the PEDOT film at the highest charge density (Figure 5.8K) is so extensive that it may lead to short-circuiting between microelectrodes. Thus, films with high deposited charge densities and thickness are expected to adversely affect the microelectrode array's performance and integration with neural tissue.

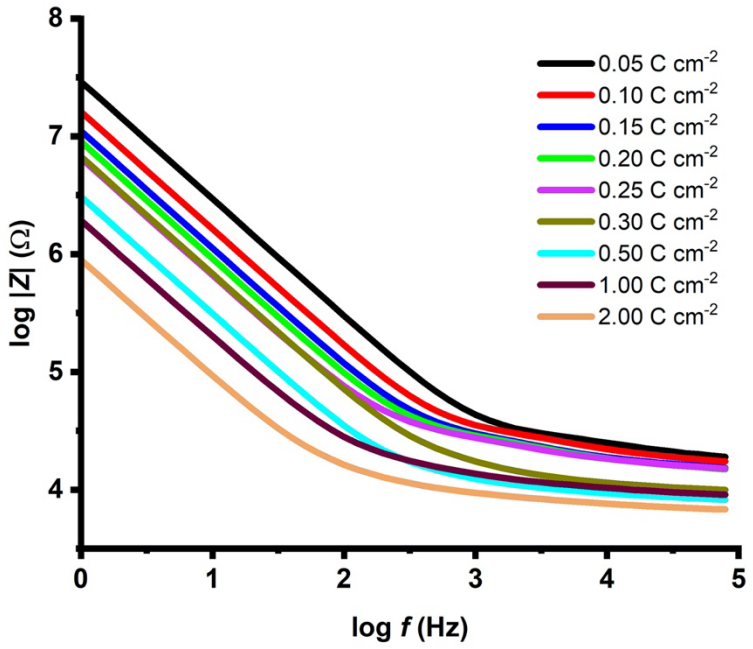

Figure 5.9 EIS of PEDOT coatings on gold microelectrodes for different amount of applied charge density (0.05 to 2.00 Ccm^{-2}) in PBS.

5.6.4 Comparison of optimized PEDOT-coated and uncoated Au microelectrodes

Charge storage in electrodes occurs through the formation of electric double layers at the electrode/electrolyte interface or is associated with redox reactions involving charge transfer across the electrode. The charge transfer mechanisms in PEDOT are explored through cyclic voltammetry experiments. During the forward voltage scan of potential cycling, positive mobile cations are expelled from the PEDOT layer into the solution, replaced by positive holes injected into the PEDOT from the electrode. This process reverses in the backward scan, leading to a decrease in hole density within the PEDOT. The voltammogram displays current peaks, which the Butler–Volmer electrochemical model can replicate, describing a faradaic current resulting from redox reactions. Following the peak, the current levels off, indicating a capacitive current [283]. Consequently, it is assumed that PEDOT operates as a pseudocapacitor, demonstrating both capacitive and faradaic charge transfer [284]. However, this assumption has been contested in

several critical studies [285]. Recent models of cyclic voltammetry in PEDOT do not rely on redox reactions, instead focusing on the coupled ion-electron diffusion and migration as explained by the Nernst-Planck-Poisson equations, often referred to as drift-diffusion equations. This perspective links the oxidation peaks to hole injection into the undoped polymer and cation expulsion, while reduction peaks are associated with electron injection and cation incorporation.

The cyclic voltammograms of PEDOT:BF_4 films deposited with a charge density of 0.3 Ccm^{-2} on the Au microelectrode surface are shown in Figure 5.10A. CV was performed in PBS, with potentials cycling between -0.8 V and +0.6 V vs. Ag/AgCl at a scan rate of 100 mVs^{-1}. In the forward scan, a broad anodic peak, attributed to the injection of holes and expulsion of cations, appears over a wide potential range. A well-defined characteristic CV peak cannot be identified. In the backward scan, a broad cathodic peak at approximately -0.7 V corresponds to electron injection and cation incorporation [285]. The area confined by the CV curve represents the electrode's charge storage capacity (CSC), which is a measure of the electrochemical performance, particularly relevant for neural stimulation applications [32]. The PEDOT films dramatically increased the area of the gold electrode's CV. The ability of PEDOT to store and transfer charge

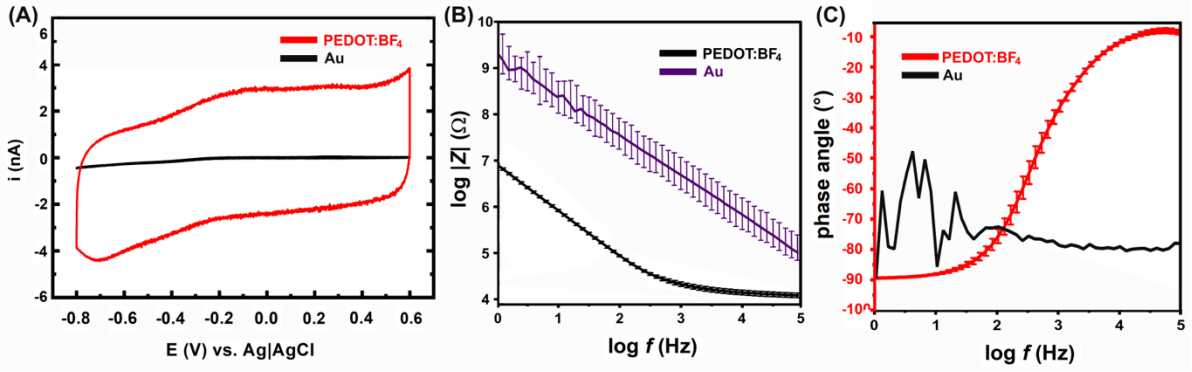

Figure 5.10 Electrochemical characterization of 0.3 Ccm^{-2} PEDOT-coated and unmodified Au microelectrodes performed in PBS. (A) Cyclic voltammetry of PEDOT-coated gold (red) and uncoated gold (black) performed at a scan rate of 100 mVs^{-1}. (B) Log plot of the impedance magnitude (Z) vs frequency (f) for PEDOT (black) and Au (purple). (C) Phase vs frequency (f) for PEDOT (red) and gold (black)

results from its rough and porous three-dimensional surface structure, which allows ions to incorporate into the bulk of the film, increasing its double layer capacitance [145].

The impedance spectra of a PEDOT-coated gold microelectrode deposited with a charge density of 0.3 Ccm^{-2} and a clean Au microelectrode is shown in Figure 5.10B. Below frequencies of 1 kHz

the impedance of 0.3 Ccm^{-2} films were two orders of magnitude lower than that of Au. The cut off frequency of PEDOT-coated electrodes, determined from the 45° phase angle of the impedance spectra occurs at approximately 300 Hz (Figure 5.10C). The cut-off frequency is the frequency where charge transfer transitions from primarily resistive to capacitive mechanisms [28]. Frequency-independent resistive charge transfer is preferred for electrophysiology applications. Purely capacitive electrode impedance results in a 90° phase shift of the potential recorded at the electrode as well as signal attenuation. This can result in significantly distorted signals. Conversely, purely resistive charge transfer mimics the phase of the signal, providing an accurate representation of the electrophysiology processes. The phase angle measurements of gold electrodes are significantly impacted by noise at low frequencies, and are close to 90° at frequencies above 100 Hz. The impedance magnitude at 1 Hz is approximately 9 MΩ. The electrical performance of the Au electrode in PBS results from its small geometric surface area, which dramatically increases the electrode impedance. The PEDOT coating has the same planar surface area as the gold electrode, but the roughness, porosity, and nodularity dramatically increases it's geometric surface area, offering a clear electrochemical advantage over the Au microelectrodes. The electrodeposited PEDOT:BF_4 films provide both the highest surface area and the lowest impedance.

5.6.5 Characterization of silk shuttled PEDOT microelectrodes

Silk fibers coated the curved neural probes to shape the tip and enhance the mechanical strength of the ultra-thin parylene probe, enabling its implantation in the brain along a curved path. A silk shuttle was fabricated on the back of the PEDOT:BF_4-modified microelectrode array. To avoid insulating the electrode surface with silk, the microelectrode array was positioned electrode-side down in the PDMS mold before silk solution application. SEM imaging revealed a uniformly distributed layer of silk on the probe's backside, reflecting a smooth surface (Figure 5.11B). This demonstrates that the silk fiber effectively covers the parylene substrate, providing a precise curvature and pointed tip, while ensuring the gold microelectrode area remains silk-free for optimal charge transfer and reliable neural signal acquisition (Figure 5.11A). To further investigate, we measured the impedance of PEDOT-coated microelectrodes before and after applying silk to see if silk deposition impacted the electrical properties. Figure 5.11C illustrates slight impedance increases at high frequencies and a left-shifted phase angle post-silk application, indicating potential partial coverage of the electrode surface. Overall, the low impedance of the silk-shuttled

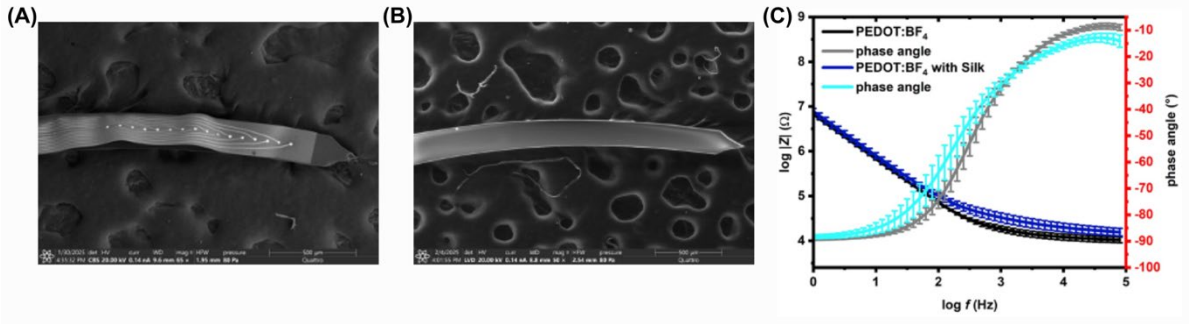

Figure 5.11 Characterization of probe with silk shuttle. SEM images of the (A) bottom of the shuttle, and the (B) probe on the top of the shuttle showing the Au electrodes. Images taken at 50x magnification and with an accelerating voltage of 20 kV. (C) Bode plots of PEDOT coated electrodes before silk deposition and after silk deposition, performed in PBS.

curved PEDOT-coated microelectrode array suggests that it is an excellent candidate for high-performance neural recording electrodes.

5.6.6 Curved probe orientation and location

The silk-shuttled flexible curved probes were successfully inserted into the brain without dura in five anesthetized mice, with three probes implanted in the ventral hippocampus Figure 5.12(D-F) and two in the dorsal hippocampus (Figure 5.12(A-C)). The accuracy of electrode placement and the orientation of the curved probe were evaluated by assessing DAPI-stained tissue slices containing the trajectory of the probe after implantation. Two of the five curved probes were successfully implanted (Figure 5.12(C,F)). We observed that the other probes either did not achieve full rotation, causing the final electrode placement to occur more ventrally than expected, or bent out of plane during the rotational insertion, resulting in electrode placement in a different anatomical plane than the one targeted.

The initial in vivo results indicated a need to improve our implantation strategy for the flexible neural interface. We observed that the silk-shuttled probes were flat and did not bend outside the plane of rotation prior to implantation, and they were implanted without resistance into the tissue. However, we noted that the probe was not completely secured in the probe mount, and both the mount and the rotating implanter required several modifications during the surgical procedure. Thus, we believe that the issues with probe implantation arose from design flaws in the implantation device. Before we conducted the implantations for the recording experiment, a new

implantation device (shown in Figure 5.4) was designed to address the problems observed during the initial surgeries, primarily focusing on securing the position of the silk shuttle “handles” and increasing the force applied to hold the probe using small magnets.

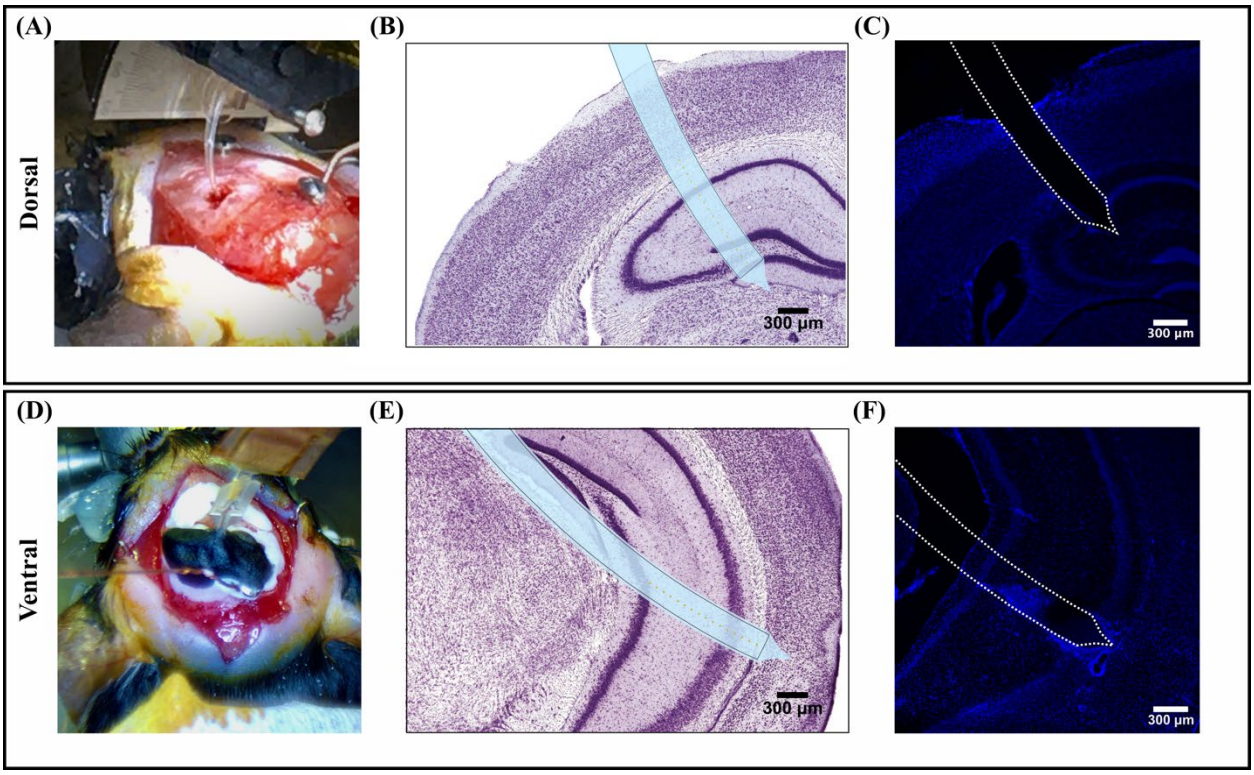

Figure 5.12 Outline of a 16-site silk-shuttled flexible curved probe positioned at the target coordinates in the (A-C) CA1-dentate gyrus (DG) axis of the dorsal hippocampus, and (D-E) CA1 pyramidal cells of the ventral hippocampus. (A, D) Images of the curved probe following implantation. (B, E) Reference images used for mapping the probe’s position at the target coordinates. (C, F) Fluorescence images of DAPI staining on coronal slices of the brain showing the trajectory of the probe implanted in the hippocampus.

5.6.7 Acute recordings in the dorsal hippocampus

Acute in vivo measurements were performed with our silk-shuttled curved probes, resulting in the recording of both LFPs and single-cell activity. Figure 5.12(A) shows a picture of one of the penetrated probes implanted inside a mouse brain, along with a fluorescent microscope image of a probe with the tip placed at the dorsal hippocampus target (Figure 5.12(C)) selected from a reference map of the brain (Figure 5.12(B)).

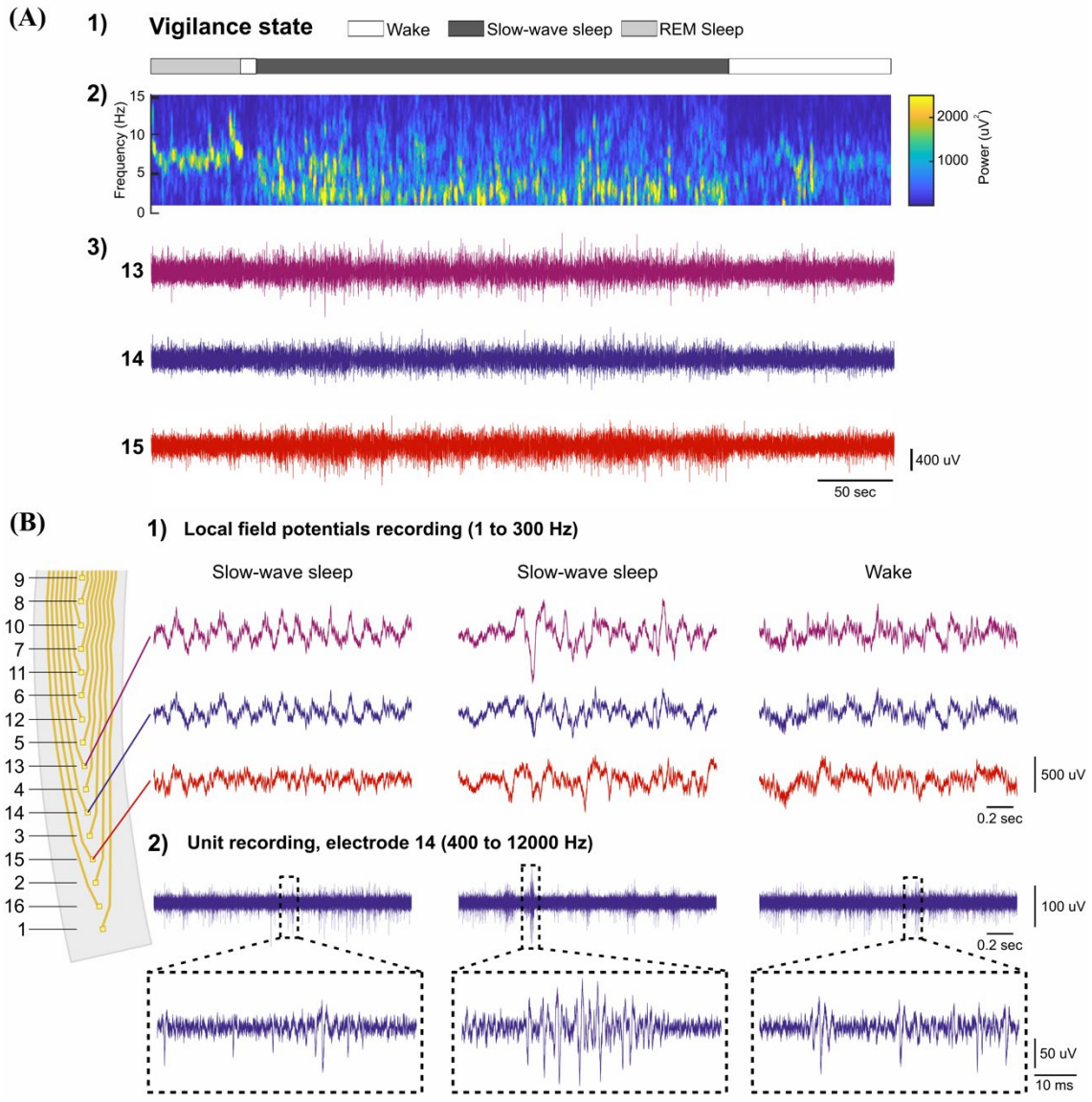

Figure 5.13 Example recordings with the curved probe. (A) Home cage recording of dorsal hippocampus local field potentials with the curved electrode across vigilance states. (A.1) The vigilance states during recording (wake, slow-wave sleep, and REM sleep). (A.2) Time-frequency decomposition of local field potential recorded at electrode 13 showing the frequency components characteristic of each vigilance state. (A.3) Raw recordings from electrodes 13, 14, and 15. (B) Close-up view of the recording shown in (A.3) for each of the vigilance states. (B.1) Recordings for electrodes 13, 14, and 15 were filtered between 1 and 300 Hz to show the local field potentials. (B.2) Unit recordings obtained from electrode 14. The signal from electrode 14 was filtered between 400 Hz and 12 kHz to show the single-unit activity recorded from electrode 14. The close-up view underneath each trace shows clearly defined single-unit activity.

The probe successfully penetrated and recorded dorsal hippocampus local field potentials across vigilance states using the curved electrode (Figure 5.13(A.1)). The time-frequency decomposition of the local field potential recorded at electrode 13 (Figure 5.13(A.2)) reveals the frequency components characteristic of each vigilance state. REM sleep shows high theta power (high power in the 6 to 12 Hz range), slow-wave sleep exhibits high power in the delta band (1 to 4 Hz), and wakefulness displays lower overall power with some periods of theta (peaks in the 6 to 12 Hz range). Raw recordings from electrodes 13, 14, and 15 are presented in Figure 5.13(A.3). A close-up view of these recordings is shown in Figure 5.13 for each of the three vigilance states. Recordings from electrodes 13, 14, and 15 were filtered between 1 and 300 Hz to show the local field potentials component (Figure 5.13(B.1)). Unit recordings obtained from electrode 14 are displayed in Figure 5.13(B.2). The signal recorded from electrode 14 was filtered between 400 Hz and 12 kHz to reveal single-unit activity at this site. The close-up view beneath each trace clearly shows defined single-unit activity (firing from a single neuron).

5.7 Conclusion

This chapter reveals an unprecedented attempt at the creation and implementation of an innovative curved neural probe yet to be attempted in neural interface technology. The development of a flexible yet implantable curved neural probe using a silk shuttle and a high-performance neural interface with optimized PEDOT coatings. Silk was selected for its recognized biocompatibility and rigidity, which offer mechanical strength during insertion and soften post-implantation. The desired curved probe shape was achieved through PDMS molding. This method produced a sharp and adequately stiff curved shuttle that successfully penetrated and implanted into the mouse hippocampus utilizing a rotating implantation approach.

Prior to in vivo experiments, the electrical properties of the microelectrode array were enhanced and characterized using electrodeposited PEDOT:BF_4 coatings. The process of depositing PEDOT onto microelectrodes poses unique challenges for optimizing electropolymerization, largely due to hemispherical diffusion effects. Furthermore, to enhance the energetic stability and surface quality of the electrodes before PEDOT deposition, the polycrystalline Au microelectrodes underwent restructuring and cleaning. The relationship between charge density and the electrical properties of PEDOT was examined with deposition charges varying from 0.05 Ccm-2 to 3.0 Ccm-2. Optical microscopy revealed that the PEDOT films varied from translucent thin layers closely adhering to

the electrode surface to much thicker films that extended well beyond it. It was observed that the impedance of the PEDOT films decreased with higher charge density, reaching the lowest impedance for the 0.3 Ccm^{-2} film. However, the thickness and excessive growth of the PEDOT film do not form an ideal interface with cells and showed poor adhesion. We found that PEDOT films at 0.3 Ccm^{-2} provided the best compromise between electrical performance and surface characteristics for neural recordings. These films exhibited notable electrochemical advantages when compared to unmodified gold electrodes. The final silk-shuttled curved PEDOT microelectrode array was successfully implanted in vivo, allowing for the recording of local field potentials and unit activity from the dorsal hippocampus. Future experiments will focus on verifying the precise placement and orientation of the curved probe. Once verified, we will proceed with our ultimate goal of recording neural signals in the ventral hippocampus. If successful, these experiments will demonstrate the ability to record with high precision and unorthodox orientations in previously inaccessible brain areas.

CHAPTER 6 DISCUSSION

The progress in neuroscience and the creation of efficient neuroprosthetics depend significantly on our capacity to interface with the brain at high resolutions and for prolonged periods. As mentioned in the introduction, two main obstacles hinder advancement: the challenge of obtaining high spatiotemporal resolution recordings from deep and complex brain structures, and the insufficient long-term reliability and biocompatibility of existing neural electrodes. This thesis sought to tackle these issues using a twofold approach: initially, by leveraging the beneficial electrochemical characteristics of the conducting polymer poly(3,4-ethylenedioxythiophene) (PEDOT) to enhance electrode performance and durability; and subsequently, by introducing novel neural probe designs aimed at reaching previously difficult neural targets while potentially reducing the adverse foreign body response (FBR).

The first primary objective of this thesis focused on improving the electrical performance and assessing the long-term stability and biocompatibility of neural electrodes coated with electrodeposited PEDOT, specifically using the tetrafluoroborate dopant (PEDOT:BF_4). Article I directly addressed this objective through a comprehensive in vivo study utilizing conventional stiff Platinum-Iridium (PtIr) microwires coated with electrodeposited PEDOT:BF_4. Article I demonstrated that while these coatings significantly reduce the impedance of conventional stiff PtIr electrodes in vivo, facilitating better electrical communication, they did not lessen the FBR. This key finding suggests that for stiff implants, the chronic tissue reaction is primarily driven by mechanical mismatch, which the coating alone cannot overcome.

Context was provided by Article II, which showcased PEDOT:PSS in a different application (stretchable wearable sensors), highlighting the versatility but also the application-specific nature of PEDOT formulations and fabrication methods. While not directly focused on implantable devices, Article II provided relevant context by exploring a different PEDOT formulation, PEDOT:PSS, deposited via screen printing onto flexible substrates for wearable applications. This work demonstrated the versatility of PEDOT chemistry and processing, achieving highly stretchable (up to 600% strain) and conformable conductive films suitable for skin-surface bio-signal monitoring (EDA, sweat ion concentration). Article II underscored PEDOT's adaptability for creating functional interfaces on flexible substrates. This contrasts with the electropolymerization approach used in Article I and Chapter 5, which is well-suited for coating

pre-defined microelectrodes but less applicable to large-area stretchable electronics, further illustrating the application-specific nature of PEDOT formulation and fabrication choices

The second specific objective aimed to develop novel neural interface architectures capable of mapping unexplored circuits within deep 3D brain structures and mitigating the FBR. The second objective motivated the development of a novel neural interface architecture, detailed in Chapter 5. This involved creating an ultra-thin, flexible, curved probe body from parylene, specifically designed to align with neuronal layers in deep structures like the ventral hippocampus (vHP), which are difficult to target with linear probes. The work presented in Chapter 5 significantly departs from conventional probe designs. A key achievement was the successful microfabrication of an ultra-thin, flexible probe based on parylene C, incorporating microelectrodes patterned into a predefined curvature designed to align perpendicularly with neuronal layers in structures like the hippocampus. The electrodes were coated with an optimized PEDOT:BF_4 layer to ensure low impedance. To overcome the challenge of implanting a flexible device, a unique dissolvable silk shuttle was integrated, providing rigidity during insertion via a custom rotating implantation device. Successful fabrication, implantation, and in vivo recording (LFP and unit activity in the dorsal hippocampus) validated the feasibility of this approach.

The research advanced systematically: Article I highlighted the shortcomings of PEDOT coatings on rigid probes, particularly concerning FBR, which inspired the creation of the flexible, shuttled system in Chapter 3 to tackle both electrical and mechanical issues. The methodology utilized a thorough array of techniques; however, there are limitations, such as the requirement for additional long-term stability assessments and more histological confirmation of accurate curved probe placement.

Ultimately, this work confirms PEDOT's ability to enhance electrode properties but notes that mitigating the FBR, particularly for chronic implants, requires addressing mechanical factors, favouring flexible designs. The successful development of the silk-shuttled curved, flexible probe signifies a significant advancement towards recording deep brain regions by integrating optimized PEDOT coatings with innovative structural and implantation strategies. The findings highlight that advancing neural interface technology necessitates a careful balance of electrical, mechanical, and biological factors tailored to specific applications.

CHAPTER 7 CONCLUSIONS AND OUTLOOK

This thesis demonstrated improved neural interfacing by addressing key issues related to electrode performance, stability, and access to deep brain structures. The main contributions of this research were: (1) the characterization of the stability and performance of PEDOT:BF_4 coatings. Through chronic in vivo testing, this work confirmed that electrodeposited PEDOT:BF_4 coatings substantially reduce the impedance of neural electrodes, which is vital for enhancing recording quality and stimulation safety. However, it also established that on rigid implants, this improvement in electrode properties does not reduce the foreign body response, highlighting the role of mechanical factors in chronic biocompatibility. (2) The development and implementation of a novel flexible, curved neural probe. An important achievement was the successful design, microfabrication, and proof-of-concept validation of an innovative curved neural probe interface. This system features an ultra-thin, flexible, curved probe made of parylene, microelectrodes coated with optimized PEDOT:BF_4 and a unique dissolvable silk shuttle for implantation. This integrated approach represents a significant step towards enabling high-resolution recordings in complex, deep brain regions. The feasibility of the curved microelectrode system was confirmed through successful implantation and neural recording of in vivo LFP and unit activity in the dorsal hippocampus.

Recommendations for Future Research

Building on the contributions of this thesis, several directions for future research are suggested to further advance neural interface technology:

1. Develop and Assess Flexible Probes to Minimize FBR: Aim for designs that enable the entire implanted device to be mechanically compliant, possibly using materials similar to those researched for wearables but tailored for implantation. A thorough histological evaluation that contrasts these fully flexible designs with stiffer alternatives is a crucial step to measure the advantages in reducing the foreign body response.

2. Validate Curved Probe Targeting and Function in the Ventral Hippocampus: Perform experiments using the developed curved probe to target the ventral hippocampus (vHP). This requires refining implantation techniques for accuracy, using histological methods for precise placement verification, and conducting chronic recordings during relevant

behavioral tasks to demonstrate the scientific advantages of accessing this region with appropriately oriented electrodes.

3. Explore Alternative Shuttle and Implantation Strategies: Investigate other materials or improved designs for the implantation shuttle to enhance insertion reliability and tissue response. Using automated or image-guided implantation systems may also improve targeting accuracy for curved trajectories.

4. Conduct Systematic Comparative Studies: Perform systematic *in vivo* comparisons of various conducting polymers (including different formulations of PEDOT), deposition methods, and designs for flexible probes to establish clear guidelines for selecting optimal materials and fabrication strategies for specific chronic neural interface applications.

The advancements outlined in this thesis hold significant promise for transforming fundamental research in neuroscience and the field of neurotechnology. High-fidelity, minimally invasive tools like the flexible curved probe enable new investigations into the neural circuits that drive cognition, emotion, and behavior. This could lead to important discoveries in areas such as memory, emotional regulation, and related neurological disorders. Additionally, enhancements in electrode performance and stability play a crucial role in creating safer, more effective, and longer-lasting clinical neuroprosthetics, such as deep brain stimulators and brain-computer interfaces, ultimately striving to enhance the quality of life for those with neurological conditions. This research lays the groundwork for the next generation of neural interfaces by combining material optimization with innovative design.

REFERENCES

[1] J. Ortigoza-Diaz *et al.*, "Techniques and considerations in the microfabrication of parylene c microelectromechanical systems," *Micromachines,* vol. 9, no. 9, p. 422, 2018.

[2] K. D. Wise, J. B. Angell, and A. Starr, "An integrated-circuit approach to extracellular microelectrodes," *IEEE Trans. Biomed. Eng.,* vol. BME-17, no. 3, pp. 238-247, 1970.

[3] S. Kovac *et al.*, "Invasive epilepsy surgery evaluation," *Seizure,* vol. 44, pp. 125-136, 2017.

[4] J. Gonzalez-Martinez *et al.*, "Stereotactic placement of depth electrodes in medically intractable epilepsy," *Journal of neurosurgery,* vol. 120, no. 3, pp. 639-644, 2014.

[5] A. L. Benabid *et al.*, "Combined (thalamotomy and stimulation) stereotactic surgery of the vim thalamic nucleus for bilateral parkinson disease," *Applied Neurophysiology,* vol. 50, no. 1-6, pp. 344-346, 1988.

[6] R. E. Gross *et al.*, "Electrophysiological mapping for the implantation of deep brain stimulators for parkinson's disease and tremor," *Movement disorders: official journal of the Movement Disorder Society,* vol. 21, no. S14, pp. S259-S283, 2006.

[7] J. A. Sweet *et al.*, "Depths and grids in brain tumors: Implantation strategies, techniques, and complications," *Epilepsia,* vol. 54, no. s9, pp. 66-71, 2013.

[8] M. S. Berger *et al.*, "Brain mapping techniques to maximize resection, safety, and seizure control in children with brain tumors," *Neurosurgery,* vol. 25, no. 5, pp. 786-792, 1989.

[9] Edward F. Chang, "Towards large-scale, human-based, mesoscopic neurotechnologies," *Neuron,* vol. 86, no. 1, pp. 68-78, 2015.

[10] J. M. Delgado, H. Hamlin, and W. P. Chapman, "Technique of intracranial electrode implacement for recording and stimulation and its possible therapeutic value in psychotic patients," *Confin Neurol,* vol. 12, no. 5-6, pp. 315-9, 1952.

[11] P. Chauvel, J. Gonzalez-Martinez, and J. Bulacio, "Presurgical intracranial investigations in epilepsy surgery," *Handb Clin Neurol,* vol. 161, pp. 45-71, 2019.

[12] G. Buzsáki, *Rhythms of the brain*: Oxford University Press, 2006.

[13] G. Buzsáki *et al.*, "Pattern and inhibition-dependent invasion of pyramidal cell dendrites by fast spikes in the hippocampus in vivo," *Proc Natl Acad Sci U S A,* vol. 93, no. 18, pp. 9921-5, 1996.

[14] K. L. Drake *et al.*, "Performance of planar multisite microprobes in recording extracellular single-unit intracortical activity," *IEEE Trans. Biomed. Eng.,* vol. 35, no. 9, pp. 719-732, 1988.

[15] K. Frank and M. G. Fuortes, "Potentials recorded from the spinal cord with microelectrodes," *J Physiol,* vol. 130, no. 3, pp. 625-54, 1955.

[16] G. Buzsáki, C. A. Anastassiou, and C. Koch, "The origin of extracellular fields and currents--eeg, ecog, lfp and spikes," *Nature reviews. Neuroscience,* vol. 13, no. 6, pp. 407-420, 2012.

[17] R. Elul, "The genesis of the eeg," *Int Rev Neurobiol,* vol. 15, pp. 227-72, 1971.

[18] Z. Nádasdy *et al.*, "Extracellular recording and analysis of neuronal activity: From single cells to ensembles," *Neuronal Ensembles: Strategies for Recording and Decoding,* pp. 17-55, 1998.

[19] C. Nicholson and J. A. Freeman, "Theory of current source-density analysis and determination of conductivity tensor for anuran cerebellum," *Journal of Neurophysiology,* vol. 38, no. 2, pp. 356-368, 1975.

[20] U. Mitzdorf, "Current source-density method and application in cat cerebral cortex: Investigation of evoked potentials and eeg phenomena," *Physiological Reviews,* vol. 65, no. 1, pp. 37-100, 1985.

[21] T. L. Richardson, R. W. Turner, and J. J. Miller, "Action-potential discharge in hippocampal ca1 pyramidal neurons: Current source-density analysis," *J Neurophysiol,* vol. 58, no. 5, pp. 981-96, 1987.

[22] G. Buzsáki, "Large-scale recording of neuronal ensembles," *Nature Neuroscience,* vol. 7, no. 5, pp. 446-451, 2004.

[23] D. N. Hill, S. B. Mehta, and D. Kleinfeld, "Quality metrics to accompany spike sorting of extracellular signals," *The Journal of Neuroscience,* vol. 31, no. 24, pp. 8699-8705, 2011.

[24] S. B. Brummer and M. J. Turner, "Electrochemical considerations for safe electrical stimulation of the nervous system with platinum electrodes," *IEEE Trans. Biomed. Eng.,* vol. BME-24, no. 1, pp. 59-63, 1977.

[25] S. B. Baumann *et al.*, "The electrical conductivity of human cerebrospinal fluid at body temperature," *IEEE Trans. Biomed. Eng.,* vol. 44, no. 3, pp. 220-223, 1997.

[26] S. B. Hladky and M. A. Barrand, "Mechanisms of fluid movement into, through and out of the brain: Evaluation of the evidence," *Fluids and Barriers of the CNS,* vol. 11, no. 1, p. 26, 2014.

[27] A. N. Galindo, D. A. Frey Rubio, and M. H. Hettiaratchi, "Biomaterial strategies for regulating the neuroinflammatory response," *Materials Advances,* 10.1039/D3MA00736G, vol. 5, no. 10, pp. 4025-4054, 2024.

[28] C. Boehler *et al.*, "Tutorial: Guidelines for standardized performance tests for electrodes intended for neural interfaces and bioelectronics," *Nature Protocols,* vol. 15, no. 11, pp. 3557-3578, 2020.

[29] A. J. Bard, L. R. Faulkner, and H. S. White, *Electrochemical methods: Fundamentals and applications*: John Wiley & Sons, 2022.

[30] E. M. Hudak *et al.*, "Electron transfer processes occurring on platinum neural stimulating electrodes: Calculated charge-storage capacities are inaccessible during applied stimulation," *J. Neural Eng.,* vol. 14, no. 4, p. 046012, 2017.

[31] R. V. Shannon, "A model of safe levels for electrical-stimulation," *IEEE Trans. Biomed. Eng.,* vol. 39, no. 4, pp. 424-426, 1992.

[32] S. F. Cogan, "Neural stimulation and recording electrodes," *Annu. Rev. Biomed. Eng.,* vol. 10, no. 1, pp. 275-309, 2008.

[33] M. F. Suesserman, F. A. Spelman, and J. T. Rubinstein, "In vitro measurement and characterization of current density profiles produced by nonrecessed, simple recessed, and radially varying recessed stimulating electrodes," *IEEE Trans. Biomed. Eng.,* vol. 38, no. 5, pp. 401-408, 1991.

[34] T. L. Rose and L. S. Robblee, "Electrical stimulation with pt electrodes. Viii. Electrochemically safe charge injection limits with 0.2 ms pulses (neuronal application)," *IEEE Trans. Biomed. Eng.,* vol. 37, no. 11, pp. 1118-1120, 1990.

[35] D. A. Henze *et al.*, "Intracellular features predicted by extracellular recordings in the hippocampus in vivo," *Journal of Neurophysiology,* vol. 84, no. 1, pp. 390-400, 2000.

[36] K. D. Harris *et al.*, "Improving data quality in neuronal population recordings," *Nature Neuroscience,* vol. 19, no. 9, pp. 1165-1174, 2016.

[37] S. F. Lempka *et al.*, "Theoretical analysis of intracortical microelectrode recordings," *J. Neural Eng.,* vol. 8, no. 4, p. 045006, 2011.

[38] J. B. Johnson, "Thermal agitation of electricity in conductors," *Physical Review,* vol. 32, no. 1, pp. 97-109, 1928.

[39] P. Barthó *et al.*, "Characterization of neocortical principal cells and interneurons by network interactions and extracellular features," *J Neurophysiol,* vol. 92, no. 1, pp. 600-8, 2004.

[40] Y. Yao *et al.*, "A microassembled low-profile three-dimensional microelectrode array for neural prosthesis applications," *Journal of Microelectromechanical Systems,* vol. 16, no. 4, pp. 977-988, 2007.

[41] M. E. Merriam *et al.*, "A 3-d 160-site microelectrode array for cochlear nucleus mapping," *IEEE Trans. Biomed. Eng.,* vol. 58, no. 2, pp. 397-403, 2011.

[42] H. A. Wark *et al.*, "A new high-density (25 electrodes/mm^2) penetrating microelectrode array for recording and stimulating sub-millimeter neuroanatomical structures," *J Neural Eng,* vol. 10, no. 4, p. 045003, 2013.

[43] A. Branner *et al.*, "Long-term stimulation and recording with a penetrating microelectrode array in cat sciatic nerve," *IEEE Trans. Biomed. Eng.,* vol. 51, no. 1, pp. 146-157, 2004.

[44] W. Zhang *et al.*, "Role of neuroinflammation in neurodegeneration development," *Signal Transduction and Targeted Therapy,* vol. 8, no. 1, p. 267, 2023.

[45] L. Müller, S. Di Benedetto, and V. Müller, "From homeostasis to neuroinflammation: Insights into cellular and molecular interactions and network dynamics," *Cells,* vol. 14, no. 1, p. 54, 2025.

[46] A. Sierra *et al.*, "Janus-faced microglia: Beneficial and detrimental consequences of microglial phagocytosis," *Frontiers in Cellular Neuroscience,* Review, vol. 7, 2013.

[47] J. C. Barrese *et al.*, "Failure mode analysis of silicon-based intracortical microelectrode arrays in non-human primates," *J. Neural Eng.,* vol. 10, no. 6, p. 066014, 2013.

[48] R. Biran, D. C. Martin, and P. A. Tresco, "Neuronal cell loss accompanies the brain tissue response to chronically implanted silicon microelectrode arrays," *Experimental Neurology,* vol. 195, no. 1, pp. 115-126, 2005.

[49] Y. Zhou *et al.*, "Dual roles of astrocytes in plasticity and reconstruction after traumatic brain injury," *Cell Communication and Signaling,* vol. 18, no. 1, p. 62, 2020.

[50] R. Biran, D. C. Martin, and P. A. Tresco, "The brain tissue response to implanted silicon microelectrode arrays is increased when the device is tethered to the skull," *Journal of Biomedical Materials Research Part A,* vol. 82A, no. 1, pp. 169-178, 2007.

[51] C. H. Thompson *et al.*, "Spatiotemporal patterns of gene expression around implanted silicon electrode arrays," *J. Neural Eng.,* vol. 18, no. 4, p. 045005, 2021.

[52] G. F. Hoeferlin *et al.*, "Bacteria invade the brain following intracortical microelectrode implantation, inducing gut-brain axis disruption and contributing to reduced microelectrode performance," *Nat. Commun.,* vol. 16, no. 1, p. 1829, 2025.

[53] T. Goto *et al.*, "An evaluation of the conductivity profile in the somatosensory barrel cortex of wistar rats," *Journal of Neurophysiology,* vol. 104, no. 6, pp. 3388-3412, 2010.

[54] A. Mercanzini *et al.*, "In vivo electrical impedance spectroscopy of tissue reaction to microelectrode arrays," *IEEE Trans. Biomed. Eng.,* vol. 56, no. 7, pp. 1909-1918, 2009.

[55] V. Sankar *et al.*, "Electrode impedance analysis of chronic tungsten microwire neural implants: Understanding abiotic vs. Biotic contributions," *Frontiers in Neuroengineering,* Original Research, vol. 7, 2014.

[56] A. Carnicer-Lombarte *et al.*, "Foreign body reaction to implanted biomaterials and its impact in nerve neuroprosthetics," *Frontiers in Bioengineering and Biotechnology,* Systematic Review, vol. 9, 2021.

[57] M. Jorfi *et al.*, "Progress towards biocompatible intracortical microelectrodes for neural interfacing applications," *J. Neural Eng.,* vol. 12, no. 1, pp. 011001-011001, 2015.

[58] V. S. Polikov, P. A. Tresco, and W. M. Reichert, "Response of brain tissue to chronically implanted neural electrodes," *Journal of Neuroscience Methods,* vol. 148, no. 1, pp. 1-18, 2005.

[59] S. M. Wellman *et al.*, "A materials roadmap to functional neural interface design," *Adv. Funct. Mater.,* vol. 28, no. 12, 2018.

[60] T. D. Kozai *et al.*, "Brain tissue responses to neural implants impact signal sensitivity and intervention strategies," *ACS chemical neuroscience,* vol. 6, no. 1, pp. 48-67, 2015.

[61] J. Parvizi and S. Kastner, "Promises and limitations of human intracranial electroencephalography," *Nature Neuroscience,* vol. 21, no. 4, pp. 474-483, 2018.

[62] J. Talairach and J. Bancaud, "Stereotaxic approach to epilepsy," *Methodology of anatomo-functional stereotaxic investigations. Progr Neurol Surg,* vol. 5, pp. 297-354, 1973.

[63] H. O. Lüders *et al.*, "The epileptogenic zone: General principles," *Epileptic Disorders,* vol. 8, no. S2, pp. S1-S9, 2006.

[64] K. Machetanz *et al.*, "Frame-based and robot-assisted insular stereo-electroencephalography via an anterior or posterior oblique approach," *Journal of Neurosurgery,* vol. 135, no. 5, pp. 1477-1486, 2021.

[65] P. Chauvel and A. McGonigal, "Emergence of semiology in epileptic seizures," *Epilepsy & Behavior,* vol. 38, pp. 94-103, 2014.

[66] S. Alomar *et al.*, "The stereo-electroencephalography methodology," *Neurosurgery Clinics of North America,* vol. 27, no. 1, pp. 83-95, 2016.

[67] M. Narizzano *et al.*, "Seeg assistant: A 3dslicer extension to support epilepsy surgery," *BMC Bioinformatics,* vol. 18, no. 1, p. 124, 2017.

[68] M. R. Mercier *et al.*, "Advances in human intracranial electroencephalography research, guidelines and good practices," *NeuroImage,* vol. 260, p. 119438, 2022.

[69] E. Halgren, K. Marinkovic, and P. Chauvel, "Generators of the late cognitive potentials in auditory and visual oddball tasks," *Electroencephalogr Clin Neurophysiol,* vol. 106, no. 2, pp. 156-64, 1998.

[70] E. Patrick *et al.*, "Corrosion of tungsten microelectrodes used in neural recording applications," *Journal of Neuroscience Methods,* vol. 198, no. 2, pp. 158-171, 2011.

[71] D. Yi *et al.*, "Design, fabrication, and implantation of invasive microelectrode arrays as in vivo brain machine interfaces: A comprehensive review," *Journal of Manufacturing Processes,* vol. 126, pp. 185-207, 2024.

[72] S. Woldring and M. N. Dirken, "Spontaneous unit-activity in the superficial cortical layers," *Acta Physiol Pharmacol Neerl,* vol. 1, no. 3, pp. 369-79, 1950.

[73] T. G. H. Yuen and W. F. Agnew, "Histological evaluation of polyesterimide-insulated gold wires in brain," *Biomaterials,* vol. 16, no. 12, pp. 951-956, 1995.

[74] L. Li *et al.*, "Electrochemical and biological performance of hierarchical platinum-iridium electrodes structured by a femtosecond laser," *Microsystems & Nanoengineering,* vol. 8, no. 1, p. 96, 2022.

[75] L. Li, C. Jiang, and L. Li, "Hierarchical platinum–iridium neural electrodes structured by femtosecond laser for superwicking interface and superior charge storage capacity," *Bio-Design and Manufacturing,* vol. 5, no. 1, pp. 163-173, 2022.

[76] A. T. Sidambe, "Biocompatibility of advanced manufactured titanium implants—a review," *Materials,* vol. 7, no. 12, pp. 8168-8188, 2014.

[77] J. D. Weiland, D. J. Anderson, and M. S. Humayun, "In vitro electrical properties for iridium oxide versus titanium nitride stimulating electrodes," *IEEE Trans Biomed Eng,* vol. 49, no. 12 Pt 2, pp. 1574-9, 2002.

[78] L. Xindong *et al.*, "Stability of the interface between neural tissue and chronically implanted intracortical microelectrodes," *IEEE Transactions on Rehabilitation Engineering,* vol. 7, no. 3, pp. 315-326, 1999.

[79] M. Salcman and M. J. Bak, "A new chronic recording intracortical microelectrode," *Medical and biological engineering,* vol. 14, no. 1, pp. 42-50, 1976.

[80] S. F. Cogan *et al.*, "In vitro comparison of the charge-injection limits of activated iridium oxide (airof) and platinum-iridium microelectrodes," *IEEE Trans. Biomed. Eng.,* vol. 52, no. 9, pp. 1612-1614, 2005.

[81] P. R. Troyk *et al.*, ""Safe" charge-injection waveforms for iridium oxide (airof) microelectrodes," communication presented at The 26th Annual International Conference of the IEEE Engineering in Medicine and Biology Society, 2004, pp. 4141-4144.

[82] A. Ghazavi *et al.*, "Electrochemical characteristics of ultramicro-dimensioned sirof electrodes for neural stimulation and recording," *J Neural Eng,* vol. 17, no. 1, p. 016022, 2020.

[83] M. A. L. Nicolelis *et al.*, "Chronic, multisite, multielectrode recordings in macaque monkeys," *Proceedings of the National Academy of Sciences,* vol. 100, no. 19, pp. 11041-11046, 2003.

[84] J. C. Williams, R. L. Rennaker, and D. R. Kipke, "Stability of chronic multichannel neural recordings: Implications for a long-term neural interface," *Neurocomputing,* vol. 26-27, pp. 1069-1076, 1999.

[85] A. Shah Idil and N. Donaldson, "The use of tungsten as a chronically implanted material," *J. Neural Eng.,* vol. 15, no. 2, p. 021006, 2018.

[86] S. F. Cogan *et al.*, "Over-pulsing degrades activated iridium oxide films used for intracortical neural stimulation," *J Neurosci Methods,* vol. 137, no. 2, pp. 141-50, 2004.

[87] L. S. Robblee *et al.*, "Electrical stimulation with pt electrodes. Vii. Dissolution of pt electrodes during electrical stimulation of the cat cerebral cortex," *J Neurosci Methods,* vol. 9, no. 4, pp. 301-8, 1983.

[88] J. McHardy *et al.*, "Electrical stimulation with pt electrodes. Iv. Factors influencing pt dissolution in inorganic saline," *Biomaterials,* vol. 1, no. 3, pp. 129-34, 1980.

[89] C. Boehler *et al.*, "Nanopt—a nanostructured electrode coating for neural recording and microstimulation," *ACS Appl. Mater. Interfaces,* vol. 12, no. 13, pp. 14855-14865, 2020.

[90] C. A. R. Chapman *et al.*, "Nanoporous gold biointerfaces: Modifying nanostructure to control neural cell coverage and enhance electrophysiological recording performance," *Adv. Funct. Mater.,* vol. 27, no. 3, p. 1604631, 2017.

[91] S. Venkatraman *et al.*, "In vitro and in vivo evaluation of pedot microelectrodes for neural stimulation and recording," *IEEE Trans. Neural Syst. Rehabilitation Eng.,* vol. 19, no. 3, pp. 307-316, 2011.

[92] K. A. Ludwig *et al.*, "Poly(3,4-ethylenedioxythiophene) (pedot) polymer coatings facilitate smaller neural recording electrodes," *J. Neural Eng.,* vol. 8, no. 1, 2011.

[93] K. A. Ludwig *et al.*, "Chronic neural recordings using silicon microelectrode arrays electrochemically deposited with a poly(3,4-ethylenedioxythiophene) (pedot) film," *J. Neural Eng.,* vol. 3, no. 1, p. 59, 2006.

[94] K. J. Seo *et al.*, "Transparent, flexible, penetrating microelectrode arrays with capabilities of single-unit electrophysiology," *Advanced Biosystems,* vol. 3, no. 3, 2019.

[95] B. Renshaw, A. Forbes, and B. R. Morison, "Activity of isocortex and hippocampus: Electrical studies with micro-electrodes," *Journal of Neurophysiology,* vol. 3, no. 1, pp. 74-105, 1940.

[96] H. Grundfest and B. Campbell, "Origin, conduction and termination of impulses in the dorsal spino-cerebellar tract of cats," *Journal of Neurophysiology,* vol. 5, no. 4, pp. 275-294, 1942.

[97] D. H. Hubel, "Tungsten microelectrode for recording from single units," *Science,* vol. 125, no. 3247, pp. 549-550, 1957.

[98] H. Grundfest *et al.*, "Stainless steel micro-needle electrodes made by electrolytic pointing," *Rev. Sci. Instrum.,* vol. 21, no. 4, pp. 360-361, 1950.

[99] E. M. Schmidt, M. J. Bak, and J. S. McIntosh, "Long-term chronic recording from cortical neurons," *Experimental Neurology,* vol. 52, no. 3, pp. 496-506, 1976.

[100] B. Y. Tay *et al.*, "Characterization of metallic micro rod arrays fabricated by μmim," *Mater. Charact.,* vol. 57, no. 2, pp. 80-85, 2006.

[101] C. Hassler *et al.*, "Characterization of parylene c as an encapsulation material for implanted neural prostheses," *Journal of Biomedical Materials Research Part B: Applied Biomaterials,* vol. 93B, no. 1, pp. 266-274, 2010.

[102] A. Prasad *et al.*, "Comprehensive characterization and failure modes of tungsten microwire arrays in chronic neural implants," *J. Neural Eng.,* vol. 9, no. 5, p. 056015, 2012.

[103] M. A. Wilson and B. L. McNaughton, "Dynamics of the hippocampal ensemble code for space," *Science,* vol. 261, no. 5124, pp. 1055-1058, 1993.

[104] C. M. Gray *et al.*, "Tetrodes markedly improve the reliability and yield of multiple single-unit isolation from multi-unit recordings in cat striate cortex," *Journal of Neuroscience Methods,* vol. 63, no. 1, pp. 43-54, 1995.

[105] M. S. Jog *et al.*, "Tetrode technology: Advances in implantable hardware, neuroimaging, and data analysis techniques," *Journal of Neuroscience Methods,* vol. 117, no. 2, pp. 141-152, 2002.

[106] A. Jules, "Fabrication of semiconductor devices," United States, 1964.

[107] Q. Bai and K. D. Wise, "Single-unit neural recording with active microelectrode arrays," *IEEE Trans Biomed Eng,* vol. 48, no. 8, pp. 911-20, 2001.

[108] J. Csicsvari *et al.*, "Massively parallel recording of unit and local field potentials with silicon-based electrodes," *J Neurophysiol,* vol. 90, no. 2, pp. 1314-23, 2003.

[109] J. Ji and K. D. Wise, "An implantable cmos circuit interface for multiplexed microelectrode recording arrays," *IEEE Journal of solid-state circuits,* vol. 27, no. 3, pp. 433-443, 2002.

[110] H.-Y. Chu and W. Fang, "A vertical convex corner compensation and non {111} crystal planes protection for wet anisotropic bulk micromachining process," *Journal of Micromechanics and Microengineering,* vol. 14, no. 6, p. 806, 2004.

[111] K. D. Wise and K. Najafi, "Microfabrication techniques for integrated sensors and microsystems," *Science,* vol. 254, no. 5036, pp. 1335-1342, 1991.

[112] F. Wu *et al.*, "An implantable neural probe with monolithically integrated dielectric waveguide and recording electrodes for optogenetics applications," *J. Neural Eng.,* vol. 10, no. 5, p. 056012, 2013.

[113] P. K. Campbell *et al.*, "A silicon-based, three-dimensional neural interface: Manufacturing processes for an intracortical electrode array," *IEEE Trans. Biomed. Eng.,* vol. 38, no. 8, pp. 758-768, 1991.

[114] L. R. Hochberg *et al.*, "Neuronal ensemble control of prosthetic devices by a human with tetraplegia," *Nature,* vol. 442, no. 7099, pp. 164-171, 2006.

[115] R. A. Normann *et al.*, "A neural interface for a cortical vision prosthesis," *Vision Research,* vol. 39, no. 15, pp. 2577-2587, 1999.

[116] K. E. Jones, P. K. Campbell, and R. A. Normann, "A glass/silicon composite intracortical electrode array," *Annals of Biomedical Engineering,* vol. 20, no. 4, pp. 423-437, 1992.

[117] H. Wark *et al.*, "A new high-density (25 electrodes/mm2) penetrating microelectrode array for recording and stimulating sub-millimeter neuroanatomical structures," *J. Neural Eng.,* vol. 10, no. 4, p. 045003, 2013.

[118] E. McGlynn *et al.*, "The future of neuroscience: Flexible and wireless implantable neural electronics," *Advanced Science,* vol. 8, no. 10, 2021.

[119] G. Hong and C. M. Lieber, "Novel electrode technologies for neural recordings," *Nature Reviews Neuroscience,* vol. 20, no. 6, pp. 330-345, 2019.

[120] J. Subbaroyan, D. C. Martin, and D. R. Kipke, "A finite-element model of the mechanical effects of implantable microelectrodes in the cerebral cortex," *J. Neural Eng.,* vol. 2, no. 4, p. 103, 2005.

[121] V. Castagnola *et al.*, "Parylene-based flexible neural probes with pedot coated surface for brain stimulation and recording," *Biosens. Bioelectron.,* vol. 67, pp. 450-457, 2015.

[122] X. C. Wang *et al.*, "A parylene neural probe array for multi-region deep brain recordings," *Journal of Microelectromechanical Systems,* vol. 29, no. 4, pp. 499-513, 2020.

[123] C. Xie *et al.*, "Three-dimensional macroporous nanoelectronic networks as minimally invasive brain probes," *Nat. Mater.,* Article, vol. 14, no. 12, pp. 1286-1292, 2015.

[124] T. Stieglitz *et al.*, "Micromachined, polyimide-based devices for flexible neural interfaces," *Biomed. Microdevices,* vol. 2, no. 4, pp. 283-294, 2000.

[125] A. Altuna *et al.*, "Su-8 based microprobes for simultaneous neural depth recording and drug delivery in the brain," *Lab on a Chip,* 10.1039/C3LC41364K, vol. 13, no. 7, pp. 1422-1430, 2013.

[126] K. Srikantharajah *et al.*, "Minimally-invasive insertion strategy and in vivo evaluation of multi-shank flexible intracortical probes," *Sci. Rep.,* vol. 11, no. 1, 2021.

[127] K. C. Cheung *et al.*, "Flexible polyimide microelectrode array for in vivo recordings and current source density analysis," *Biosens. Bioelectron.,* vol. 22, no. 8, pp. 1783-1790, 2007.

[128] S. P. Lacour, G. Courtine, and J. Guck, "Materials and technologies for soft implantable neuroprostheses," *Nature Reviews Materials,* vol. 1, no. 10, p. 16063, 2016.

[129] J. Liu *et al.*, "Syringe-injectable electronics," *Nature Nanotechnology,* vol. 10, no. 7, pp. 629-636, 2015.

[130] J. M. Lee *et al.*, "Stitching flexible electronics into the brain," *Advanced Science,* vol. 10, no. 16, p. 2300220, 2023.

[131] M. D. Ferro *et al.*, "Neuroroots, a bio-inspired, seamless brain machine interface for long-term recording in delicate brain regions," *AIP Advances,* vol. 14, no. 8, 2024.

[132] L. Zou *et al.*, "Self-assembled multifunctional neural probes for precise integration of optogenetics and electrophysiology," *Nat. Commun.,* vol. 12, no. 1, p. 5871, 2021.

[133] Z. Zhao *et al.*, "Ultraflexible electrode arrays for months-long high-density electrophysiological mapping of thousands of neurons in rodents," *Nature Biomedical Engineering,* vol. 7, no. 4, pp. 520-532, 2023.

[134] L. Luan *et al.*, "Ultraflexible nanoelectronic probes form reliable, glial scar–free neural integration," *Sci. Adv.,* vol. 3, no. 2, p. e1601966, 2017.

[135] S. Takeuchi *et al.*, "Parylene flexible neural probes integrated with microfluidic channels," *Lab on a Chip,* vol. 5, no. 5, pp. 519-523, 2005.

[136] L. W. Tien *et al.*, "Silk as a multifunctional biomaterial substrate for reduced glial scarring around brain-penetrating electrodes," *Adv. Funct. Mater.,* vol. 23, no. 25, pp. 3185-3193, 2013.

[137] F. Wu *et al.*, "Silk-backed structural optimization of high-density flexible intracortical neural probes," *Journal of Microelectromechanical Systems,* vol. 24, no. 1, pp. 62-69, 2015.

[138] A. Lecomte *et al.*, "Silk and peg as means to stiffen a parylene probe for insertion in the brain: Toward a double time-scale tool for local drug delivery," *Journal of Micromechanics and Microengineering,* vol. 25, no. 12, p. 125003, 2015.

[139] C. Cointe *et al.*, "Scalable batch fabrication of ultrathin flexible neural probes using a bioresorbable silk layer," *Microsystems & Nanoengineering,* vol. 8, no. 1, p. 21, 2022.

[140] Z. Ahmed *et al.*, "Flexible optoelectric neural interfaces," *Curr. Opin. Biotechnol.,* vol. 72, pp. 121-130, 2021.

[141] A. Williamson *et al.*, "Localized neuron stimulation with organic electrochemical transistors on delaminating depth probes," *Adv. Mater.,* vol. 27, no. 30, pp. 4405-4410, 2015.

[142] B. J. Kim *et al.*, "3d parylene sheath neural probe for chronic recordings," *J Neural Eng,* vol. 10, no. 4, p. 045002, 2013.

[143] J. Rivnay *et al.*, "High-performance transistors for bioelectronics through tuning of channel thickness," *Sci. Adv.,* vol. 1, p. 5, 2015.

[144] S. Reineke *et al.*, "White organic light-emitting diodes with fluorescent tube efficiency," *Nature,* vol. 459, no. 7244, pp. 234-238, 2009.

[145] M. Fahlman *et al.*, "Interfaces in organic electronics," *Nature Reviews Materials,* vol. 4, no. 10, pp. 627-650, 2019.

[146] I. Zozoulenko *et al.*, "Polarons, bipolarons, and absorption spectroscopy of pedot," *ACS Applied Polymer Materials,* vol. 1, no. 1, pp. 83-94, 2019.

[147] G. Malliaras and R. Friend, "An organic electronics primer," *Physics Today,* vol. 58, no. 5, pp. 53-58, 2005.

[148] T. P. Kaloni *et al.*, "Polythiophene: From fundamental perspectives to applications," *Chem. Mater.,* vol. 29, no. 24, pp. 10248-10283, 2017.

[149] M. Dietrich *et al.*, "Electrochemical and spectroscopic characterization of polyalkylenedioxythiophenes," *J. Electroanal. Chem.,* vol. 369, no. 1-2, pp. 87-92, 1994.

[150] E. Mitraka *et al.*, "Oxygen-induced doping on reduced pedot," *Journal of Materials Chemistry A,* 10.1039/C6TA10521A, vol. 5, no. 9, pp. 4404-4412, 2017.

[151] E. Genies, G. Bidan, and A. Diaz, "Spectroelectrochemical study of polypyrrole films," *Journal of Electroanalytical Chemistry and Interfacial Electrochemistry,* vol. 149, no. 1-2, pp. 101-113, 1983.

[152] A. F. Diaz *et al.*, "Electrochemistry of conducting polypyrrole films," *Journal of electroanalytical Chemistry and Interfacial electrochemistry,* vol. 129, no. 1-2, pp. 115-132, 1981.

[153] N. Rolland *et al.*, "Understanding morphology-mobility dependence in pedot: Tos," *Physical Review Materials,* vol. 2, no. 4, p. 045605, 2018.

[154] D. E. Raymond and D. J. Harrison, "Observation of pyrrole radical cations as transient intermediates during the anodic formation of conducting polypyrrole films," *J. Electroanal. Chem.,* vol. 361, no. 1-2, pp. 65-76, 1993.

[155] T. Otero and I. Boyano, "Comparative study of conducting polymers by the escr model," *The Journal of Physical Chemistry B,* vol. 107, no. 28, pp. 6730-6738, 2003.

[156] J. Heinze *et al.*, "On the origin of the so-called nucleation loop during electropolymerization of conducting polymers," *The Journal of Physical Chemistry B,* vol. 111, no. 5, pp. 989-997, 2007.

[157] J. Heinze, B. A. Frontana-Uribe, and S. Ludwigs, "Electrochemistry of conducting polymers—persistent models and new concepts," *Chem. Rev.,* vol. 110, no. 8, pp. 4724-4771, 2010.

[158] C. C. Bof Bufon *et al.*, "Relationship between chain length, disorder, and resistivity in polypyrrole films," *The Journal of Physical Chemistry B,* vol. 109, no. 41, pp. 19191-19199, 2005.

[159] E. Tamburri *et al.*, "Growth mechanisms, morphology, and electroactivity of pedot layers produced by electrochemical routes in aqueous medium," *Synth. Met.,* vol. 159, no. 5-6, pp. 406-414, 2009.

[160] D. C. Martin and G. G. Malliaras, "Interfacing electronic and ionic charge transport in bioelectronics," *ChemElectroChem,* vol. 3, no. 5, pp. 686-688, 2016.

[161] X. Y. Cui and D. C. Martin, "Electrochemical deposition and characterization of poly(3,4-ethylenedioxythiophene) on neural microelectrode arrays," *Sensors and Actuators B-Chemical,* vol. 89, no. 1-2, pp. 92-102, 2003.

[162] A. L. Kip *et al.*, "Chronic neural recordings using silicon microelectrode arrays electrochemically deposited with a poly(3,4-ethylenedioxythiophene) (pedot) film," *J. Neural Eng.,* vol. 3, no. 1, p. 59, 2006.

[163] A. L. Kip *et al.*, "Poly(3,4-ethylenedioxythiophene) (pedot) polymer coatings facilitate smaller neural recording electrodes," *J. Neural Eng.,* vol. 8, no. 1, p. 014001, 2011.

[164] T. Niederhoffer, A. Vanhoestenberghe, and H. T. Lancashire, "Methods of poly (3, 4)-ethylenedioxithiophene (pedot) electrodeposition on metal electrodes for neural stimulation and recording," *J. Neural Eng.,* vol. 20, no. 1, p. 011002, 2023.

[165] M. Bianchi *et al.*, "Poly(3,4-ethylenedioxythiophene)-based neural interfaces for recording and stimulation: Fundamental aspects and in vivo applications," *Advanced Science,* vol. 9, no. 12, 2022.

[166] Z. Aqrawe *et al.*, "Conducting polymers for neuronal microelectrode array recording and stimulation," *Sensors and Actuators B: Chemical,* vol. 257, pp. 753-765, 2018.

[167] M. Berggren *et al.*, "Ion electron–coupled functionality in materials and devices based on conjugated polymers," *Adv. Mater.,* vol. 31, no. 22, 2019.

[168] N. Rossetti *et al.*, "Poly(3,4-ethylenedioxythiophene) (pedot) coatings for high-quality electromyography recording," *ACS Applied Bio Materials,* vol. 2, no. 11, pp. 5154-5163, 2019.

[169] S. M. Won *et al.*, "Emerging modalities and implantable technologies for neuromodulation," *Cell,* vol. 181, no. 1, pp. 115-135, 2020.

[170] I. R. Minev *et al.*, "Electronic dura mater for long-term multimodal neural interfaces," *Science,* vol. 347, no. 6218, pp. 159-163, 2015.

[171] T. Wichmann and M. R. DeLong, "Deep brain stimulation for movement disorders of basal ganglia origin: Restoring function or functionality?," *Neurotherapeutics,* vol. 13, no. 2, pp. 264-283, 2016.

[172] K. Y. Chen *et al.*, "In vivo spatiotemporal patterns of oligodendrocyte and myelin damage at the neural electrode interface," *Biomaterials,* vol. 268, 2021.

[173] R. Green and M. R. Abidian, "Conducting polymers for neural prosthetic and neural interface applications," *Adv. Mater.,* vol. 27, no. 46, pp. 7620-37, 2015.

[174] S. Lee *et al.*, "Electrically conducting polymers for bio-interfacing electronics: From neural and cardiac interfaces to bone and artificial tissue biomaterials," *Biosens. Bioelectron.,* vol. 170, p. 112620, 2020.

[175] N. Rossetti *et al.*, "Neural and electromyography pedot electrodes for invasive stimulation and recording," *J. Mater. Chem. C,* 10.1039/D1TC00625H, vol. 9, no. 23, pp. 7243-7263, 2021.

[176] M. J. Donahue *et al.*, "Tailoring pedot properties for applications in bioelectronics," *Mater. Sci. Eng. R Rep.,* vol. 140, p. 100546, 2020.

[177] I. B. Dimov *et al.*, "Semiconducting polymers for neural applications," *Chem. Rev.,* vol. 122, no. 4, pp. 4356-4396, 2022.

[178] G. Schiavone *et al.*, "Guidelines to study and develop soft electrode systems for neural stimulation," *Neuron,* vol. 108, no. 2, pp. 238-258, 2020.

[179] C. Boehler *et al.*, "Long-term stable adhesion for conducting polymers in biomedical applications: Irox and nanostructured platinum solve the chronic challenge," *ACS Appl Mater Interfaces,* vol. 9, no. 1, pp. 189-197, 2017.

[180] L. Ouyang *et al.*, "Enhanced pedot adhesion on solid substrates with electrografted p(edot-nh2)," *Sci. Adv.,* vol. 3, no. 3, 2017.

[181] D. Chhin *et al.*, "Diazonium-based anchoring of pedot on pt/ir electrodes via diazonium chemistry," *J. Electrochem. Soc.,* vol. 165, no. 12, pp. G3066-G3070, 2018.

[182] J. Qu *et al.*, "Durability of poly(3,4-ethylenedioxythiophene) (pedot) films on metallic substrates for bioelectronics and the dominant role of relative shear strength," *Journal of the Mechanical Behavior of Biomedical Materials,* vol. 100, p. 103376, 2019.

[183] P. Oldroyd and G. G. Malliaras, "Achieving long-term stability of thin-film electrodes for neurostimulation," *Acta Biomater.,* vol. 139, pp. 65-81, 2022.

[184] X. S. Zheng *et al.*, "Electrode materials for chronic electrical microstimulation," *Advanced Healthcare Materials,* vol. 10, no. 12, 2021.

[185] C. Bodart *et al.*, "Electropolymerized poly(3,4-ethylenedioxythiophene) (pedot) coatings for implantable deep-brain-stimulating microelectrodes," *ACS Appl. Mater. Interfaces,* vol. 11, no. 19, pp. 17226-17233, 2019.

[186] T. D. Y. Kozai *et al.*, "Chronic in vivo evaluation of pedot/cnt for stable neural recordings," *IEEE Trans. Biomed. Eng.,* vol. 63, no. 1, pp. 111-119, 2016.

[187] A. N. Dalrymple *et al.*, "Electrochemical and mechanical performance of reduced graphene oxide, conductive hydrogel, and electrodeposited pt-ir coated electrodes: An active in vitro study," *J. Neural Eng.,* vol. 17, no. 1, p. 016015, 2019.

[188] M. Asplund *et al.*, "Toxicity evaluation of pedot/biomolecular composites intended for neural communication electrodes," *Biomed. Mater.,* Article, vol. 4, no. 4, p. 12, 2009.

[189] M. R. Abidian *et al.*, "Interfacing conducting polymer nanotubes with the central nervous system: Chronic neural recording using poly(3,4-ethylenedioxythiophene) nanotubes," *Adv. Mater.,* vol. 21, no. 37, pp. 3764-3770, 2009.

[190] P. R. Patel *et al.*, "Chronic in vivo stability assessment of carbon fiber microelectrode arrays," *J. Neural Eng.,* Article, vol. 13, no. 6, p. 15, 2016.

[191] T. D. Y. Kozai *et al.*, "Ultrasmall implantable composite microelectrodes with bioactive surfaces for chronic neural interfaces," *Nat. Mater.,* vol. 11, no. 12, p. 1065, 2012.

[192] H. Charkhkar *et al.*, "Chronic intracortical neural recordings using microelectrode arrays coated with pedot-tfb," *Acta Biomater.,* vol. 32, pp. 57-67, 2016.

[193] H. S. Mandal *et al.*, "Improving the performance of poly(3,4-ethylenedioxythiophene) for brain-machine interface applications," *Acta Biomater.,* vol. 10, no. 6, pp. 2446-2454, 2014.

[194] H. S. Mandal *et al.*, "Improved poly(3,4-ethylenedioxythiophene) (pedot) for neural stimulation," *Neuromodulation,* vol. 18, no. 8, pp. 657-663, 2015.

[195] X. L. Luo *et al.*, "Highly stable carbon nanotube doped poly(3,4-ethylenedioxythiophene) for chronic neural stimulation," *Biomaterials,* vol. 32, no. 24, pp. 5551-5557, 2011.

[196] C. L. Kolarcik *et al.*, "Evaluation of poly(3,4-ethylenedioxythiophene)/carbon nanotube neural electrode coatings for stimulation in the dorsal root ganglion," *J. Neural Eng.,* vol. 12, no. 1, 2015.

[197] X. S. Zheng *et al.*, "Evaluation of a conducting elastomeric composite material for intramuscular electrode application," *Acta Biomater.,* vol. 103, pp. 81-91, 2020.

[198] A. N. Dalrymple *et al.*, "Electrochemical and biological performance of chronically stimulated conductive hydrogel electrodes," *J. Neural Eng.,* vol. 17, no. 2, p. 026018, 2020.

[199] A. N. Dalrymple *et al.*, "Electrochemical and biological characterization of thin-film platinum-iridium alloy electrode coatings: A chronic in vivo study," *J. Neural Eng.,* vol. 17, no. 3, p. 036012, 2020.

[200] R. M. Miriani, M. R. Abidian, and D. R. Kipke, "Cytotoxic analysis of the conducting polymer pedot using myocytes," communication presented at 2008 30th Annual International Conference of the IEEE Engineering in Medicine and Biology Society, 2008, pp. 1841-1844.

[201] G. Buzsáki, C. A. Anastassiou, and C. Koch, "The origin of extracellular fields and currents — eeg, ecog, lfp and spikes," *Nature Reviews Neuroscience,* vol. 13, no. 6, pp. 407-420, 2012.

[202] M. E. J. Obien *et al.*, "Revealing neuronal function through microelectrode array recordings," *Frontiers in Neuroscience,* Review, vol. 8, no. 423, 2015.

[203] C. Boehler *et al.*, "Actively controlled release of dexamethasone from neural microelectrodes in a chronic in vivo study," *Biomaterials,* vol. 129, pp. 176-187, 2017.

[204] S. F. Lempka *et al.*, "In vivo impedance spectroscopy of deep brain stimulation electrodes," *J. Neural Eng.,* vol. 6, no. 4, p. 046001, 2009.

[205] N. A. Alba *et al.*, "In vivo electrochemical analysis of a pedot/mwcnt neural electrode coating," *Biosensors,* vol. 5, no. 4, pp. 618-646, 2015.

[206] A. M. Kuncel and W. M. Grill, "Selection of stimulus parameters for deep brain stimulation," *Clinical Neurophysiology,* Review, vol. 115, no. 11, pp. 2431-2441, 2004.

[207] S. F. Cogan *et al.*, "Tissue damage thresholds during therapeutic electrical stimulation," *J. Neural Eng.,* vol. 13, no. 2, pp. 021001-021001, 2016.

[208] R. H. Pudenz *et al.*, "Electrical stimulation of the brain. Ii. Effects on the blood-brain barrier," *Surg Neurol,* vol. 4, no. 2, pp. 265-270, 1975.

[209] T. D. Y. Kozai *et al.*, "Chronic tissue response to carboxymethyl cellulose based dissolvable insertion needle for ultra-small neural probes," *Biomaterials,* vol. 35, no. 34, pp. 9255-9268, 2014.

[210] Z. J. Du *et al.*, "Ultrasoft microwire neural electrodes improve chronic tissue integration," *Acta Biomater.,* vol. 53, pp. 46-58, 2017.

[211] A. Golabchi *et al.*, "Melatonin improves quality and longevity of chronic neural recording," *Biomaterials,* vol. 180, pp. 225-239, 2018.

[212] N. J. Michelson *et al.*, "Multi-scale, multi-modal analysis uncovers complex relationship at the brain tissue-implant neural interface: New emphasis on the biological interface," *J. Neural Eng.,* vol. 15, no. 3, p. 033001, 2018.

[213] P. Jastrzebska-Perfect *et al.*, "Mixed-conducting particulate composites for soft electronics," *Sci. Adv.,* vol. 6, no. 17, p. eaaz6767, 2020.

[214] T. Someya, Z. N. Bao, and G. G. Malliaras, "The rise of plastic bioelectronics," *Nature,* Review, vol. 540, no. 7633, pp. 379-385, 2016.

[215] W. Gao *et al.*, "Fully integrated wearable sensor arrays for multiplexed in situ perspiration analysis," *Nature,* vol. 529, no. 7587, pp. 509-514, 2016.

[216] D. Son *et al.*, "Multifunctional wearable devices for diagnosis and therapy of movement disorders," *Nature Nanotechnology,* vol. 9, no. 5, pp. 397-404, 2014.

[217] C. M. Proctor *et al.*, "An electrocorticography device with an integrated microfluidic ion pump for simultaneous neural recording and electrophoretic drug delivery in vivo," *Advanced Biosystems,* Article, vol. 3, no. 2, p. 6, 2019.

[218] C. M. Proctor *et al.*, "Electrophoretic drug delivery for seizure control," *Sci. Adv.,* vol. 4, no. 8, p. eaau1291, 2018.

[219] K. Tybrandt *et al.*, "High-density stretchable electrode grids for chronic neural recording," *Adv. Mater.,* vol. 30, no. 15, 2018.

[220] A. Domínguez-Bajo *et al.*, "Interfacing neurons with nanostructured electrodes modulates synaptic circuit features," *Advanced Biosystems,* vol. 4, no. 9, p. 2000117, 2020.

[221] W. Wang *et al.*, "Strain-insensitive intrinsically stretchable transistors and circuits," *Nature Electronics,* vol. 4, no. 2, pp. 143-150, 2021.

[222] B. Zhang *et al.*, "Stretchable conductive fibers based on a cracking control strategy for wearable electronics," *Adv. Funct. Mater.,* vol. 28, no. 29, p. 1801683, 2018.

[223] L. Cai *et al.*, "Fully printed stretchable thin-film transistors and integrated logic circuits," *ACS Nano,* vol. 10, no. 12, pp. 11459-11468, 2016.

[224] S. Choi *et al.*, "Recent advances in flexible and stretchable bio-electronic devices integrated with nanomaterials," *Adv. Mater.,* vol. 28, no. 22, pp. 4203-4218, 2016.

[225] X. Fan *et al.*, "Pedot:Pss for flexible and stretchable electronics: Modifications, strategies, and applications," *Advanced Science,* vol. 6, no. 19, p. 1900813, 2019.

[226] H. Lee *et al.*, "Ultrathin organic electrochemical transistor with nonvolatile and thin gel electrolyte for long-term electrophysiological monitoring," *Adv. Funct. Mater.,* vol. 29, no. 48, p. 1906982, 2019.

[227] Y. Liang *et al.*, "Pedot:Pss-based bioelectronic devices for recording and modulation of electrophysiological and biochemical cell signals," *Advanced Healthcare Materials,* vol. 10, no. 11, p. 2100061, 2021.

[228] Y. Y. Broza *et al.*, "Disease detection with molecular biomarkers: From chemistry of body fluids to nature-inspired chemical sensors," *Chem. Rev.,* vol. 119, no. 22, pp. 11761-11817, 2019.

[229] H. Kai *et al.*, "Intrinsically stretchable electrochromic display by a composite film of poly(3,4-ethylenedioxythiophene) and polyurethane," *ACS Appl. Mater. Interfaces,* vol. 9, no. 23, pp. 19513-19518, 2017.

[230] Y. Li *et al.*, "Highly stretchable polystyrene sulfonate organic electrochemical transistors achieved via polyethylene glycol addition," *Flexible and Printed Electronics,* vol. 4, no. 4, p. 044004, 2019.

[231] S. Zhang *et al.*, "Tuning the electromechanical properties of pedot:Pss films for stretchable transistors and pressure sensors," *Advanced Electronic Materials,* vol. 5, p. 1900191, 2019.

[232] L. V. Kayser and D. J. Lipomi, "Stretchable conductive polymers and composites based on pedot and pedot:Pss," *Adv. Mater.,* vol. 31, no. 10, p. 1806133, 2019.

[233] D. J. Lipomi *et al.*, "Electronic properties of transparent conductive films of pedot:Pss on stretchable substrates," *Chem. Mater.,* vol. 24, no. 2, pp. 373-382, 2012.

[234] J. Y. Oh *et al.*, "Conducting polymer dough for deformable electronics," *Adv. Mater.,* vol. 28, no. 22, pp. 4455-4461, 2016.

[235] R. B. Luo *et al.*, "A simple strategy for high stretchable, flexible and conductive polymer films based on pedot:Pss-pdms blends," *Org. Electron.,* vol. 76, 2020.

[236] S. Zhang *et al.*, "Patterning of stretchable organic electrochemical transistors," *Chem. Mater.,* vol. 29, no. 7, pp. 3126-3132, 2017.

[237] A. Chortos *et al.*, "Mechanically durable and highly stretchable transistors employing carbon nanotube semiconductor and electrodes," *Adv. Mater.,* vol. 28, no. 22, pp. 4441-4448, 2016.

[238] Y. Wang *et al.*, "A highly stretchable, transparent, and conductive polymer," *Sci. Adv.,* vol. 3, no. 3, p. e1602076, 2017.

[239] P. Andersson Ersman *et al.*, "Screen printed digital circuits based on vertical organic electrochemical transistors," *Flexible and Printed Electronics,* vol. 2, p. 12, 2017.

[240] M. Zabihipour *et al.*, "High yield manufacturing of fully screen-printed organic electrochemical transistors," *npj Flexible Electronics,* vol. 4, no. 1, p. 15, 2020.

[241] M. Sensi *et al.*, "Modulating the faradic operation of all-printed organic electrochemical transistors by facile in situ modification of the gate electrode," *ACS Omega,* vol. 4, no. 3, pp. 5374-5381, 2019.

[242] D.-H. Kim *et al.*, "Epidermal electronics," *Science,* vol. 333, no. 6044, p. 838, 2011.

[243] G. Buzsáki, "Theta oscillations in the hippocampus," *Neuron,* vol. 33, no. 3, pp. 325-340, 2002.

[244] S. Royer *et al.*, "Distinct representations and theta dynamics in dorsal and ventral hippocampus," *The Journal of Neuroscience,* vol. 30, no. 5, pp. 1777-1787, 2010.

[245] A. D. Ekstrom *et al.*, "Human hippocampal theta activity during virtual navigation," *Hippocampus,* vol. 15, no. 7, pp. 881-889, 2005.

[246] L. L. Colgin, "Mechanisms and functions of theta rhythms," *Annual review of neuroscience,* vol. 36, no. 1, pp. 295-312, 2013.

[247] M. S. Fanselow and H.-W. Dong, "Are the dorsal and ventral hippocampus functionally distinct structures?," *Neuron,* vol. 65, no. 1, pp. 7-19, 2010.

[248] B. A. Strange *et al.*, "Functional organization of the hippocampal longitudinal axis," *Nature reviews neuroscience,* vol. 15, no. 10, pp. 655-669, 2014.

[249] M. Vázquez *et al.*, "Influence of oxygen and carbon dioxide on the electrochemical stability of poly(3,4-ethylenedioxythiophene) used as ion-to-electron transducer in all-solid-state ion-selective electrodes," *Sensors and Actuators B: Chemical,* vol. 82, no. 1, pp. 7-13, 2002.

[250] H. Yamato, M. Ohwa, and W. Wernet, "Stability of polypyrrole and poly (3, 4-ethylenedioxythiophene) for biosensor application," *J. Electroanal. Chem.,* vol. 397, no. 1-2, pp. 163-170, 1995.

[251] X. Cui and D. C. Martin, "Electrochemical deposition and characterization of poly(3,4-ethylenedioxythiophene) on neural microelectrode arrays," *Sensors and Actuators B: Chemical,* vol. 89, no. 1, pp. 92-102, 2003.

[252] M. Heim, B. Yvert, and A. Kuhn, "Nanostructuration strategies to enhance microelectrode array (mea) performance for neuronal recording and stimulation," *Journal of Physiology-Paris,* vol. 106, no. 3-4, pp. 137-145, 2012.

[253] R. A. Green *et al.*, "Conducting polymers for neural interfaces: Challenges in developing an effective long-term implant," *Biomaterials,* vol. 29, no. 24-25, pp. 3393-3399, 2008.

[254] C. Boehler, Z. Aqrawe, and M. Asplund, "Applications of pedot in bioelectronic medicine," *Bioelectronics in Medicine,* vol. 2, no. 2, pp. 89-99, 2019.

[255] N. R. Armstrong *et al.*, "Interface modification of ito thin films: Organic photovoltaic cells," *Thin Solid Films,* vol. 445, no. 2, pp. 342-352, 2003.

[256] S. Baek, R. A. Green, and L. A. Poole-Warren, "The biological and electrical trade-offs related to the thickness of conducting polymers for neural applications," *Acta Biomater.,* vol. 10, no. 7, pp. 3048-3058, 2014.

[257] J. Yang and D. C. Martin, "Impedance spectroscopy and nanoindentation of conducting poly(3,4-ethylenedioxythiophene) coatings on microfabricated neural prosthetic devices," *J. Mater. Res.,* vol. 21, no. 5, pp. 1124-1132, 2006.

[258] V. Castagnola *et al.*, "Morphology and conductivity of pedot layers produced by different electrochemical routes," *Synth. Met.,* vol. 189, pp. 7-16, 2014.

[259] R. Kumar, "Advances in adhesion solutions for medical applications," SCS, Inc., Indianapolis, IN, in Proceedings of the SMTA Medical Electronics Symposium, 2008. [Online]. Available: https://scscoatings.com/technical-library/#

[260] I. S. Romero *et al.*, "Enhancing the interface in silk–polypyrrole composites through chemical modification of silk fibroin," *ACS Appl. Mater. Interfaces,* vol. 5, no. 3, pp. 553-564, 2013.

[261] A. R. Murphy, P. S. John, and D. L. Kaplan, "Modification of silk fibroin using diazonium coupling chemistry and the effects on hmsc proliferation and differentiation," *Biomaterials,* vol. 29, no. 19, pp. 2829-2838, 2008.

[262] J. Hagler *et al.*, "Performance of silk-polypyrrole bilayer actuators under biologically relevant conditions," *J. Appl. Polym. Sci.,* vol. 136, no. 2, p. 46922, 2019.

[263] G. Paxinos and K. B. Franklin, *Paxinos and franklin's the mouse brain in stereotaxic coordinates*: Academic press, 2019.

[264] J. H. Siegle *et al.*, "Open ephys: An open-source, plugin-based platform for multichannel electrophysiology," *J. Neural Eng.,* vol. 14, no. 4, p. 045003, 2017.

[265] M. C. Barnes *et al.*, "Deposition mechanism of gold by thermal evaporation: Approach by charged cluster model," *J. Cryst. Growth,* vol. 213, no. 1, pp. 83-92, 2000.

[266] W. Mahoney, S. Lin, and R. Andres, "Probing the nucleation of a thin metal film: Atom deposition vs. Cluster beam deposition," *MRS Online Proceedings Library,* vol. 355, pp. 83-88, 1994.

[267] B. E. Conway, "Electrochemical oxide film formation at noble metals as a surface-chemical process," *Prog. Surf. Sci.,* vol. 49, no. 4, pp. 331-452, 1995.

[268] A. Hamelin, "Cyclic voltammetry at gold single-crystal surfaces. Part 1. Behaviour at low-index faces," *J. Electroanal. Chem.,* vol. 407, no. 1-2, pp. 1-11, 1996.

[269] Q. Jiang, H. M. Lu, and M. Zhao, "Modelling of surface energies of elemental crystals," *J. Phys.: Condens. Matter,* vol. 16, no. 4, p. 521, 2004.

[270] Z. Wang *et al.*, "Tuning surface structure of 3d nanoporous gold by surfactant-free electrochemical potential cycling," *Adv. Mater.,* vol. 29, no. 41, p. 1703601, 2017.

[271] M. H. Fakhr *et al.*, "Cleaning of ltcc, pen, and pcb au electrodes towards reliable electrochemical measurements," *Sci. Rep.,* vol. 12, no. 1, p. 20431, 2022.

[272] J. Lukkari *et al.*, "Photocurrent spectroscopic study of the initiation and growth of poly (3-methylthiophene) films on electrode surfaces with different adsorption properties," *The Journal of Physical Chemistry,* vol. 98, no. 34, pp. 8525-8535, 1994.

[273] L. M. Fischer *et al.*, "Gold cleaning methods for electrochemical detection applications," *Microelectron. Eng.,* vol. 86, no. 4-6, pp. 1282-1285, 2009.

[274] A. R. Silva Olaya, B. Zandersons, and G. Wittstock, "Restructuring of nanoporous gold surfaces during electrochemical cycling in acidic and alkaline media," *ChemElectroChem,* vol. 7, no. 17, pp. 3670-3678, 2020.

[275] P. Ahrens *et al.*, "Electrochemical formation of gold nanoparticles on polycrystalline gold electrodes during prolonged potential cycling," *ChemElectroChem,* vol. 5, no. 6, pp. 943-957, 2018.

[276] C. Amatore *et al.*, "Cyclic voltammetry at microelectrodes. Influence of natural convection on diffusion layers as characterized by in situ mapping of concentration profiles," *Electrochem. Commun.,* vol. 11, no. 6, pp. 1269-1272, 2009.

[277] K. Kinoshita, J. Lundquist, and P. Stonehart, "Potential cycling effects on platinum electrocatalyst surfaces," *Journal of Electroanalytical Chemistry and Interfacial Electrochemistry,* vol. 48, no. 2, pp. 157-166, 1973.

[278] L. Pigani *et al.*, "Electropolymerisation of 3,4-ethylenedioxythiophene in aqueous solutions," *Electrochem. Commun.,* vol. 6, no. 11, pp. 1192-1198, 2004.

[279] H. Randriamahazaka, V. Noël, and C. Chevrot, "Nucleation and growth of poly(3,4-ethylenedioxythiophene) in acetonitrile on platinum under potentiostatic conditions," *J. Electroanal. Chem.,* vol. 472, no. 2, pp. 103-111, 1999.

[280] W. Obretenov *et al.*, "Underpotential deposition and electrocrystallization of metals an atomic view by scanning tunneling microscopy," *J. Electrochem. Soc.,* vol. 140, no. 3, p. 692, 1993.

[281] J. E. Hagler *et al.*, "Electrodeposited pedot:Bf4 coatings improve impedance of chronic neural stimulating probes in vivo," *Advanced Materials Interfaces,* vol. 9, no. 35, p. 2201066, 2022.

[282] E. B. Boz, M. Fritz, and A. Forner-Cuenca, "Electropolymerized poly(3,4-ethylenedioxythiophene) coatings on porous carbon electrodes for electrochemical separation of metals," *Advanced Materials Interfaces,* vol. 10, no. 9, p. 2202497, 2023.

[283] S. W. Feldberg, "Reinterpretation of polypyrrole electrochemistry. Consideration of capacitive currents in redox switching of conducting polymers," *Journal of the American Chemical Society,* vol. 106, no. 17, pp. 4671-4674, 1984.

[284] T. Yeu, T. V. Nguyen, and R. E. White, "A mathematical model for predicting cyclic voltammograms of electronically conductive polypyrrole," *J. Electrochem. Soc.,* vol. 135, no. 8, p. 1971, 1988.

[285] A. V. Volkov *et al.*, "Understanding the capacitance of pedot:Pss," *Adv. Funct. Mater.,* vol. 27, no. 28, 2017.

APPENDIX A Supporting information of Article I: Electrodeposited PEDOT:BF_4 Coatings Improve Impedance of Chronic Neural Stimulating Probes In Vivo

Jo'Elen Hagler, Jeeyeon Yeu, Xin Zhou, Guillaume Ducharme, Bénédicte Amilhon, and Fabio Cicoira**

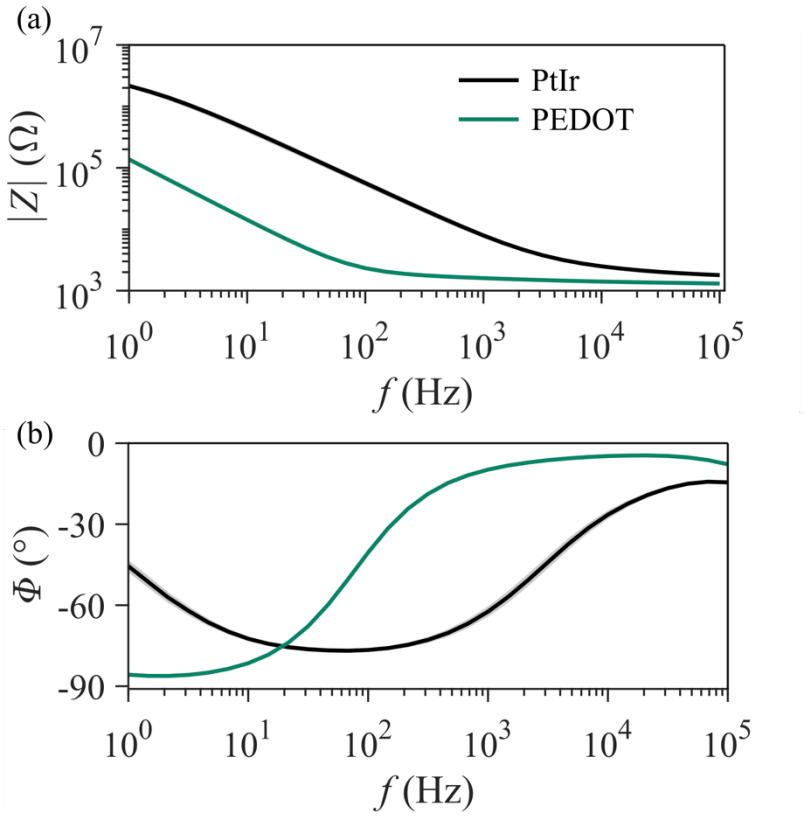

Figure A.1 Electrochemical measurements of PtIr (black) and PEDOT-coated PtIr (green) electrodes prior to implantation. (a) The average electrode impedance magnitude (Z) vs. frequency, and (b) the average phase of the impedance vs. frequency derived from EIS.

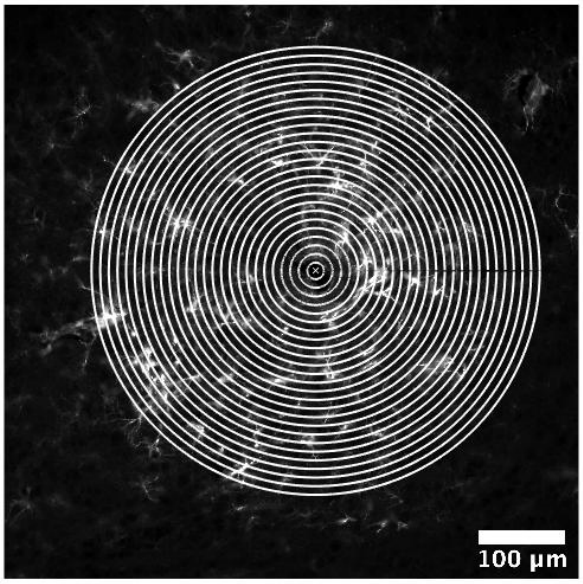

Figure A.2 The script generated masks of 25 concentric rings every 10 µm from the edge of the track, for a total distance of 250 µm from the implant surface.

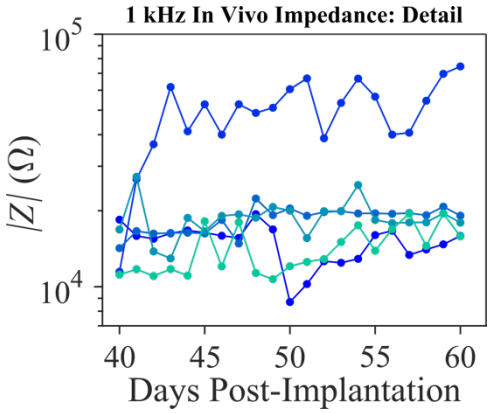

Figure A.3 Individual PEDOT electrode $|Z|$ from day 40 to day 60. Note that one outlier causes a sudden increase in the mean impedance of PEDOT electrodes.

APPENDIX B Supporting information of article II: Flexible and stretchable printed conducting polymer devices for electrodermal activity measurements

Jo'Elen Hagler, ChiHyeong Kim, Pierre Kateb, Jeeyeon Yu, Noemy Gagnon-Lafrenais, Erin Gee, Sofian Audry, Fabio Cicoira

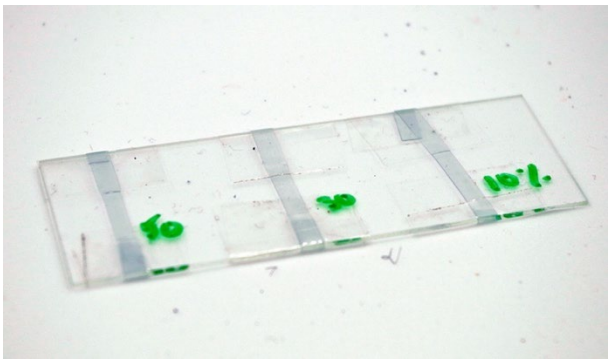

Figure B.1 PEDOT:PSS films on TPU substrate strained to 10%, 30%, or 50% and fixed to a

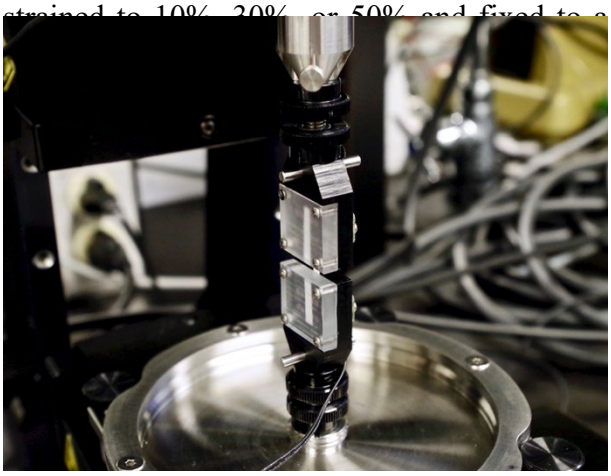

Figure B.2 Electrical tensile tester loaded with PEDOT:PSS sample.

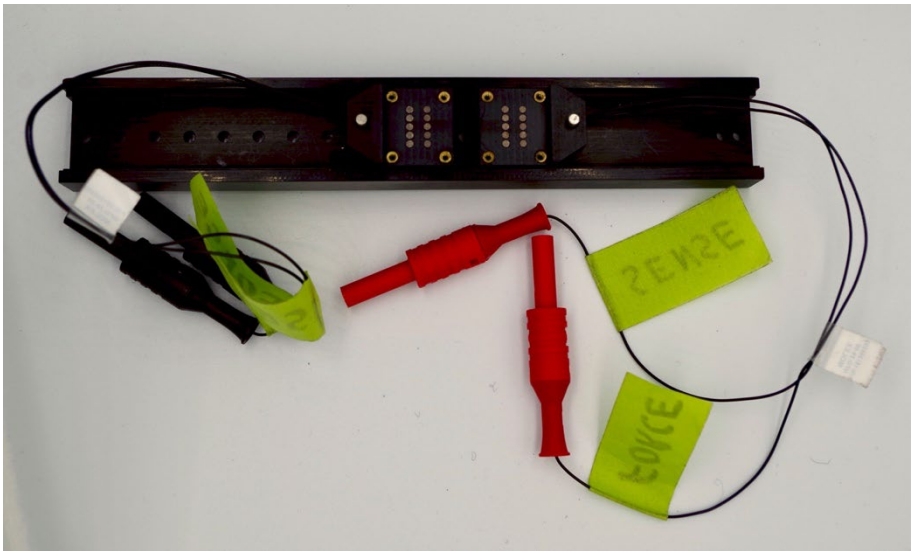

Figure B.3 Biomomentum electrical tensile tester used for strain tests. A 4 probe measurement set up is used to record the voltage under an applied current. Each probe has six circular electrodes connected in series.

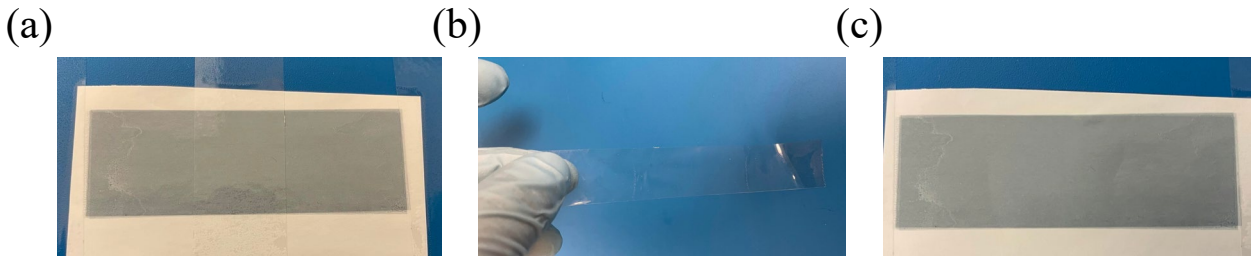

Figure B.4 Tape test of PEDOT:PSS adhesion to TPU. (a) PEDOT:PSS on TPU with tape in center of film. (b) Tape after removing from film. Tape shows no PEDOT:PSS was removed. (c) PEDOT:PSS film after tape was removed from center. No PEDOT:PSS was visibly removed.

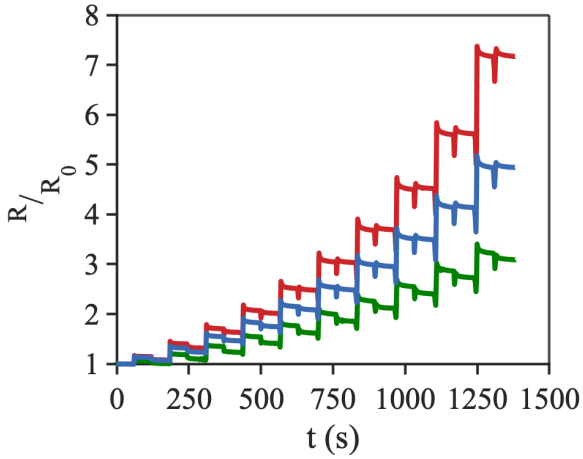

Figure B.5 Evolution of stretchable PEDOT:PSS film resistance with applied strain. Normalized resistance (R/R_0) (solid) vs time for films (n=3) under incremental stretching from 0% to (10 up to 100%) to 0% strain.

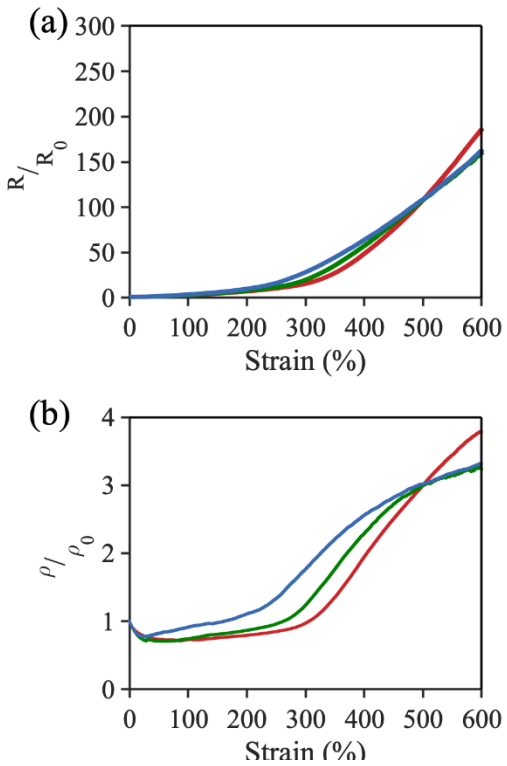

Figure B.6 Normalized (a) resistance and (b) resistivity of PEDOT:PSS films (n=3) when stretched from 0% to 600%.

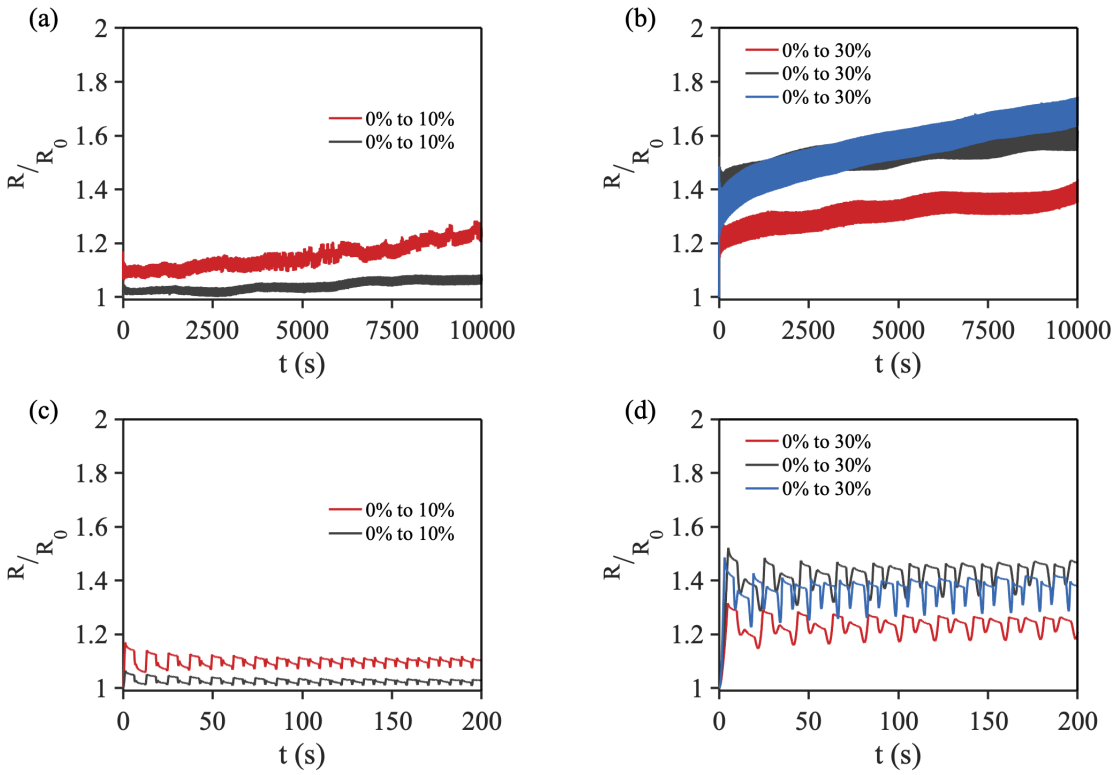

Figure B.7 Evolution of normalized resistance versus time while undergoing 1000 cycles of strain from 0% to (a) 10% (n=2) or (b) 30% strain (n=3). (c) First 200 s of (a). (d) First 200 s of (b).

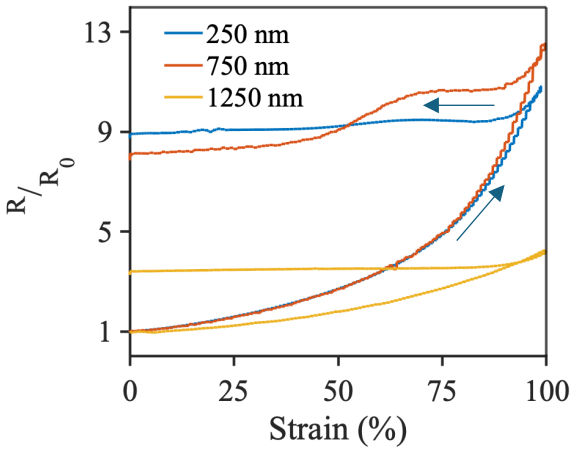

Figure B.8 Evolution of average normalized resistance of films with thicknesses of 250, 750 and 1250 nm, with strain from 0% to 100% to 0%.

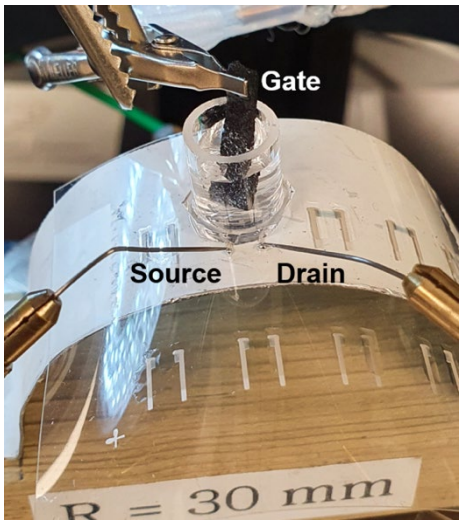

Figure B.9 Measurement of the bent PEDOT:PSS OECT characteristics.

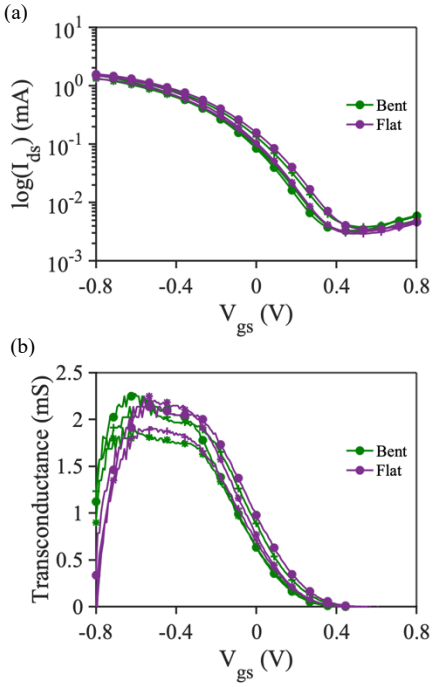

Figure B.10 Individual transfer curves for OECTs (n=3) measured while OECTs were bent (green) or flat (purple). (a) Drain current and (b) transconductance vs gate voltage measured at a drain voltage of -0.6 V.

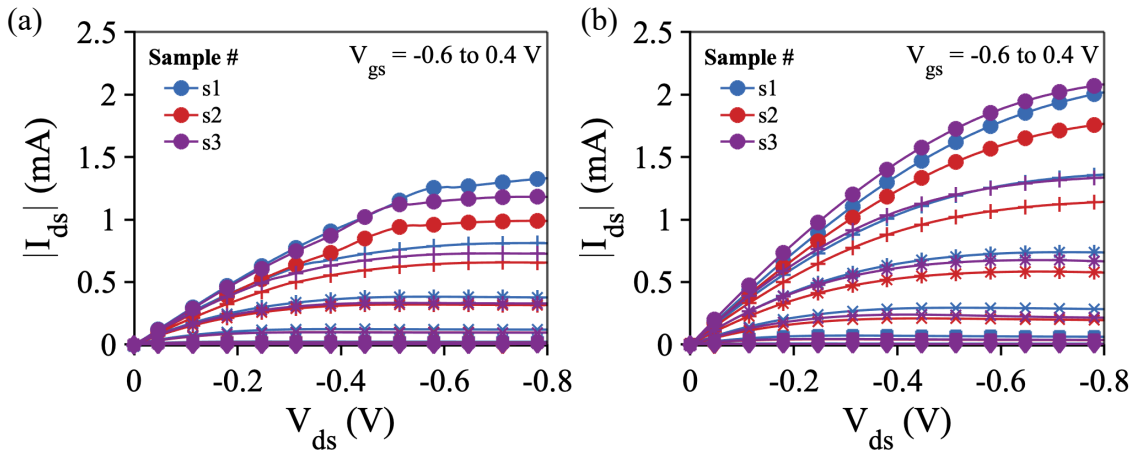

Figure B.11 Individual output curves for OECTs (n=3) measured while OECTs were (a) bent or (b) flat. Drain current vs drain voltage measured while applying a constant gate voltage ranging from -0.6 to 0.4 V.

Figure B.12 Steel electrodes and cable used to record EDA.

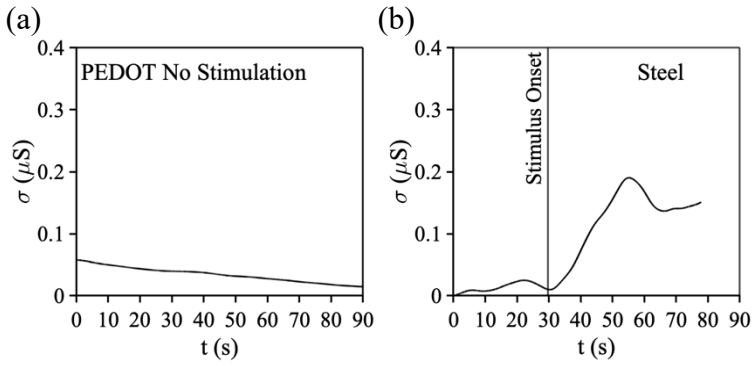

Figure B.13 EDA signal in conductance vs. time acquired with PEDOT:PSS electrodes from the fingertips of a volunteer who did not undergo audiovisual stimulation. (b) EDA signal collected with steel electrodes. Onset of audiovisual stimulation indicated by vertical line.